Inaugural dissertation

for

obtaining the doctoral degree

of the

Combined Faculty of Mathematics, Engineering and Natural Sciences

of the

Ruprecht-Karls-University

Heidelberg

Presented by

M.Sc. Veronika Buršić

born in: Pula, Croatia on 1st March 1997.

Oral examination: 8th December 2025.

Functional spatial genomics uncover a fusion-regulated and clinically relevant driver of metastasis in Ewing sarcoma

Referees:

Prof. Dr. Dr. Thomas Grünewald

&

Prof. Dr. Ursula Klingmüller

“Nothing in life is to be feared, it is only to be understood.

Now is the time to understand more, so that we may fear less.”

Marie Skłodowska-Curie

ABSTRACT

Metastasis is the major negative prognostic factor across cancer entities, yet how driver oncogenes shape transcriptional programs facilitating metastatic spread is poorly understood. In Ewing sarcoma (EwS), a highly aggressive pediatric soft-tissue and bone sarcoma, driven by chimeric FET::ETS transcription factors, low activity of the fusion oncoproteins are thought to promote metastasis, yet, the underlying mechanisms and key downstream effectors still remain largely elusive. Therefore, a spatial functional genomics approach in the EwS model identified for the first time that FET::ETS-low activity signature is localized at the invasive front of patient's tumor and is associated with the transcriptional induction of the multifunctional shuttle LIM domain only protein 7 (LMO7). Integrating these data with clinical information showed that high *LMO7* expression levels are associated with worse prognosis and the development of metastatic disease. Gene network analyses of transcriptomic data from patient-derived tumors as well as functional proteogenomic analyses of EwS cell lines with/without conditional RNA-interference-mediated knockdown of *LMO7*, highlight this gene as a regulatory hub involved in multiple pro-metastatic processes including epithelial-to-mesenchymal transition and cytoskeleton remodeling. Functional experiments prove that *LMO7* silencing decreases the capacity of EwS cells for clonogenic growth and migration *in vitro*, which is mirrored by reduced primary tumor growth and complete absence of metastatic burden *in vivo*.

In sum, these results identify LMO7 as clinically relevant key downstream regulator of FET::ETS fusions in EwS and provide an example of how the integration of functional, spatial and clinical data can shed light on how oncogenes promote metastasis in cancer.

Key words: Ewing sarcoma, metastasis, LMO7, EWSR1::ETS, spatial transcriptomics

ZUSAMMENFASSUNG

Metastasen haben einen wesentlichen negativen Einfluss auf die Diagnose verschiedener Krebsarten, doch wie Onkogene Transkriptionsprogramme beeinflussen, welche die Metastasierung begünstigen, ist noch weitgehend unverstanden. Beim Ewing-Sarkom (EwS), einem hochaggressiven pädiatrischen Weichteil- und Knochensarkom, das durch chimäre FET::ETS-Transkriptionsfaktoren angetrieben wird, wird angenommen, dass eine geringe Aktivität der Fusions-Onkoproteine die Metastasierung fördert. Die zugrunde liegenden Mechanismen und die wichtigsten nachgeschalteten Effektoren sind jedoch noch weitgehend unbekannt. In dieser Arbeit wurde mithilfe eines „spatial functional genomics“ Ansatzes im EwS-Modell erstmals festgestellt, dass die *FET::ETS*-low-Fusionsexpression an der invasiven Front des Tumors des Patienten lokalisiert ist und mit der transkriptionellen Induktion des multifunktionalen LIM domain 7 (LMO7) Shuttle-Proteins assoziiert ist. Die Integration dieser Daten mit klinischen Informationen zeigt, dass eine hohe Expression von *LMO7* sowie *EWSR1::ETS*-low-Signaturen mit einer schlechteren Prognose und der Entwicklung von Metastasen assoziiert sind. Gen-Netzwerkanalysen von Transkriptomdaten aus Tumoren von Patienten und funktionelle proteogenomische Analysen von EwS-Zelllinien mit/ohne konditionellem RNA-Interferenz induziertem *LMO7* Knockdown heben dieses Gen als regulatorischen Knotenpunkt hervor, der an mehreren metastasierungsfördernden Prozessen beteiligt ist, darunter die epitheliale-mesenchymale Transition und die Umgestaltung des Zytoskeletts. Funktionelle Experimente zeigen, dass *LMO7*-silencing die Fähigkeit von EwS-Zellen zum klonogenen Wachstum und zur Migration *in vitro* verringert, was sich in einem reduzierten Primärtumorwachstum und einem vollständigen Fehlen von Metastasen *in vivo* widerspiegelt.

Zusammenfassend lassen diese Ergebnisse darauf schließen, dass LMO7 ein klinisch relevanter Schlüsselregulator der FET::ETS-Fusionen bei EwS ist. Es wurde gezeigt, dass die Integration von funktionellen, spatial und klinischen Daten Aufschluss darüber geben kann, wie Onkogene die Metastasierung bei Krebs fördern.

Schlüsselwörter: Ewing-Sarkom, Matastasierung, LMO7, EWSR1::ETS, spatial transcriptomics

For little Gregory, now my guardian angel, and all other children who died of cancer.

TABLE OF CONTENTS

LIST OF FIGURES AND TABLES

LIST OF FIGURES

LIST OF TABLES

LIST OF ABBREVIATIONS

ACTB	actin beta
ALK	ALK receptor tyrosine kinase
AP-1	activator protein 1 transcription factor
APLP2	amyloid precursor-like protein 2
ATTC	American Type Culture Collection
AURKA	aurora kinase A
BCL11B	BCL11 transcription factor B
BMP1	bone morphogenetic protein 1
BRAF	B-Raf proto-oncogene, serine/threonine kinase
CASP3	caspase 3
CBP	CREB binding lysine acetyltransferase
CD99	CD99 antigen
CDKN2A	cyclin dependent kinase inhibitor 2A
CFA	Colony forming assay
CH	calponin homology domain
circLMO7	circular LMO7 RNA
CLK1	CDC like kinase 1
COG	Children's Oncology Group
CREB1	cyclic AMP-responsive element-binding protein 1
CT	computed tomography
CTCs	circulating tumor cells
CYR61	cysteine-rich angiogenic inducer 61
DBD	DNA binding domain
DDX5	DEAD-box helicase 5
DES	desmin
DNMT	DNA methyltransferase
Dox	doxycycline
DSMZ	German Collection of Microorganisms and Cell Cultures
ECM	extracellular matrix
EGFR	epidermal growth factor receptor
EMT	epithelial-to-mesenchymal transition
ERG	ETS transcription factor ERG
ERK	extracellular-signal-regulated kinase
ESCLA	Ewing Sarcoma Cell Line Atlas
ETS1	ETS proto-oncogene 1, transcription factor
ETV1	ETS variant transcription factor 1
ETV4	ETS variant transcription factor 4

EwS	Ewing sarcoma
EWSR1	EWS RNA binding protein 1
FAK	focal adhesion kinase
FBX	F-box domain
FCS	Fetal Calf Serum
FEV	FEV transcription factor, ETS family member
FFPE	formalin-fixed paraffin-embedded
FISH	fluorescence *in situ* hybridization
FLI1	Fli-1 proto-oncogene, ETS transcription factor
FOS	Fos proto-oncogene, AP-1 transcription factor subunit
FOXO1	forkhead box O1
FUS	FUS RNA binding protein
GLG1	golgi glycoprotein 1
GLI1	GLI family zinc finger 1
GSEA	gene set enrichment analysis
HIF-1α	hypoxia inducible factor 1 subunit alpha
H&E	Hematoxylin and Eosin
HLA	human leukocyte antigen
hnRNP K	heterogeneous nuclear ribonucleoprotein K
IF	immunofluorescence
IGF	insulin-like growth factor
IGF-1	insulin like growth factor 1
IGFBP3	insulin-like growth factor binding protein 3
IHC	immunohistochemistry
IL1RAP	IL1 receptor accessory protein
JAK-STAT	Janus kinase/signal transducers and activators of transcription
JNK	c-Jun N-terminal kinase
JUN	Jun proto-oncogene, AP-1 transcription factor subunit
KD	knockdown
KO	knockout
LMO7	LIM domain 7
LOX	lysyl oxidase
LOXHD1	lipoxygenase homology domain-containing protein 1
MAD2L2	mitotic arrest deficient 2 like 2
MAPK	mitogen-activated protein kinase
MAP3K12	mitogen-activated protein kinase kinase kinase 12
MET	mesenchymal-to-epithelial transition
MHC-I	major histocompatibility complex class I
MMP1	matrix metallopeptidase 1

MMP2	matrix metallopeptidase 2
MRI	magnetic resonance imaging
MRTFB	myocardin related transcription factor B
MSC	mesenchymal stem cells
MyoD	myoblast determination protein 1
MYPT1	myosin phosphatase target subunit 1
NCSCs	neural crest stem cells
NES	Normalized Enrichment Score
NFκB	nuclear factor-kappa B
NFATC2	nuclear factor of activated T cells 2
NGS	next-generation sequencing
NID2	nidogen 2
NKX2-2	NK2 homeobox 2
NMII	non-muscle myosin II
NSG	Nod/Scid/gamma
OE	overexpression
P300	EP300 lysine acetyltransferase
PAPP-A	pregnancy-associated plasma protein A
PATZ1	POZ/BTB and AT hook containing zinc finger 1
PAX3	paired box 3
PAX7	paired box 7
PDX	patient derived xenografts
PI3K	phosphoinositide 3-kinase
PI15	peptidase inhibitor 15
PPFIBP1	PPFIB scaffold protein 1
PRPF6	pre-mRNA processing factor 6
RBM11	RNA binding motif protein 11
RhoA	Ras homolog family member A
ROCK1	Rho associated coiled-coil containing protein kinase 1
RT	room temperature
RT-PCR	reverse transcription–polymerase chain reaction
Shh	Sonic Hedgehog
SMARCA5	SNF2 related chromatin remodeling ATPase 5
SP3	Sp3 transcription factor
STAG2	STAG2 cohesin complex component
SYT11	synaptotagmin 11
TAZ	Transcriptional coactivator with PDZ-binding motif
TCR	translational cancer research
TEAD	TEA domain transcription factor 1

TERT	telomerase reverse transcriptase
TGFBR2	transforming growth factor beta receptor 2
TGF-β	transforming growth factor beta
TME	tumor microenvironment
TNFα	tumor necrosis factor alpha
TNS3	tensin 3
TP53	tumor protein p53
TRAIL	TNF-related apoptosis-inducing ligand
TSPAN8	tetraspanin 8
TSS	transcription start site
TTN	titin
VEGFA	vascular endothelial growth factor A
WDR5	WD repeat domain 5
WGCNA	weighted gene correlation network analysis
YAP	Yes1 associated transcriptional regulator
ZEB2	zinc finger E-box binding homeobox 2

1. INTRODUCTION

1.1. About Ewing sarcoma

Ewing sarcoma (EwS) is a highly aggressive bone and soft tissue fusion-driven tumor, occurring predominantly in children, adolescents and young adults (Grünewald et al., 2018). It is the second most common primary bone tumor in children, and accounts for approximately 2% of all childhood cancer diagnoses (Chavan et al., 2023; Goodspeed et al., 2025). EwS was discovered in 1921 by Dr. James Ewing, after whom it was named (Ewing, 1921). Historically, it was known for high mortality rates, but through systematic clinical research, the outcomes for patients with localized disease and standard-risk have strongly improved to 70–80% overall survival (Durer et al., 2024; Grunewald et al., 2018.). Still, of particular concern are the survival rates of metastatic patients that have, unfortunately, remained relatively unchanged in the last decades, where overall survival is poor, being in the range of 20–30% (Zetouni & Sergi, 2022). EwS, metastatic and relapsed, typically have a poor prognosis and frequent recurrences, leading to high morbidity and mortality rates (Chavan et al., 2023). Therefore, further investigations of metastatic EwS are essential for better understanding and treatment of the disease.

1.2. Epidemiology, clinical representation and diagnostics of EwS

1.2.1. Epidemiology of EwS

EwS occurs with an incidence of approximately 2 cases/million people per year in the general population (Chakraborty et al., 2018). However, the incidence of EwS varies substantially by geographic region and ancestry. The peak incidence occurs in children and adolescents (10–19-year age group) across all regions, while the highest incidence rates are recorded in subpopulations with predominantly European ancestry (Spector et al., 2022). Here, incidence rates can typically range from less than 2 to about 5 cases per million (Siegel et al., 2025; Spector et al., 2022). Genome-Wide Association Studies have uncovered several single nucleotide polimorphisms that were significantly associated with the EwS suceptibility in populations of European ancestry, and were much rarer in populations of African or Asian ancestry (Machiela et al., 2018). Also, there is a consistent excess incidence in males compared to females across most regions (Dupuy et al., 2023; Spector et al., 2022).

1.2.2. Clinical features and treatment regimens in EwS

EwS mainly arises in bones and soft tissues. In bones, it predominantly occurs in the pelvis, femur, tibia, and ribs (Paulussen et al., 2001). Skeletal EwS most frequently involves the diaphysis or metadiaphyseal region of long bones of both lower and upper extremities (Choi et al., 2014). Commonly at the time of diagnosis, EwS tumors demonstrate extension into adjacent soft tissues (Kashima et al., 2013). In soft tissues, EwS predominantly occurs in the thoracic wall, gluteal muscle, pleural cavities and cervical muscles (Grünewald et al., 2018). Outcome of patients also significantly differs between patients with skeletal and extraskeletal EwS, where the latter has better overall survival (Applebaum et al., 2011).

Clinically, patients often present with localized pain and swelling. Patients may also present with a palpable mass, pathologic fracture, or constitutional symptoms such as fever, fatigue, weight loss, or anemia (Choi et al., 2014).

Radiographically, EwS typically manifests as a destructive, permeative osteolytic lesion that often extends trough the cortical bone to involve the periosteum and adjacent soft tissues. The intermittent growth of the tumor gives rise to the characteristic 'onion-skin' multilayered periosteal reaction. In some cases, erosion of the outer cortex by periosteal proliferation produces a concave cortical defect, referred to as 'saucerization'. Additional periosteal reactions, such as the vertical 'hair-on-end' appearance and the presence of Codman triangles, may also be seen in EwS (**Figure 1.1**) (Choi et al., 2014). EwS is a systemic disease with radiologically undetectable micrometastases already present at diagnosis (Bull et al., 2025), while the single-most powerful predictor of outcome in EwS is the presence of metastatic burden at time of diagnosis (Dasgupta et al., 2023). Patients with metastatic EwS have an abysmal 5-year survival rate of 20–35%, despite aggressive cytotoxic treatment regimens (Bosma et al., 2018). Considering that, imaging studies are the central tool for detection of metastases (Grünewald et al., 2018). Imaging modalities such as magnetic resonance imaging (MRI) and computed tomography (CT) are part of conventional staging methods in EwS (Furth et al., 2005) and can help determine the extent of bone and soft tissue tumor involvement and assess for metastatic disease (Choi et al, 2014). CT of the chest has replaced chest radiograph as the standard-of-care to assess for pulmonary involvement (**Figure 1.1c**) (Dasgupta et al., 2023). The early diagnosis of EwS remains challenging. Despite similar symptoms, pseudotumoral and benign bone lesions occur more frequently (Zöllner et al., 2021). The clinical stage at diagnosis is one of the major predictors of survival. Therfore,

accurate determination of tumor burden at diagnosis is a critical factor in planning treatment and predicting the patient outcome (Grunewald et al., 2018).

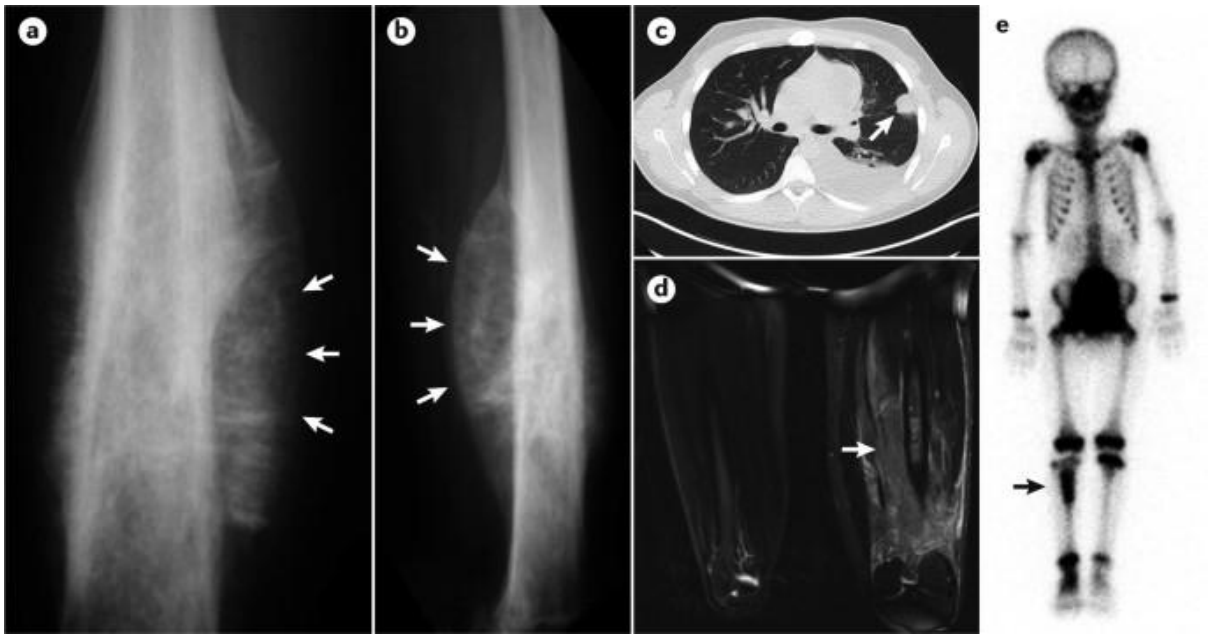

Figure 1.1 Radiological presentation of EwS. a. Anteroposterior and **b**. lateral X-ray images of a 14-year-old patient demonstrate EwS osteolytic lesion in the right femur with associated periosteal soft-tissue involvement (arrows). **c.** Lungs CT scan of a 19-year-old male patient reveals a pulmonary metastasis (arrow). **d.** MRI of the same patient shown in panels **a** and **b** illustrates the primary femoral tumor with adjacent soft-tissue edema (arrow). **e.** Bone scintigraphy of a 6-year-old patient indicates a tumor mass in the right tibia (arrow). Figure reprinted from: Grunewald et al. (2018), PMID: 29977059, through copyright license number: 6043070238889.

The diagnosis and treatment of EwS in children and adolescents should be carried out in accordance with pediatric oncology guidelines at an interdisciplinary and experienced pediatric oncology center to achieve optimal therapeutic outcomes (Biermann et al., 2025; Gaspar et al., 2015; Zarghooni et al., 2023). Current standard-of-care options comprise induction chemotherapy, tumor resection, and postoperative consolidation (Zarghooni et al., 2023). Most commonly used chemotherapy regimen is VDC/IE, which alternates between two combinations of drugs, given between 2 or 3 weeks. The first drug combination includes vincristine, doxorubicin and cyclophosphamide and the second set of drugs includes a combination of ifosfamide and etoposide (Zarghooni et al., 2023). Furthermore, consolidation radiotherapy of the primary tumor and selected metastases plays a significant role in the treatment of EwS. In patients with lung metastases detectable at diagnosis, whole-lung radiotherapy is also necessary. Radiotherapy in young patients should preferably be provided

in the form of proton therapy, which lowers the burden on surrounding tissue (Zarghooni et al., 2023; Zollner et al., 2021).

1.2.3. Cytology and molecular diagnostics of EwS

The specific cell type(s) from which EwS originates are still under debate. When first reported by James Ewing in 1921, he proposed an endothelial origin on the basis of its cellular morphology and the rareness of the stroma (Ewing, 1921). He found that the tumor cells resembled activated endothelial cells, and thus termed it 'endothelioma of bone' (Cripe, 2011). He described tumor cells as uniform, small, and round, with clear cytoplasm, features that would later be classically summarized as a 'small round blue cell tumor' in histology (Wu & Govender, 2012). In 1971, a myelogenous origin of EwS was proposed given ultrastructural features resembling developing myelocytes (Kadin & Bensch, 1971). Since then, several hypotheses regarding the histogenesis of EwS have been developed, with neural crest stem cells (NCSCs) and mesenchymal stem cells (MSCs) receiving the most attention as the putative cells of origin (Tu et al., 2017). Those hypotheses are being supported with evidence that silencing of *EWSR1::FLI1* recovered the phenotype of their MSC progenitor (Tirode et al., 2007). Additionally, introduction of the EWSR1::FLI1 into human MSCs resulted in its stable expression as well as phenotypic and transcriptional changes that reflect key features of EwS (Riggi et al., 2008). Conversely, there is evidence supporting that EwS originates from NCSCs since they were also able to tolerate expression of EWSR1::FLI1 (von Levetzow et al., 2011) and recently same was showin for NCSCs in EwS zebrafish model (Vasileva et al., 2024).

EwS can develop in almost any part of the body, making the diagnosis process more complex. Classification of small round cell tumors of bone is oftentimes challenging due to overlapping clinicopathologic features (Choi et al., 2014). EwS is a highly malignant tumor composed of small round cells (Ozaki et al., 2015). CD99 antigen and FLI1 proto-oncogene (FLI1) or ETS transcription factor ERG (ERG) are important immunohistochemical (IHC) markers used to support diagnosis of EwS (**Figure 1.2, a–c**). However, all three are highly sensitive but nonspecific. Using a combination of several antibodies can significantly narrow the differential diagnosis and can help to make the final diagnosis. For example, specificity >95% is reached in combined use of CD99 and NK2 homeobox 2 (NKX2-2) and adding paired box 7 (PAX7) to the IHC panel may be even more useful (Gajdzis et al., 2022). Furthermore, adding BCL11 transcription factor B (BCL11B) and/or golgi glycoprotein 1 (GLG1) to the

IHC panel is sufficient to reach even higher specificity for EwS which may significantly reduce the number of misdiagnosed patients, and thus improve patient care (Baldauf et al., 2017).

A molecularly and diagnostically relevant hallmark of EwS is the oncogenic fusion between *FET* and *ETS* families of genes. Most common genetic fusion in EwS, found in ~90% of cases, is the one between EWS RNA binding protein 1 (*EWSR1*) and *FLI1*, namely t(11;22)(q24;q12) (Delattre, et al., 1992). Many other translocation partners are also possible within the family of *FET* genes and *ETS* transcription factors, second most common involving *ERG* gene (Sorensen et al., 1994) substituting *FLI1*, in 5–10% cases (Ginsberg et al., 1999). The role of EwS fusion proteins in tumorigenesis is complex and multifaceted. The subsequent chapter (1.3. Molecular signature and genetics of EwS) will examine the types as well as roles of the fusion proteins in EwS in greater detail.

Detection of the tumor-specific *FET::ETS* fusion gene is essential to diagnose EwS. Reverse transcription-polymerase chain reaction (RT-PCR) and fluorescence *in situ* hybridization (FISH) (**Figure 1.2d**) are commonly used to detect the fusion gene (Ueno-Yokohata et al., 2021). However, at least 28 fusion transcript variants have been reported, making rapid and accurate detection difficult. For that reason usage of multiplex RT-PCR to detect fusion genes for the diagnosis of EwS might also be suitable (Ueno-Yokohata et al., 2021). In recent years, usage of next-generation sequencing (NGS) significantly enhanced diagnostic accuracy, especially in IHC ambiguous pediatric sarcomas (He et al., 2025). NGS can analyze multiple genes simultaneously, providing a more complete genomic profile compared to traditional methods, but its usage is not widespread in clinical settings due to having longer turnaround time, being more expensive, and data analysis can being more complex, compared to traditional methods (Jeyaraman et al., 2025).

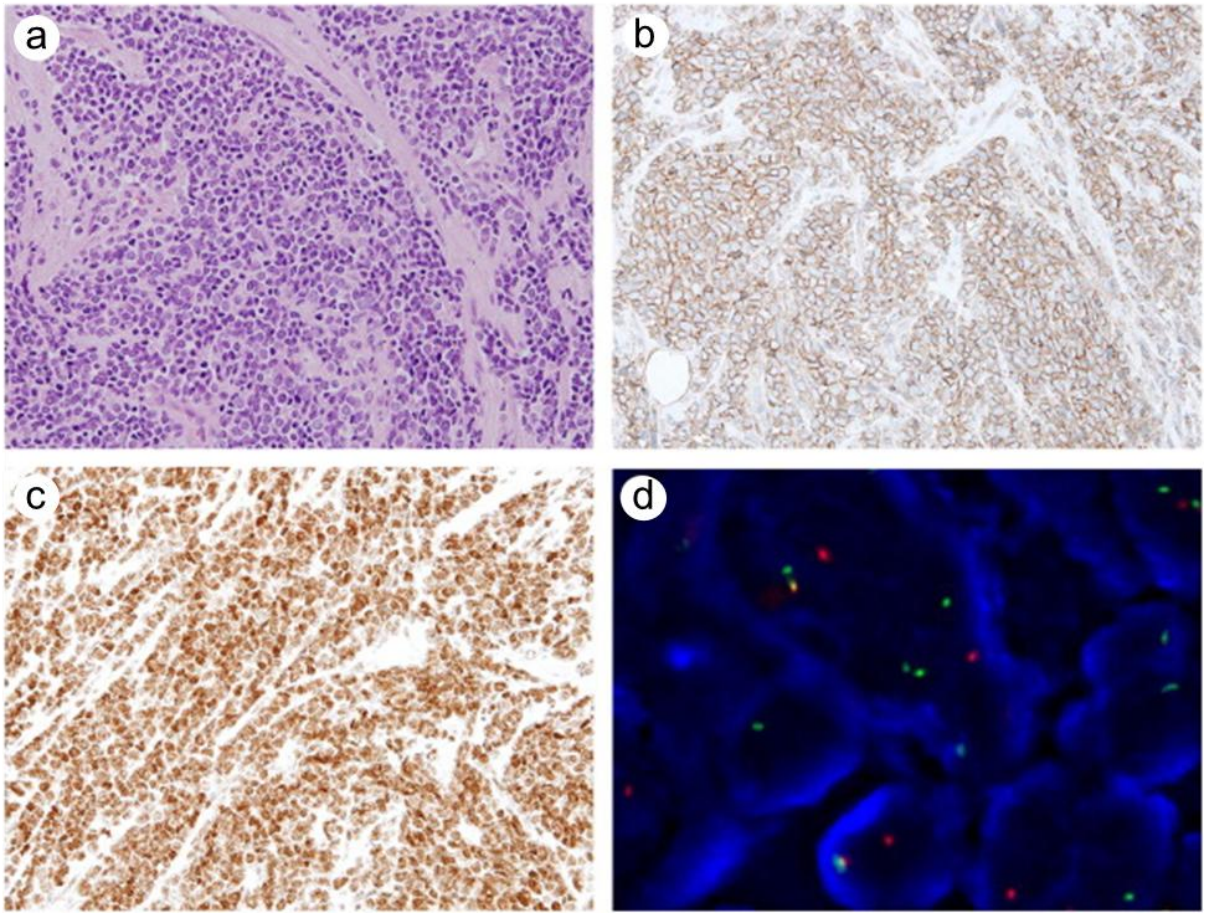

Figure 1.2 Diagnostic features of EwS using IHC and FISH. a. Small, round tumor cells characterized by scant cytoplasm, round nuclei, and fine chromatin. **b.** CD99-positive tumor cells with diffuse and membranous patterns. **c.** Strong nuclear staining for FLI1 in the tumor cells. Images at 200× magnification. **d.** FISH assay result for *EWSR1* break-apart showing separated green and orange signals. Image at 1,000× magnification. Figure adapted from: Kim & Park (2016), PMID: 27246176, through copyright license number: 6044300126381.

1.3. Molecular signature and genetics of EwS

The formation of fusion genes results from aberrant recombination of chromosomal structures, whereby two or more genes that were originally not adjacent are then fused together. These new genes are transcribed and translated to form fusion proteins that affect downstream signaling pathways (Tang et al., 2025). Such processes often give rise to the aberrant activation or deactivation of intracellular signaling pathways, which is a significant contributing factor in the development of cancer (Dai et al., 2018; Tang et al., 2025). The main driver of oncogenesis in EwS is the *FET::ETS* fusion, the end product of abnormal chromosomal rearrangement. As previously described, the most common fusion in EwS is the one between genes *EWSR1* and *FLI1*, t(11;22)(q24;q12) (Delattre, et al., 1992), while many other translocation partners are

also possible within the family of FET genes and ETS transcription factors (Grunewald et al., 2018). Such ETS family members that can substitute *FLI* in rare cases are: FEV transcription factor, ETS family member (*FEV*) (Peter et al., 1997), ETS variant transcription factor 1 (*ETV1*) and ETS variant transcription factor 4 (*ETV4*) (Urano et al., 1998). Similarly, given the homology between the TET family genes, rare cases of EwS, fusion variants harbor FUS RNA binding protein (*FUS*) instead of *EWSR1* gene (**Figure 1.3**) (Boone et al., 2021a; Grunewald et al., 2018). Furthermore, a broader group referred to as 'Ewing sarcoma family tumors' have non-canonical *EWSR1* fusions to non-ETS partners, including nuclear factor of activated T cells 2 (*NFATC2*), POZ/BTB and AT hook containing zinc finger 1 (*PATZ1*), Sp3 transcription factor (*SP3*), and SNF2 related chromatin remodeling ATPase 5 (*SMARCA5*) (Antonescu & Dal Cin, 2014). Such tumors are morphologically indistinguishable from EwS and are currently treated on Ewing-specific regimens (Jo, 2020).

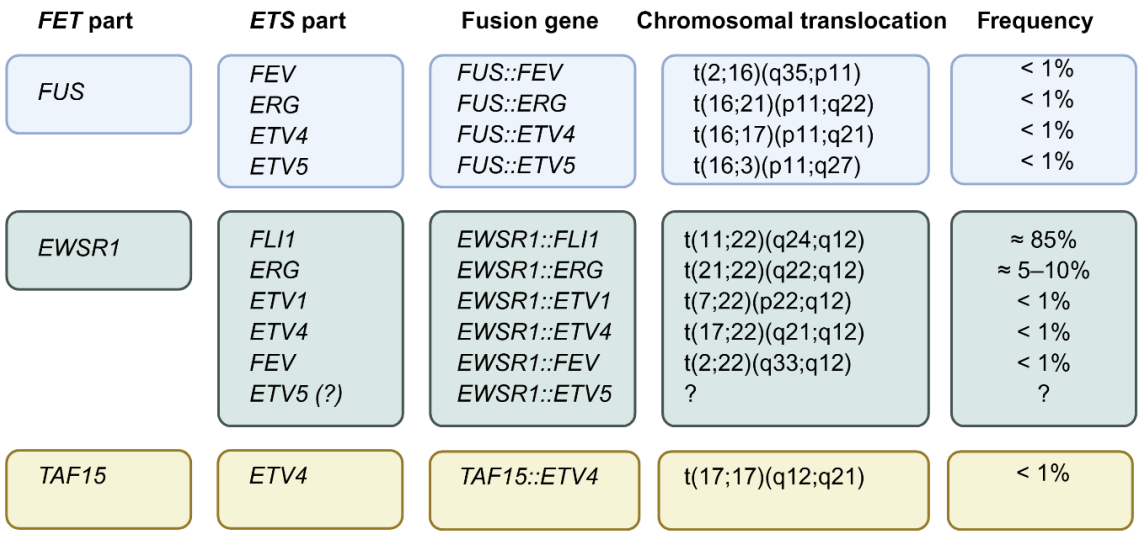

Figure 1.3 Fusion partners in EwS, FET::ETS family of genes. Oncogenic translocations in EwS include a member of the FET gene family (*FUS*, *EWSR1* or *TAF15*) in combination with a member of the ETS family of transcription factors (such as *FLI1*, *ERG*, *ETV1*, *ETV4* and *FEV*). The figure was adapted from Grunewald et al. (2018), PMID: 29977059, copyright license number: 6043070238889, with integration of several novel fusions discovered since then, such as *FUS::ETV4* (Boone et al., 2021a), *TAF15::ETV4* (Picard et al., 2022) and *FUS::ETV5* (Dehner et al., 2025). Although the *EWSR1::ETV5* gene fusion has not yet been reported in EwS, its occurrence remains plausible due to the significant structural resemblance between members of the FET and ETS family members.

Genes that are constituents of EwS genetic fusions have many roles in healthy cells, however once part of the fusion, they preserve some of its canonical roles as well as evolving entirely new, neomorphic functions. However, it is worth noting that some of the preserved

functions might be aberrantly activated, whether in the wrong time or at the wrong place within the cell (Muthahari et al., 2025; Thang et al., 2025).

Fusion proteins present in EwS are aberrant transcription factors that interfere with different signaling pathways and target genes, affecting cell proliferation, differentiation, and cell death (Thang et al., 2025). Such aberrant activity of transcriptional regulators can completely rewire the physiological cellular signaling. Divergent chromatin remodeling caused by EWSR1::FLI1 in EwS includes both mechanisms of direct activation and repression of enhancer elements. Accordingly, there are two distinct classes of motifs that are preferred fusion protein binding sites in the human genome (**Figure 1.4**) (Riggi et al., 2014). The first are GGAA-microsatellites, dispersed across the human genome, varying in some places from two to several consecutive GGAA-microsatellite repeats. This implies the possibility of the fusion protein binding essentially across the length of the genome, wherever such microsatellites are present (Tak et al, 2022). The number of repeats ('sweet spot' length) influences binding and transcriptional activation (Gangwal et al., 2008). Johnson et al. (2017) described that microsatellites with 18–26 repeats represent a 'sweet spot' that is particularly effective in driving EWSR1::FLI1 mediated gene expression. While Orth et al. (2022) further defined this binding, indicating that long consecutive GGAA microsatellites on both alleles increase the probability of EWSR1::ETS-binding compared with loci containing only one 'long' allele.

Secondly, there are canonical non-repetitive ETS motifs, conserved sequences and binding sites still preserved from native FLI1 activity. The preferred high-affinity binding sequence for FLI1 is 'ACC**GGAA**GTG', while other family members bind similar sequences containing a 'GGA(A/T)' core surrounded by additional base pairs (Boone et al., 2021b). Through binding canonical ETS motifs, EWSR1::FLI1 directly represses targets transcription by displacing wild-type ETS factors from mesenchymal enhancers (**Figure 1.4**) (Riggi et al., 2014).

Both GGAA-microsatellites and canonical ETS motifs are recognized by the same ETS DNA-binding domain (DBD) within the FLI1 or ERG part of the respective fusion protein. This domain is conserved from the wild-type FLI1/ERG protein, which naturally recognizes and binds ETS consensus sequences. Genome-wide ChIP-seq and chromatin mapping studies show that EWSR1::FLI1 binding at GGAA-microsatellites, which are neomorphic enhancer activating motifs, result in gene upregulation, while EWSR1::FLI1 binding to ETS motifs is context-dependent and can result in either repressive or enhancing effect on adjacent genes

(Boone et al., 2021b; Orth et al., 2022). Recently, a study on repressive functions of EWSR1::FLI1 showed that the fusion regulated metastasis-related cell movement, through binding to the ETS proto-oncogene 1, transcription factor (*ETS1*) locus and deposition of the repressive H3K27me3 chromatin marks (Ebegboni et al., 2024).

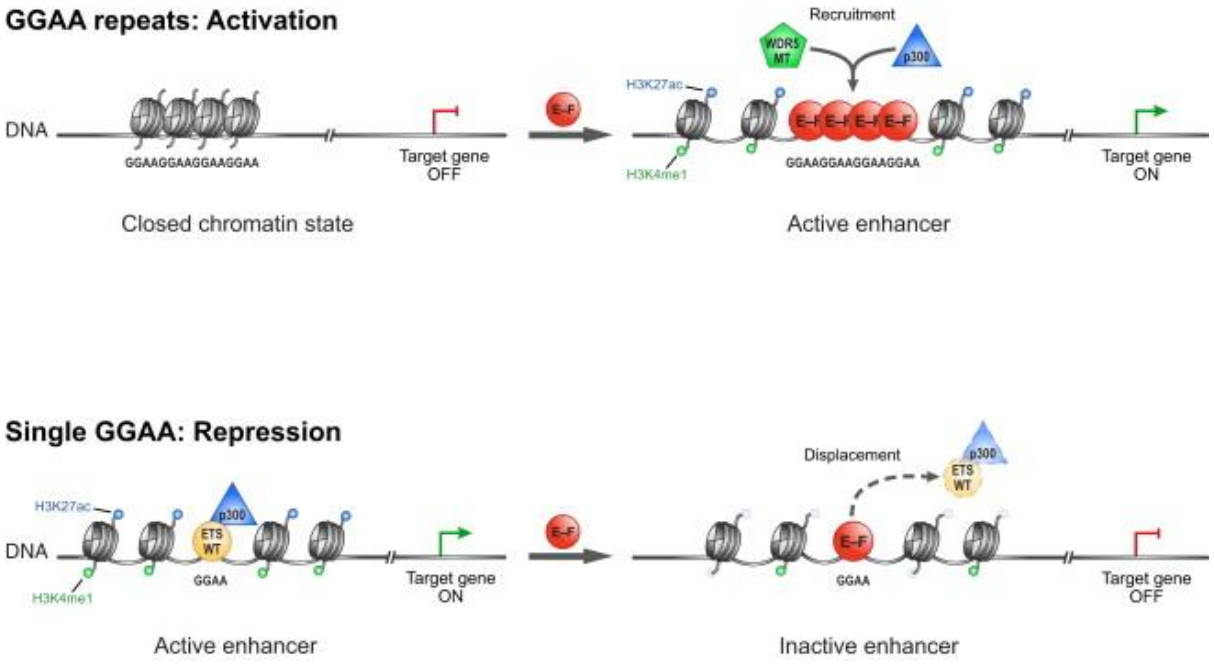

Figure 1.4 Enhancer remodeling mechanisms mediated by EWSR1::FLI1. This schematic depicts two different chromatin remodeling processes underlying the dual transcriptional roles of EWSR1::FLI1: enhancer activation and induction involving recruitment of WD repeat domain 5 (WDR5) and EP300 lysine acetyltransferase (p300) at GGAA repeats (top), and enhancer repression characterized by displacement of native ETS transcription factors and p300 at single GGAA canonical ETS motifs (bottom). Figure reprinted from: Riggi et al. (2014), PMID: 25453903, through copyright license number: 6043061062270.

Historically, much research has been centered on the transcriptional roles of oncogenic sarcoma fusion proteins, but there is emerging evidence that EWSR1::FLI1 has important functions beyond classic transcriptional regulation, including post-transcriptional roles (Yu et al., 2023). One of such roles is the ability of EWSR1::FLI1 to regulate alternative splicing. Alternative splice variants of genes that potentially regulate oncogenesis, including CDC like kinase 1 (*CLK1*), caspase 3 (*CASP3*), PPFIB scaffold protein 1 (*PPFIBP1*), and telomerase reverse transcriptase (*TERT*), were found to be regulated by EWSR1::FLI1 (Selvanathan et al., 2015). Also, in a CLIP-seq experiment, it was found that EWSR1::FLI1 RNA-binding motifs most frequently occur adjacent to intron-exon boundaries. EWSR1::FLI1 also alters splicing by directly binding to known splicing factors including DEAD-box helicase 5 (DDX5),

heterogeneous nuclear ribonucleoprotein K (hnRNP K), and pre-mRNA processing factor 6 (PRPF6) (Selvanathan et al., 2015). Additionally, EWSR1::FLI1 can also influence mRNA stability and degradation rates. Confirming this, France et al. (2011) found that EWSR1::FLI1 decreased the transcript half-life of insulin-like growth factor binding protein 3 (*IGFBP3*), a down-regulated direct target gene in human tumor-derived EwS cell lines. They also demonstrated that both EWS and ETS domains are required for modulation of both transcript synthesis and degradation (France et al., 2011). Moreover, EWSR1::FLI1 was found to regulate the subcellular localization of proteins. This was shown for forkhead box O1 protein (FOXO1), which was excluded from the nucleus in the presence of EWSR1::FLI1 (Niedan et al., 2013). Thus, EWSR1::FLI1 exerts oncogenic effects in EwS not only by regulating transcription but also by modulating RNA splicing, mRNA stability, chromatin structure, and even the localization and function of other proteins. These multifaceted roles are integral to its ability to drive tumorigenesis.

While pediatric cancers usually lack the mutational burden of adult cancers, they still exhibit high levels of cellular heterogeneity that are largely mediated by epigenetic mechanisms (Apfelbaum et al., 2022). EwS is a genetically rather simple tumor mainly driven by EWSR1::ETS fusions, where somatic mutations are rare (Brohl et al., 2014). The most common somatic mutations are mutations in genes: STAG2 cohesin complex component (*STAG2*) in 17%, cyclin dependent kinase inhibitor 2A (*CDKN2A*) in 12%, and in tumor protein p53 (*TP53*) in 7% of EwS cases (Tirode & Surdez et al., 2014). EwS tumors with mutations in *TP53* often display resistance to radiotherapy, and patients with these mutations have significantly worse outcomes, especially when co-occurring with mutations in *STAG2* (Kim et al., 2023; Tirode & Surdez et al., 2014). While mutations in *STAG2* and deletions of *CDKN2A* rarely occur together, the impact of mutations in *CDKN2A* alone is less well characterized (Tirode & Surdez et al., 2014). Furthermore, multiple studies, have shown that mutations in *STAG2* or its loss of function in EwS is strongly associated with increased metastatic potential, altered chromatin architecture, and worse prognosis (Adane et al., 2021; Giménez-Llorente et al., 2024; Surdez et al., 2021).

1.4. Alterations in cell signaling promoting invasion and metastasis in EwS

Metastasis is the hallmark of cancer that is responsible for the greatest number of cancer-related deaths. Yet, it remains poorly understood (Fares et al., 2020). Metastatic spread is a highly

complex multistep cascade of evolutionary events performed with exquisite, but fatal, consistency across patients (Bull et al., 2025). The development of metastases requires cancer cells to leave their primary site (invasion), enter the bloodstream (intravasation), endure pressure in blood vessels (circulation), acclimate to new cellular surroundings in a secondary site (extravasation and colonization), and escape immune cells (Fares et al., 2020). In carcinomas, this is facilitated by tumor cells undergoing an epithelial-to-mesenchymal transition (EMT) which reduces their adhesion properties and enhances their migratory and invasive abilities. Once cells reach their destination, they undergo a reverse process termed mesenchymal-to-epithelial transition (MET) to establish metastases (Damerell et al., 2021).

In contrast to carcinomas, EMT processes in sarcomas are largely unknown and appear paradoxical since they are, by definition, already mesenchymal in nature (Damerell et al., 2021). Nonetheless, it has been proposed that sarcoma cells may reside in a metastable state, and depending on cellular context, can either differentiate towards an epithelial or more mesenchymal phenotype. This EMT/MET plasticity has been has been associated with increased tumor aggressiveness, and several EMT/MET transcription factors have been shown to play a role in the development and progression of sarcomas (Damerell et al., 2021; Sannino et al., 2017). First efforts to describe and understand the process of metastasis in sarcomas, come from studies of cellular plasticity. Those studies, highlight the importance of both epithelial and mesenchymal characteristics that make EwS cells competent for metastasis. On the example of transcription factor, zinc finger E-box binding homeobox 2 (ZEB2), it was shown that ZEB2 acts as a repressor of epithelial differentiation in EwS and works in conjunction with EWSR1::FLI1, which in turn acts as a repressor of mesenchymal differentiation. This bidirectional process keeps EwS cells in an undifferentiated state and they retain access to features of both epithelial and mesenchymal cells, which sets them for successful growth and metastasis (Wiles et al., 2013).

1.4.1. Oscillatory fusion behavior and EwS metastasis

Changes in the expression and activity of the EWSR1::FLI1 fusion protein is a central component of EwS tumor cell plasticity. Studies have shown that different levels and/or activity of fusion protein expression drive heterogeneity within the tumor, leading to distinct cellular phenotypes (Adane et al., 2021; Aynaud et al., 2020; Chaturvedi et al., 2012; Chaturvedi et al., 2014; Franzetti et al., 2017; Surdez et al., 2021; Willis et al., 2013). In EwS, the majority of tumor cells have high fusion protein expression and are highly proliferative.

Conversely, a minority of cells within the tumor have reduced transcriptional activity and expression of EWSR1::FLI1, displaying a more mesenchymal, migratory phenotype, and are associated with increased metastatic potential. In sum, EWSR1::FLI1-high cells have an enhanced ability to grow and proliferate, while EWSR1::FLI1-low cells have a more migratory, EMT and metastatic-like phenotype, reflecting a shift in cell state (**Figure 1.5**). This plasticity is primarily regulated through epigenetic mechanisms rather than genetic mutations, enabling tumor cells to dynamically adapt and transition between different phenotypic states in response to intrinsic and extrinsic cues (Franzetti et al., 2017).

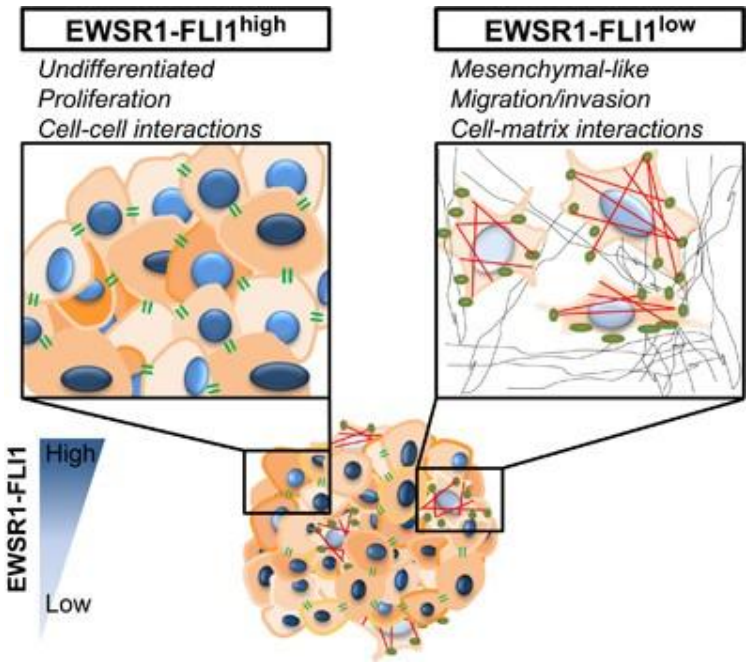

Figure 1.5 Model of EwS cell dissemination, based on cell-to-cell heterogeneity of EWSR1::FLI1 expression. In this model, undifferentiated EWSR1::FLI1-high cells proliferate with strong cell-cell adhesion, whereas mesenchymal-like EWSR1::FLI1-low cells migrate and invade environment through important cell-matrix interactions. Figure reprinted from: Franzetti et al. (2017), PMID: 28135250. Licensed under a Creative Commons Attribution-NonCommercial-NoDerivs 4.0 International License, whereas reuse of this material for non-commercial/educational purposes is possible without obtaining additional permission from Springer Nature.

1.4.2. Cell signaling pathways in EwS metastasis

One of the most significant pathways influencing the tumor invasiveness and metastatic potential are developmental signaling pathways. Some of those that are aberrantly activated in EwS include: Sonic Hedgehog (ShH) (Beauchamp et al., 2009), Wnt/β-catenin (Pedersen et al., 2016), TGF-β (Saratov et al., 2022) and Hippo pathway (Bierbaumer et al., 2021).

Sonic Hedgehog (ShH) pathway has unconventional activation in EwS. Usually this pathway is activated through Shh ligand binding to the Patched receptor and activating the downstream cascade that culminates in increased function of the GLI family of transcription factors (Lessnick & Ladanyi, 2012). However, in EwS the ShH pathway is not activated at the ligand-receptor level. Subsequent studies demonstrated a pathway in which EWSR1::FLI1 directly binds and upregulates the GLI family zinc finger 1 (*GLI1*) promoter while GLI1, in turn, upregulates NKX2-2 (Beauchamp et al., 2009). Thus, activated NKX2-2 (induced by EWSR1::FLI1), promotes tumor survival and progression (Smith et al., 2006).

Wnt/β-catenin signaling is active in small subpopulations of EwS cells, and those display a more metastatic phenotype, that is reminiscent of EWSR1::ETS-low cells. Specifically, activation of Wnt/β-catenin induces alterations to the actin cytoskeleton, acquisition of a migratory phenotype, and upregulation of EWSR1::ETS repressed genes (Pedersen et al., 2016). Furthermore, these β-catenin-activated EwS cells also alter secretion of extracellular matrix (ECM) proteins that promote angiogenesis but also induction of the angiomatrix by Wnt/β-catenin-active tumor cells is dependent on TGF-β (Hawkins et al., 2020).

In EwS, transforming growth factor beta (TGF-β) signaling is tightly connected to the tumor microenvironment (TME). Even though relatively underexplored in EwS, TME plays a crucial role in the progression of the disease, resistance to therapy, and metastasis (Volchenboum et al., 2015). Here, bone environment and bone remodeling signals may have a big impact in the development of EwS, since EwS most often arises during adolescence and young adulthood, coinciding with rapid bone remodeling and increased bone mass (Saggese et al., 2002). Furthermore, more than 80% of EwS originates in bone, a unique and biochemically distinct local environment, where EwS patients with primary bone tumors tend to have worse prognosis compared to those with extra-skeletal EwS (Applebaum et al., 2011), as well as those with bone metastases versus lung-only metastases (Gaspar et al., 2015). Bone remodeling releases various factors, such as TGF-β, Insulin-Like Growth Factor (IGF), and Wnt ligands that are essential for osteoblast and osteoclast regulation, but can also influence tumor behavior. EWSR1::FLI1 expression plays an important role in regulating the sensitivity of EwS cells to these bone-derived signals (Apfelbaum et al., 2022). Namely, EWSR1::FLI1 represses transforming growth factor beta receptor 2 (TGFBR2), which then inhibits TGF-β pathway activation, ECM gene expression and protein secretion as well as pro-migratory signaling in EWSR1::FLI1-high cells (Pedersen et al., 2016; Hawkins et al.,2020). Conversely, activation

of Wnt/β-catenin signaling can activate TGFBR2 expression and mimic a more migratory EWSR1::FLI1-low state. Increases in Wnt activity lead to increased secretion of TGF-β ligands as well as ECM proteins from tumor cells that contribute to an angiogenic and pro-tumorigenic TME in EwS (Apfelbaum et al., 2022; Hahm et al., 1999; Pedersen et al., 2016). Also, TGF-β co-receptor endoglin, an endothelial cell marker, expression in EwS is associated with increased tumor cell plasticity, invasiveness, and poor prognosis (Pardali et al., 2011).

Main downstream effectors of the Hippo signaling pathway are Yes1 associated transcriptional regulator (YAP) and its paralog transcriptional coactivator with PDZ-binding motif (TAZ) (Guo & Teng, 2015). In Ews it was found that TAZ levels increase in the migratory EWSR1::FLI1-low state and are associated with adverse prognosis in EwS patients (Bierbaumer et al., 2021). It has been reported that YAP and TAZ are commonly upregulated in many human cancers, providing attractive therapeutic targets (Guo & Teng, 2015). Verteporfin, the potent YAP/TAZ/TEAD complex inhibitor, suppressed expression of EWSR1::FLI1 regulated cytoskeletal genes involved in actin signaling to the ECM, effectively blocked F-actin and focal-adhesion assembly, and inhibited EwS cell migration at submicromolar concentrations, as well as reduced relapse and delayed lung metastasis *in vivo*. These data suggest that YAP/TAZ pathway inhibition may prevent EwS cell dissemination and metastasis, justifying further preclinical development of YAP/TAZ inhibitors for EwS treatment (Bierbaumer et al., 2021; Chaturvedi et al., 2014).

The actin cytoskeleton plays an important role in the biology of EwS, particularly in cell adhesion, morphology, migration, and metastasis. The top three classes of genes that are repressed by EWSR1:FLI1 are categorized as genes related to structure and function of focal adhesions, ECM receptor interactions, and regulation of the actin cytoskeleton. In EWSR1::FLI1-low state there is a dramatic restoration of actin cytoskeletal organization, increased cell spreading, and enhanced formation of actin stress fibers. EWSR1::FLI1-induced repression of α5 integrin and zyxin expression promotes tumor progression by supporting anchorage-independent cell growth (Chaturvedi et al., 2014). Furthermore, reduced expression of EWSR1::FLI1 is associated with the increase of actin-binding proteins implicated in cell contractility, cytoskeleton assembly and maintenance but also the decrease of cell-cell adhesion proteins such as tight junctions and desmosome family proteins. Indeed, EWSR1::FLI-low cells have increased three-dimensional migration and invasion properties (Franzetti et al., 2017). As well, EWSR1::FLI1 strongly represses the activity of the Rho-F-actin signal pathway transcriptional effector myocardin related transcription factor B (MRTFB), affecting the

expression of many EWSR1::FLI1-negatively correlated genes including structural and regulatory cytoskeletal genes. EWSR1::FLI1 suppresses the Rho-actin pathway by perturbation of a MRTFB/YAP-1/TEAD transcriptional module, which directly affects the actin-autoregulatory feedback loop, and provides a mechanistic basis for the underlying EWSR1::FLI1-dependent reversible cytoskeletal reprogramming of EwS cells (Katschnig et al., 2017).

Furthermore, cancer cells must overcome anoikis (detachment-induced cell death) to successfully metastasize. Recently, it has been found that distinct oncoproteins upregulate IL1 receptor accessory protein (IL1RAP) to suppress anoikis (Zhang et al., 2021a). IL1RAP is directly induced by oncogenic fusions of EwS. IL1RAP inactivation triggers anoikis and impedes metastatic dissemination of EwS cells (Zhang et al., 2021a).

Finally, one of the important steps for successful metastatic dissemination is immune evasion. EwS is an immunologically cold solid tumor, meaning it has low immunogenicity and limited immune cell infiltration, which contributes to its ability to evade immune detection and destruction. Some of the mechanisms of immune evasion in EwS include few tumor-specific antigens, low expression of major histocompatibility complex class I (MHC-I) antigen-presenting molecules, accumulation of immunosuppressive M2 macrophages and myeloid proinflammatory cells, and release of extracellular vesicles which are capable of reprogramming host cells in the tumor microenvironment and systemic circulation. The development of efficient immunotherapies in immune-inert pediatric sarcomas requires addressing both the tumor cell itself and the TME (Evdokimova et al., 2022). However, there is recent evidence that sheds the light on immunology of EwS and opens a door of opportunity for immune therapies. Single-cell sequencing of 18 EwS primary tissue samples showed that EwS is infiltrated by natural killer, T, and B cells, dendritic cells, and immunosuppressive macrophages. EwS-associated T cells show various degrees of dysfunction. The antigen-presenting cells found in EwS lack costimulatory gene expression, implying functional impairment. Interaction analysis reveals a clear role of EwS tumor cells in turning the EwS immune microenvironment into an immunosuppressive niche (Visser et al., 2023). Furthermore, single-cell RNA sequencing and immunofluorescence of circulating tumor cells (CTCs) at the time of EwS diagnosis identified tetraspanin 8 (TSPAN8) as a potential therapeutic target. This study identified that CTCs have lower enrichment of gene signatures associated with EwS compared to matched primary cells, supporting the fact that low EWSR1::FLI1 activity leads to more metastasis. Finally, they showed that a transmembrane

protein TSPAN8 was highly enriched in the CTCs, and its expression was not restricted solemnly to the CTCs but also was highly and broadly expressed in primary EwS (Goodspeed et al., 2025). In addition, characterization of the surfaceome of EwS, revealed pregnancy-associated plasma protein A (PAPP-A) as a highly differentially expressed therapeutic target. PAPP-A is a cell membrane-associated proteinase produced by the placenta that promotes fetal growth by inducing IGF signaling. This study discovered a novel link between insulin like growth factor 1 (IGF-1) signaling and immune evasion in cancer, thus implicating shared mechanisms of immune evasion between EwS and the placenta (Heitzeneder et al., 2019). Similarly, amyloid precursor-like protein 2 (APLP2) has been implicated in the survival of cancer cells, including EwS cells. APLP2 lowers the sensitivity of EwS cells to radiotherapy-induced apoptosis and enables EwS cells survive exposure to cytotoxic immune cells (Peters et al., 2013). In sum, these results indicate promising targets in the field of TME and immunology of EwS, which are both important in the scope of metastatic tumor progression.

The field of EwS metastasis is slowly developing but is still to some extent underexplored. The area still lacks substantial knowledge that would closer clarify the biology of EwS metastatic cells or discover novel biomarkers for metastatic disease. As a result of that, there is a lot of potential for unexplored and novel molecular targets that have yet have to be discovered.

1.5. LIM-domain protein 7 (LMO7)

LIM domain proteins are involved in a wide range of cellular functions, including transcription, cytokinesis, adhesion, and motility. They contain a highly conserved LIM domain that consists of two zinc fingers while the rest of the protein can be highly variable (Matthews et al., 2013). Many LIM proteins localize to focal adhesions and adherens junctions where they function as molecular scaffolds mediating cell adhesion. Additionally, these proteins can influence specific signaling pathways from these cytoskeletal structures, by modulating the localization, expression or activity of signaling molecules, such as focal adhesion kinase (FAK), Rho, and mitogen-activated protein kinase (MAPK), that promote cell migration, proliferation, and apoptosis (Sala & Oakes, 2023). While LIM proteins are primarily recognized for their role in organizing the actin cytoskeleton, they also take part in gene transcription regulation. They shuttle between the cytoplasm and the nucleus, amongst other as a consequence of triggering cells with ligands of nuclear receptors. LIM domain proteins act as important co-regulators of

nuclear receptor-mediated gene transcription, in which they are functioning either as coactivators or as corepressors (Sala & Ampe, 2018). Through both cytoskeleton organization and transcription regulation, LIM domain proteins have important cellular roles in processes that are relevant to cancer such as self-renewal, cell cycle regulation and metastasis (Matthews et al., 2013).

LIM domain 7 protein (LMO7) is a multifunctional PDZ-LIM protein that has several distinct functional domains, including a LIM domain, a calponin homology (CH) domain, a PDZ domain and an F-box (FBX) domain, that together enable it to have a vast variety of distinct protein-protein interactions, related to wide-ranging and multi-compartmental cell functions (Gomes et al., 2021). For instance, PDZ-LIM proteins are known to mediate signaling between the nucleus and the cytoplasm, sequester nuclear factors to the cytoplasm and interact with actin microfilaments (Krcmery et al., 2010). In addition, they facilitate the assembly of protein complexes, regulate gene transcription, control mitosis progression, influence spindle assembly checkpoint besides being involved in the ciliary function (Gomes et al., 2021).

LMO7 is an emerin-binding protein that regulates the transcription of emerin and other muscle-relevant genes as well as genes implicated in X-linked Emery-Dreifuss muscular dystrophy (Holaska et al., 2006). Aside from binding emerin in the nuclear envelope, in studies done in mice, Lmo7 was shown to be a scaffold protein that regulates crosstalk between apical junctions and the actomyosin system. Here, Lmo7 binds non-muscle myosin II (NMII) and recruits it to apical junctions which is essential for Lmo7-mediated apical constriction and requires the Rho-ROCK-NMII pathway (Matsuda et al., 2022). Furthermore, Lmo7 is essential for effective myoblast differentiation, as competitive emerin binding to Lmo7 inhibited Lmo7 binding and activation of the myoblast determination protein 1 (MyoD) and paired box 3 (Pax3) promoters (Dedeic et al., 2011). Also, in hair cells of the inner ear, LMO7 organizes the cuticular plate and F-actin network, essential for hearing. Deficiency leads to hearing loss due to disrupted cytoskeletal architecture (Du et al., 2019). In the renal epithelial barrier, LMO7 is associated with the cell-cell junctional complex and cortical F-actin, where it regulates FAK during osmotic pressure. Here LMO7 depletion in cells resulted in junctional integrity loss and excessive FAK activation (Zhen et al., 2022). Finally, LMO7 was described to interact with activator protein 1 transcription factor (AP-1) subunits c-FOS and c-JUN, promoting their ubiquitination and degradation, disrupting AP-1 dependent TGF-β autoinduction in wound healing and fibrotic processes (Xie et al., 2019).

Cancer is a multifaceted disease characterized by the dysregulation of numerous genes and pathways. Among these, LMO7 has emerged as a significant player in various cancer types, gaining substantial attention for its involvement in tumorigenesis and cancer progression (Zeng et al., 2025). There is currently no data in the literature on the role of LMO7 in EwS. However, LMO7 was earlier described as an important factor in promoting pancreatic (Liu et al., 2021) and breast cancer progression and metastasis (Hu et al., 2011). It has also been shown that LMO7 acts as a facilitator in driving immune evasion by promoting regulatory T cell differentiation and chemotaxis, and inhibiting CD8+ T and natural killer cells in pancreatic ductal adenocarcinoma (Dai et al., 2025). Furthermore, *LMO7* was found to form fusions with ALK receptor tyrosine kinase (*ALK*) in non-small cell lung cancer (Yang et al., 2022), while in papillary thyroid carcinoma, *LMO7* formed fusions with the B-Raf proto-oncogene, serine/threonine kinase (*BRAF*), where it also increased extracellular-signal-regulated kinase (ERK) phosphorylation and promoted anchorage-independent cell growth (He et al., 2018). Conversely, high LMO7 expression was shown to correlate with better overall survival in oropharyngeal squamous cell carcinoma (Israelsson et al., 2024), and in several studies with lung cancer (Nakamura et al., 2011, Karlsson et al., 2018 and Giannos et al., 2021), hinting to a context-dependent role of LMO7, earlier also suggested for many other LMO proteins (Matthews et al., 2013).

Additionally, *LMO7* mRNA transcript has been found to be alternatively spliced in the region of exons 3–5 and circularly covalenty bound, shaping circular *LMO7* RNA, *circLMO7* (Luo et al., 2024). *circLMO7* was shown to be important for inhibiting myoblast differentiation (Wei et al., 2017) and in osteosarcoma development (Luo et al., 2024).

In sum, LMO7 is a versatile scaffold protein essential for cytoskeletal organization, cell adhesion, signaling, gene regulation, and immune modulation (**Figure 1.6**). Its dysregulation is implicated in cancer, muscle diseases, hearing loss, and immune evasion, making it a potential biomarker and therapeutic target in multiple diseases.

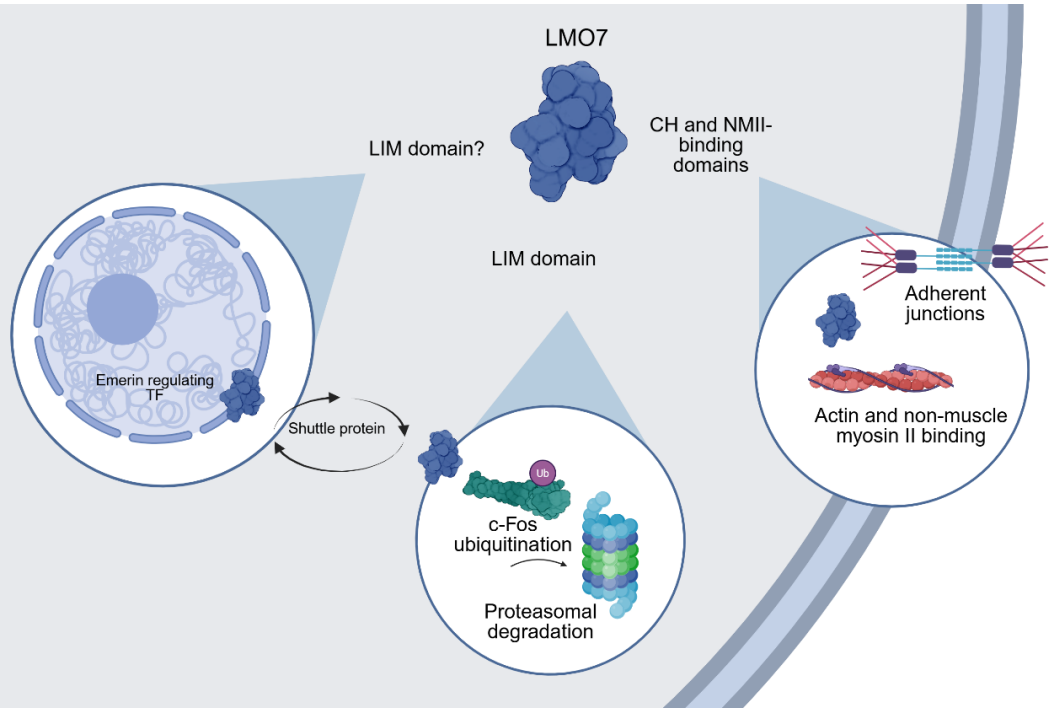

Figure 1.6 Multifunctional and multifaceted protein LMO7, and some of its roles in the cells. LMO7 is involved in regulation of muscle relevant genes like emerin (left panel) most likely through its LIM domain which is part of C-terminal region of LMO7 and has been described as sufficint to directly bind emerin *in vitro* (Holaska et al., 2006). LMO7 is also involved in ubiquitination and degradation of AP-1 complex subunits c-JUN and c-FOS (middle panel) through its LIM domain. And through its CH and NMII-binding domains, LMO7 acts as a scaffold protein that regulates crosstalk between apical junctions and the actomyosin system (right panel). Figure was designed by integrating the data from: Holaska et al. (2006), Xie et al. (2019), Du et al. (2019), Zhen et al. (2022) and Matsuda et al. (2022).

1.6. Integration of multi-omics technologies in translational cancer research

Translational cancer research (TCR) is pivotal in bridging the gap between fundamental cancer biology and clinical oncology, leading to significant advancements in cancer diagnosis, treatment, and patient outcomes. Integrating multi-omics data into TCR offers unique prospects to comprehend the underlying biology of complex diseases like cancer. Multi-omics technologies are advantageous in understanding tumor biology, tumor classifications, diagnostics, and tumor prognosis (Chakraborty et al., 2024).

Multi-omics refers to the comprehensive analysis of cellular components, including genomics (DNA), transcriptomics (RNA), epigenomics (epigenetic modifications), proteomics (proteins), and metabolomics (metabolites) (Yates & Van Allen, 2025). In recent years, multi-omics technologies have been developed to study cancer at the single-cell level. Tumor heterogeneity is a hallmark of cancer, and single-cell sequencing has enabled its study with

remarkable resolution. Historically, bulk sequencing averaged measurements across tissues, masking the complexity of individual cellular interactions. Breakthroughs in single-cell sequencing and spatial profiling have deepened our understanding of tumor biology, especially through multi-omics approaches resolution (Zhu et al., 2020). These technologies provide insights into the levels of complexity of malignant cells and the TME, as well as their spatial organization and interactions. While bulk technologies capture inter-tumor heterogeneity, intra-tumor heterogeneity requires single-cell and spatial profiling. Integrative multi-omics approaches have enabled a holistic view of tumor biology, driving progress in understanding cancer at unprecedented depth (Yates & Van Allen, 2025).

Recent advances in spatial transcriptomics sequencing technologies have enabled precise quantification and visualization of gene expression within the spatial context of tissues. Unlike conventional transcriptomic approaches, these methods provide not only expression profiles at the cellular level but also critical insights into the spatial location of gene expression within tissues, cellular composition of biological tissues, interactions between cells and TME, and cell heterogeneity (Jin et al., 2024). This technology enables identification of diverse molecular profiles across tumor regions, crucial for understanding and visualizing tumor heterogeneity, cancer evolution, treatment response, and therapeutic resistance. Equally, they are important tools for uncovering spatially regulated biomarkers and therapeutic targets in tumors, aiding in the development of personalized treatments tailored to patients (**Figure 1.7**) (Chakraborty et al., 2024). Also, spatial omics technologies are of immense value for mapping tumor-host interactions and dynamics of metastatic dissemination. By examining spatial relationships among cancer cells, normal tissue, and metastatic niches, these approaches provide valuable insights into the mechanisms underlying invasion, angiogenesis, and the establishment of metastases (Chakraborty et al., 2024).

Finally, omics approaches, especially spatial and single-cell technologies, are helping to unravel the intra- and inter-tumor heterogeneity and could be of remarkable use in EwS research, knowing that the main driver of EwS, FET::ETS fusion, is heterogeneously expressed within tumor tissue (Franzetti et al., 2017). Integrating such technologies combined with patient material and clinical data, generate a powerful tool in bridging the gap between fundamental cancer biology and clinical oncology of EwS, leading to significant advancements in cancer diagnostics, treatment, and patient outcomes.

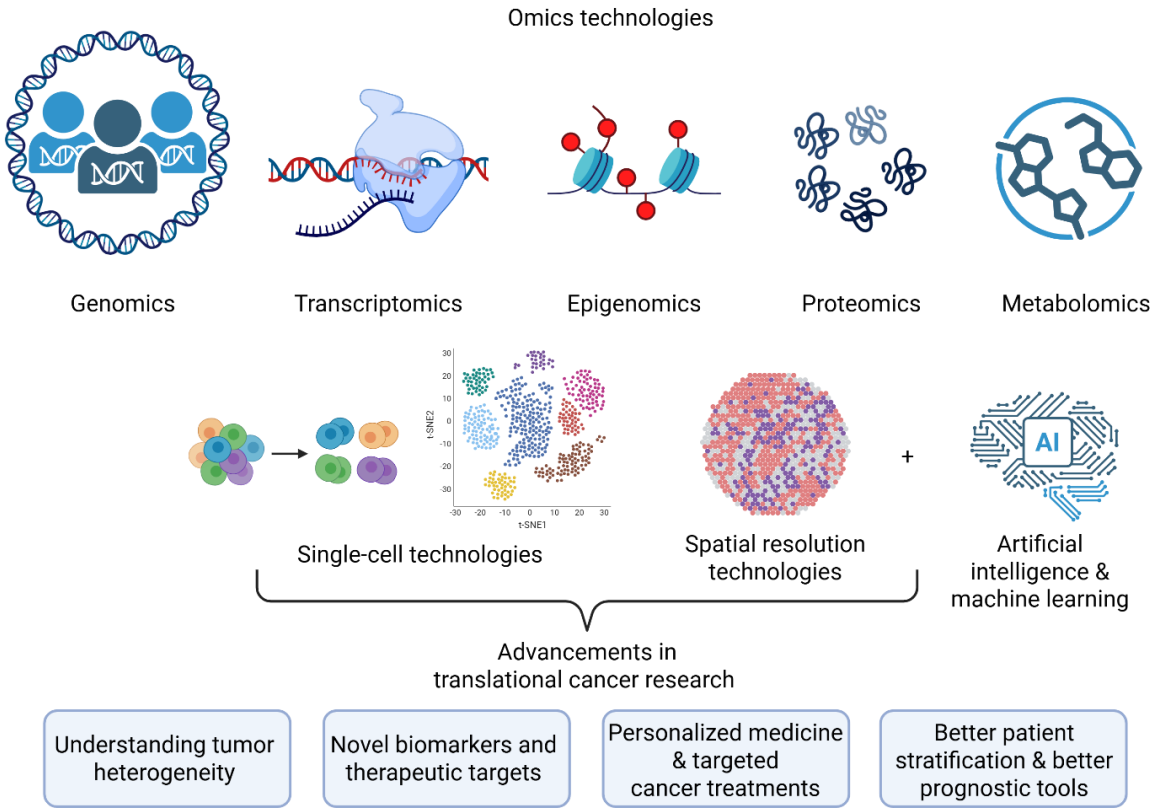

Figure 1.7 Omics technologies and artificial intelligence in translational cancer research. Schematic representation of various omics technologies (genomics, transcriptomics, proteomics, etc.) combined with single-cell and spatial resolution technologies can contribute to enormous advancements in TCR. Combining such technologies generates large datasets that need to be processed and integrated, for which purpose integrating AI and machine learning tools in TCR is essential and time-effective. Figure designed according to the data from: Chakraborty et al. (2024), Zhang et al. (2024), Yates & Van Allen (2025).

2. HYPOTHESIS & OBJECTIVES

2.1. Hypothesis

EwS cells exhibit high degree of heterogeneity and cell plasticity and EwS tumors are aggressive with high metastatic potential. Despite many advances in multi-omics technologies, the mechanisms driving metastasis in EwS remain incompletely understood. To fill the gap in the knowledge and deepen the understanding of metastatic processes in EwS with clinical relevance, this project was designed. Particularly, in the span of this thesis, I investigate the role of fusion-driven clinically relevant genes as potential novel prognostic biomarkers fueling EwS invasion and metastasis.

Hypothesis: Integrative multi-omics approach can be used to identify EWSR1::FLI1 regulated and clinically relevant gene(s) contributing EwS invasion and metastasis.

2.2. Objectives

1. To identify clinically relevant gene(s) correlated with EwS patient survival that are highly expressed in fusion-low cells and at the invasive front of the EwS tumor by utilizing multi-omics integrative approach.

2. To validate such candidate(s) *in vitro* and *in vivo* in EwS models by utilizing doxycycline (Dox)-inducible knockdown (KD) systems.

3. To decipher potential vulnerabilities of fusion-candidate regulated metastatic pathway in EwS.

3. MATERIALS & METHODS

3.1. Cell biology

3.1.1. Cell lines and cell culture conditions

Human EwS cell lines used for the purpose of this thesis were retrieved from the following repositories: A-673 (RRID: CVCL_0080) from American Type Culture Collection (ATCC), MHH-ES-1 (RRID:CVCL_1411) from the German Collection of Microorganisms and Cell Cultures (DSMZ), and TC-32 (RRID: CVCL_7151) from the Children's Oncology Group (COG). Additionally, A-673, MHH-ES-1 and TC-32 cells modified with Dox-inducible construct targeting their FET::ETS fusion were previously generated as part of Ewing Sarcoma Cell Line Atlas (ESCLA) (Orth et al., 2022). Human HEK293T (RRID: CVCL_0063) cells were purchased from DSMZ.

All cell lines were cultured in RPMI-1640 medium with stable L-glutamine and sodium bicarbonate (Sigma-Aldrich, Germany), supplemented with 10% Fetal Calf Serum (FCS) tested to be Dox-free (Sigma-Aldrich), penicillin (100 U/mL) and streptomycin (100 µg/mL; Merck, Darmstadt, Germany) in cell culture flasks and plates (Sarstedt, Germany). Cells were washed with DPBS (1×, Gibco, Thermo Fisher Scientific, Darmstadt, Germany) and trypsinized with 10% trypsin (Anprotec, Bruckberg, Germany). Cells were pelleted at 1,200 rpm, 4 min. Cell lines were routinely tested for Mycoplasma contamination using Mycoplasma PCR Detection Kit (Biozol, Hamburg, Germany) and checked for cell line identity and purity by short-tandem repeat (STR) or single nucleotide polymorphism (SNP) testing.

3.1.2. siPOOL transfections

For transient silencing of *LMO7* expression in EwS cells, siPOOLs (siTOOLs Biotech GmbH, Planegg/Martinsried, Germany) were used consisting of 30 customized siRNAs against *LMO7*, which greatly reduced off-target effects while maximizing on-target effects (Hannus et al., 2014), or a non-targeting control.

For transcriptomic and proteomic analyses, $1{,}4 \times 10^5$ EwS cells were seeded per well of 6-well plates in standard cell culture media in four biological replicates. The following day, cells were transfected with 5 nmol siPOOLs against *LMO7* or a non-targeting control siPOOL for 55 h, using RNAiMax lipofectamine (Thermo Fisher Scientific) in Opti-MEM (Thermo Fisher Scientific) as per manufacturer's recommendation. In brief, for each siPOOL, two

solutions were prepared separately and then mixed in a 1:1 ratio. The first solution contained 0.24 µL siRNA (from 50 µM stock) and Opti-MEM to a total of 237 µL/well for a 6-well plate transfection. The second solution contained 1.97 µL RNAiMax lipofectamine and Opti-MEM, also to a total of 237 µL/well for a 6-well plate. Two solutions were mixed in 1:1 ratio and incubated for 20 min at room temperature (RT). Meanwhile, media was removed, 1891 µL of fresh media added and 473 µL transfection mix added dropwise.

3.1.3. Production of Lentiviruses

Lentiviruses were produced in HEK293T cells using PEI Max (Polysciences, Warrington, PA, USA) and three plasmids: lentiviral packaging plasmid psPAX2 (Addgene, #12260), VSV-G envelope expressing plasmid pMD2.G (Addgene, #12259) and Tet-pLKO-puro (Addgene, #21915) for Dox-inducible expression of shRNA. For optimal production of lentiviruses 5.1 µg Tet-pLKO-puro, 3.4 µg psPAX2 and 1.7 µg pMD2.G were mixed in Opti-MEM to final volume of 500 µL. A second mix was prepared using 30 µL PEI Max (1 g/L) and 470 µL Opti-MEM. After vortexing, the PEI Max solution was added to the plasmid mix and incubated together for 30 min at RT. After incubation, 1 mL of the solution was added dropwise per T75 flask. Cells were incubated for 16 h at 37 °C, after which medium was exchanged. Cell supernatant with viruses was collected 48 h after adding the plasmid/PEI mix to the cells, then centrifuged at 500 × g, 4 min and filtered through a 0.45 µm PES filter. Filtered supernatant was aliquoted and kept at −80 °C until needed.

3.1.4. Lentiviral transduction, antibiotic selection and single cell cloning

EwS wild-type (wt) cells were seeded at 2×10^5 per T25 flasks in duplicate. The following day, 1 mL of filtered viral supernatant was added dropwise to one flask together with Polybrene Transfection Reagent (1:1000, Sigma-Aldrich). After 24 h of incubation with the virus, cells were washed with DPBS (1×) and selection medium containing 1 µg/mL Puromycin (InvivoGen, San Diego, CA, USA) was added to both flasks. After 48–72 h, cells were washed with DPBS (1×) and further grown in standard medium.

Generated cell lines were then seeded as 1 cell/well in three 96-well cell culture plates to grow single cell clones in RPMI-1640 supplemented with 30% FCS, 2% GlutaMAX™ Supplement (100×, Thermo Fisher Scientific), and 1% Gibco™ HEPES (1 M, Thermo Fisher Scientific) to enhance single-cell growth (**Figure 3.1**). After approximately 1 week, wells with single colonies were observed under the microscope and marked. When grown to 80% confluence (usually after 2–3 weeks from seeding), colonies were transferred to 48-well culture plates

using Accutase (Sigma-Aldrich) for cell detachment. After cells have grown there to 80% confluence, they were transferred to 24-well cell culture plate in triplicate. One well was designated for further expansion of the clone and other two wells were treated with or without Dox (1 µg /mL), for 72 h, after which RNA was extracted, cDNA synthesized, and knockdown of the target gene measured by qPCR.

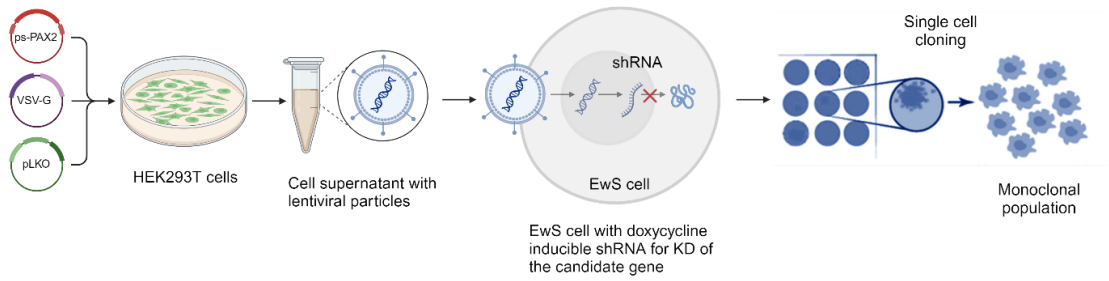

Figure 3.1 Schematic of lentiviral particle production, EwS cell transduction and single-cell cloning. Lentiviruses were produced in HRK293T cells, using three plasmids: ps-PAX2, VSV-G and Tet-pLKO-puro. Filtered cell supernatant with lentiviral particles was used to deliver genetic material into the host cell genome (Singer & Verma, 2008). The delivered DNA construct contained a shRNA expression cassette controlled by a Dox-responsive promoter. Cells that successfully received the construct were selected with puromycin and seeded as single cell clones.

3.2. Cell assays in 2D and 3D

3.2.1. Proliferation assay by trypan blue exclusion method

For proliferation assays, 1,2 × 10^5 EwS cells/well of a 6-well plate were seeded with/without Dox in triplicates for 72 h. Thereafter, cells including their supernatant were collected by trypsination and counted using standardized hemocytometers using the Trypan Blue Solution 0.4% (Life Technologies, Carlsbad, CA, USA) exclusion method to quantify the number of viable and dead cells (Funk & Musa 2020).

3.2.2. Colony forming assay (CFA)

For CFAs, 8 × 10^4 cells /well were seeded in triplicates in a 6-well plate. After 24 h, Dox (1 µg/mL) was added to induce RNA-interference mediated *LMO7* KD or *LMO7* overexpression (OE). Dox was renewed every 48 h. When performing CFAs with *LMO7* KO cell lines, parental wt EwS cell lines were used as control and standard medium was refreshed every 48 h. At the experimental endpoint (7–10 days after seeding, depending on the cell line), medium was

removed, colonies washed with DPBS (1×), and then air dried for 5 min. Colonies were fixed with 800 µL/well ice-cold methanol (100%, Sigma-Aldrich) for 10 min at −20 °C. After removing methanol colonies were left to dry until white (5–10 min) and were then stained with 800 µL/well crystal violet solution for 20 min. After washing with DPBS (1×) and drying, plates were scanned and analyzed using ImageJ software (ImageJ 1.54f, NIH, USA).

Crystal violet stock solution (50 mL) for CFA staining was prepared as follows: 10.8 mL crystal violet (2.3%, Sigma-Aldrich), 12.5 mL formalin (4%), 0.5 mL methanol (100%, Sigma-Aldrich), 26.2 mL DPBS (1×) and was stored in dark bottles, due to the crystal violet light sensitivity, at RT.

3.2.3. 3D sphere viability assays

For 3D sphere viability assays, A-673/TR/shLMO7 and MHH-ES-1/TR/shLMO7 cells were seeded in quadruplicates at a density of 1×10^3 cells/well in a 96-well U-bottom, cell-repellent surface culture plates (Greiner Bio-One, Frickenhausen, Germany) with and without Dox (1 µg/mL). Every 48 h there was a half media exchange, adding fresh medium with 2× Dox. After 5 d, representative images of spheres were taken with 5× objective on an Axio light microscope with camera (Zeiss, Jena, Germany). Subsequently, sphere viability was measured using CellTiter-Glo Luminescent Cell Viability Assay (CTG) reagent (Promega, Madison, WI, USA). For that purpose, spheres were transferred to opaque plates and incubated with CTG reagent (1:1 ratio) in the dark on a shaker for 30 min. Luminescence from the samples was recorded at 1 sec integration time using a GloMax Microplate reader (Promega). Sphere viability was calculated by subtracting the blank values and relative to control.

3.2.4. Transwell assay

A-673/TR/shLMO7 and MHH-ES-1/TR/shLMO7 cells were pretreated with/without Dox (1 µg/mL) for 72 h in standard culturing conditions. Cells were then split and kept in 1% FCS (starvation) medium for 24 h in conditions with/without Dox (1 µg/mL). Cells were then seeded at a density of 5×10^4 cells/well in 300 µL of 1% FCS media with/without Dox in Thincert cell culture insert for 24-well plates (pore size 8 µm, Greiner). The media surrounding the inserts was 10% FCS with/without Dox. The following day, cells that migrated through the membrane toward the 10% FCS-containing well were fixed in 4% formalin (5 min) and stained with crystal violet (10 min). During incubation, cells were mechanically removed from the top of the insert using cotton swab. Inserts were then washed by dipping into ddH_2O and destained using 10% acetic acid in DPBS (1×). Absorbance of the solvent was measured using a GloMax

Microplate reader (Promega) at 600 nm (**Figure 3.2**). The ratio of cells migrating toward the chemoattractant was calculated relative to control.

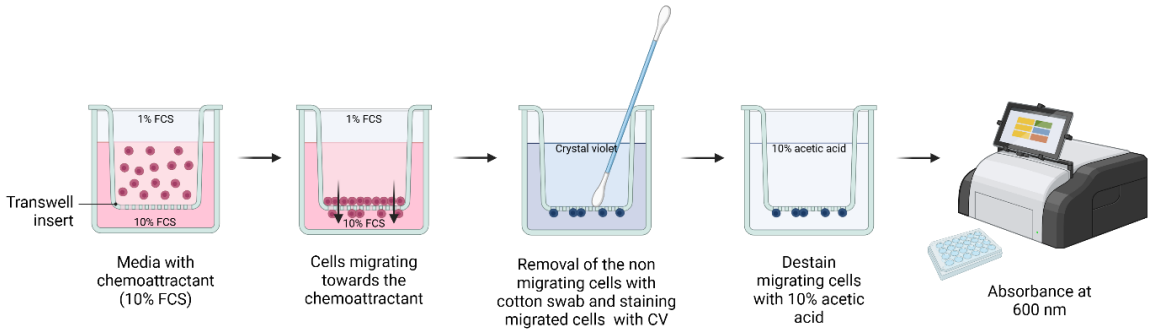

Figure 3.2. Schematic representation of transwell assay. Prior to seeding in upper chamber of transwell inserts, cells were starved in 1% FCS supplemented medium for 24 h. The lower chamber contained 10% FCS supplemented medium which acted as a chemoattractant for the starved cells. At 24 h post-seeding, cells were stained with crystal violet solution and non-migrating cells from the upper chamber were mechanically removed with the cotton swab. This enabled dissolving the crystal violet in 10% acetic acid only from cells that migrated through the porous membrane of the transwell. Absorbance of destained migrating cells of the lower chamber was measured at 600 nm.

3.3. Cloning

All *in silico* cloning and plasmid maps (representative example for each used plasmid of this thesis is shown in **Supplementary figure 7.1**) were generated in SnapGene (version 7.2.1). Software availability obtained trough the institutional licence (KITZ, Heidelberg).

3.3.1. Single-vector inducible lentiviral RNAi system for conditional LMO7 KD

In order to generate Dox-inducible *LMO7* KD cell lines, shRNA sequences were designed using the RNAi Consortium shRNA Library, an online tool from Broad Institute. Two shRNAs targeting *LMO7* were selected according to their predicted intrinsic score (>10) and coverage of CDS and/or 3'-end. Chosen sequences were ordered as sets of primers (see **Table 3.1**) and annealed in a PCR reaction with annealing buffer and lowering temperatures from 95 °C to 14 °C. To clone the shRNA into the designated plasmid, Tet-pLKO-puro (Addgene, #21915) was cut open with AgeI-HF (New England Biolabs, Ipswich, MA, USA) and EcoRI-HF (New England Biolabs) and the stuffer region was removed. The digested plasmid was electrophoresed on a 1% agarose gel and the product purified using NucleoSpin Gel and PCR Clean-up kit (Macherey-Nagel, Düren, Germany) according to the manufacturer's protocol. Digested plasmid and shRNA oligos were ligated using T4 ligase with a 2 h incubation at 16°C.

The ligated product was used to transform competent NEB® Stable Competent *E. coli* (High Efficiency) (New England Biolabs). Transformed bacteria were plated on LB Broth agar (Sigma-Aldrich) plates with 100 µg/mL ampicillin (Sigma-Aldrich) overnight. The next day, grown colonies were picked for colony PCR and confirmed with Sanger sequencing (Eurofins Genomics Europe Sequencing GmbH, Konstanz, Germany). Colonies carrying correct shRNA sequences were grown overnight in LB medium with 100 µg/mL ampicillin and plasmids were extracted in larger quantities using Midi Prep (Zymo Research, Irvine, CA, USA) according to the manufacturer's protocol. From overnight cultures, glycerol stocks were prepared for long term storage at −80 °C.

3.3.2. Cloning of fusion binding sites and luciferase reporter assays

To assess the average enhancer/repressor activity of both alleles of the LMO7-associated fusion binding sites in a given cell, two fusion binding regions in the proximity of *LMO7* gene (indicated by R2 Gene Browser as EWSR1::ETS core sites) were PCR-cloned upstream of the SV40 minimal promoter into the pGL3-Fluc vector (Promega, #E1761): 373 bp fragment (hg19 coordinates: chr13: 76,195,324–76,195,697) and 434 bp fragment (hg19 coordinates: chr13: 76,340,783–76,341,217). Primer sequences are given in **Table 3.1**. Furthermore, the distal LMO7 promoter upstream from the LMO7 gene was PCR-cloned upstream of luciferase gene into a pGL4-10 (Promega, #9PIE665) vector: 247 bp (hg19 coordinates: chr13: 76,140,731–76,140,978). For amplifying the regions of interest from A-673 cells, Invitrogen Platinum SuperFI II PCR Mix was used according to manufacturer's protocol. Amplified DNA was gel purified using Nucleospin Gel and PCR Cleanup kit (Macherey-Nagel). pGL3-Fluc vector was digested with NheI-HF and KpnI-HF and pGL4-10 with NheI-HF and HindIII-HF (all restriction enzymes were from Thermo Fisher Scientific). Digested vectors were gel purified using Nucleospin Gel and PCR Cleanup kit (Macherey-Nagel) and assembled using NEBuilder HiFi DNA Assembly Master Mix (New England Biolabs), following the manufacturer's protocol. NEB 5-alpha Competent *E. coli* (High Efficiency) (New England Biolabs) were directly transformed with 2 µL of ligation product and plated overnight in LB+Amp plates. Sequencing was performed by overnight *E. coli* run using Sanger sequencing at Microsynth AG (Balgach, Switzerland).

A-673/TR/shEWSR1::FLI1 and MHH-ES-1/TR/shEWSR1::FLI1 cells (2.5×10^4 per well in a 24-well plate) were treated with/without Dox (1 µg/mL; Sigma-Aldrich) 48 h prior to transfection. Transfection was performed using Lipofectamine™ LTX Reagent with PLUS™

Reagent (Invitrogen) and Opti-MEM (Thermo Fisher Scientific) with generated pGL3-Fluc vectors of in equal mass (212 ng) and with the Renilla pGL3-Rluc vectors (Promega) (2.12 ng) in a total volume of 55 µL, following the protocol from Hölting & Knott (2020). The medium (0.5 mL) was replaced by fresh medium with/without Dox (1 µg/mL; Sigma-Aldrich) 8 h post-transfection. After 48 h, the cells were lysed and assayed with a dual luciferase assay system Beetle-Juice Luciferase Assay Firefly (PJK GmbH, Kleinblittersdorf, Germany) and Renilla-Juice Luciferase Assay (PJK GmbH) according to manufacturer's instructions. Firefly luciferase activity was normalized to Renilla luciferase activity.

3.3.3. Cloning of conditional LMO7 overexpression system

In order to generate Dox-inducible LMO7 overexpression cell lines, GeneArt Prime Clone gene synthesis (Thermo Fisher) was utilized to synthesize the longest *LMO7* transcript variant 1, normally expressed in EwS cells. *LMO7* transcript variant 1 was excised from the gene synthesis donor plasmid and cloned into the Dox-inducible plasmid system rwSMART-TRE3G-LMO7-mCMV-TETON3G-Puro by the Cellular Tools Core Facility (DKFZ, Heidelberg).

3.4. CRISPR-Cas9 LMO7 KO

3.4.1. Electroporation optimization protocol

There was no designated program for electroporation of EwS cells using Lonza Nucleofector System (Lonza, Basel, Switzerland), so several different programs for electroporation of various cancer cells were tested using pmaxGFP™ Vector (Lonza). The Alt-R™ CRISPR-Cas9 system protocol (IDT, Coralville, IA, USA) was used for cell preparation for electroporation with pmaxGFP™ Vector and the same protocol was later also followed to introduce CRISPR-Cas9 system and LMO7 guide RNA into the EwS cells. The most optimal electroporation program on the device was chosen, DS-137, depending on the presence and strength of GFP signal in cells 48–72 h post electroporation (**Figure 3.2a**).

3.4.2. Electroporation of EwS cells with LMO7 guide RNA and Cas9 nuclease

Three EwS cell lines (A-673, MHH-ES-1,TC-32; 1×10^6 cells) were electroporated with Alt-R HiFi Cas9 Nuclease V3 (IDT, #1081061) and a two-part guide RNA (tracrRNA + crRNA): Alt-R CRISPR-Cas9 tracrRNA (IDT, #1072534) and LMO7 Alt-R® CRISPR-Cas9 crRNA

(Hs.Cas9.LMO7.1.AE, 2nM, IDT). Cells were prepared by following the Alt-R™ CRISPR-Cas9 system protocol (IDT) for delivery of ribonucleoprotein complexes into cells using Lonza Nucleofector System (Lonza) and applying the DS-137 electroporation program. After electroporation, cells were plated in RPMI-1640 medium supplemented with 20% FCS for 72 h to recover, and afterwards seeded as single cell clones (**Figure 3.3b**). Once grown, clones were Sanger sequenced at Microsynth AG (Balgach, Switzerland) in the region of *LMO7* gene (primers in the **Table 3.1**) and also confirmed for LMO7 protein presence/absence using western blot.

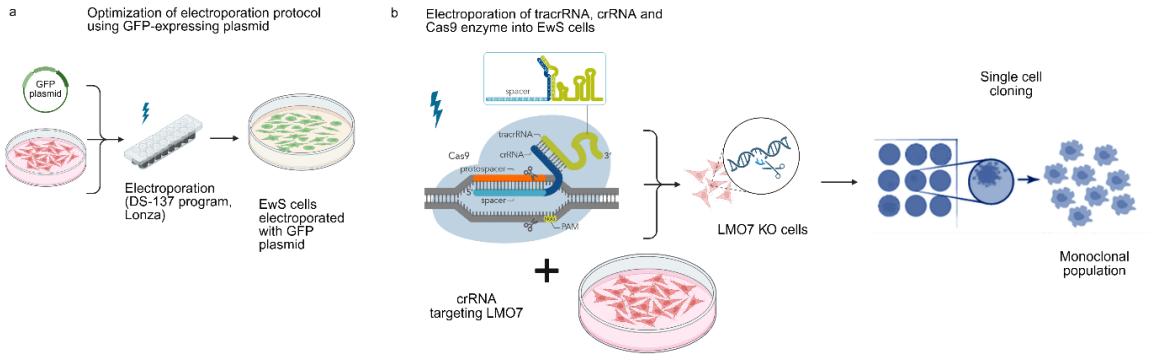

Figure 3.3. Schematic of electroporation protocol for targeted *LMO7* KO in EwS cells. a. Optimization of electroporation protocol for most efficient delivery of ribonucleoprotein complexes, using GFP expressing plasmid (pmaxGFP™ Vector, Lonza). **b.** Electroporation of Cas9 nuclease and two part guide RNA (tracrRNA + crRNA) for targeted LMO7 KO, followed by single cell cloning.

3.5. RNA analysis

3.5.1. RNA isolation

RNA was isolated from EwS cell lines using RNA purification kit NucleoSpin RNA kit (Macherey-Nagel) according to the manufacturer's protocol with the exclusion of β-ME in the initial lysate. RNA was eluted in 40 µL of RNase free water and RNA concentrations measured using Nanodrop One (Thermo Fisher).

3.5.2. cDNA synthesis

RNA was diluted to 1,000 ng for all samples. Reverse transcription was performed using the High-Capacity cDNA Reverse Transcription Kit (Applied Biosystems, Foster City, CA, USA) according to the manufacturer's protocol with the following cycling conditions: 25°C for 10 min, 37°C for 120 min, 85°C for 5 min, and hold at 4°C. The reaction volume was 20 µL.

3.5.3. RT-qPCR

RT-qPCR reactions were performed using SYBR Select Master Mix for CFX (Applied Biosystems) mixed with 1:10 diluted cDNA, 0.5 µM forward and 0.5 µM reverse primer in a total reaction volume of 20 µl. The reaction was run on CFX Opus 96 Real-Time PCR System (Bio-Rad, Feldkirchen, Germany) and analyzed using Bio-Rad CFX Manager 3.1 software. Gene expression values were calculated using the $2^{-(\Delta\Delta Ct)}$ method relative to the housekeeping gene *RPLP0* as an internal control. Oligonucleotides were purchased from Sigma-Aldrich and are listed in the **Table 3.1**. The thermal conditions for RT-qPCR were as follows: UDG Activation (50 °C, 2 min) (1 cycle), AmpliTaq® Fast DNA Polymerase, UP Activation (95 °C, 10 min) (1 cycle); denaturation (95 °C, 15 sec) and annealing/extension (60 °C, 1 min) (45 cycles); denaturation (95 °C, 30 sec).

3.5.4. Affymetrix

RNA isolated from cell lines at 55 h post-transfection with siPOOLs (siTOOLs Biotech GmbH) silencing *LMO7* or non-targeting control and QC (> 50 ng/µl RNA per sample was available and the expression of *LMO7* and housekeeping gene *RPLP0* was tested using RT-qPCR) prior to submission to Microarray Core Facility (DKFZ, Heidelberg) for Affymetrix microarray analysis. The used Affymetrix human Clariom D (Applied Biosystems) captured a total of 135,750 transcripts. Firstly, .cel files were processed using Transcriptome Analysis Console (Applied Biosystems), and output files were further processed using R studio/Bioconductor (R version 4.4.1). QC and further filtering showed 21,324 uniquely mapped transcript IDs with available Entrez IDs which excluded small, non-coding pseudogene or similar RNA transcripts. Principal Component Analysis (PCA) was applied to the transcriptomic count matrix after which principal components were subjected to Euclidean hierarchical clustering generating dendrograms representing relationships among sample groups. Differential expression analysis was performed on both pooled samples and cell line-specific groups using limma R package (3.62.2). Limma output files were ranked by differential gene expression and used as input for gene set enrichment analysis (GSEA). GSEA was performed using the clusterProfiler R package against the C2 gene set collection from MSigDB. Python (version 3.10.18, packaged by conda-forge) with Matplotlib and Seaborn libraries was used to visualize Hallmark gene set enrichment results in order to generate customized heatmap/bar plots representing enrichment scores and statistical significance.

3.6. Protein biochemistry

3.6.1. Protein isolation and Western blot

EwS cells were cultured in standard culture conditions, and harvested 72 h post-Dox treatment (1 µg/mL). Whole cellular protein was extracted using RIPA buffer (SERVA Electrophoresis GmbH, Heidelberg, Germany) and 1× protease/phosphatase inhibitor cocktail (100×, Sigma-Aldrich). Protein concentration was measured using the Pierce BCA Protein Assay Kit (Thermo Fisher Scientific) and Pierce Bovine Serum Albumin Standards (Thermo Fisher Scientific) according to manufacturer's protocol. Protein concentration was adjusted to 25 µg in 30 µL with water and Laemmli SDS sample buffer (6×, Thermo Fisher Scientific) for all samples. Proteins were separated on 10% Mini-PROTEAN® TGX™ Precast Protein Gels (10-well, BioRad) and transferred on PVDF membrane using Trans-Blot Turbo RTA Mini 0.2 µm PVDF Transfer Kit (BioRad) and the Trans-Blot Turbo Transfer System (BioRad) following the manufacturer's protocol. Membrane was blocked in 5% skim milk (SERVA Electrophoresis GmbH) in 1× TBST (ROTI®Fair TBST 7.6 tablets, Carl Roth GmbH + Co. KG, Karlsruhe, Germany). Membranes were incubated in 5% skim milk with rabbit polyclonal anti-LMO7 antibody (1:1,000, #PA5-5428, Invitrogen, Thermo Fisher Scientific), rabbit monoclonal anti-FLI1 (1:500, ab133485, abcam, Cambridge, UK) or rabbit monoclonal anti-GAPDH (1:2,000, #14C10, Cell Signaling Technology (CST), Danvers, MA, USA), overnight at 4 °C. The next day, membranes were washed three times with 1× TBST and then incubated for 1 h with mouse anti-rabbit IgG-HRP (1:5,000, #sc-2357, Santa Cruz Biotechnology, Dallas, TX, USA) in 5% skim milk at RT. After being washed for three times with 1× TBST, signal was detected using WesternBright™ Sirius™ Chemiluminescent HRP Substrate (Advansta Inc., Menlo Park, CA, USA) and visualized with imaging system Fusion FX Edge (Vilber Lourmat, Marne-la-Vallée, France) equipped with Evolution CAPT Edge software.

3.6.2. Cellular fractionation and protein separation

Nuclear, cytoplasmic, and whole-cell protein extracts were extracted from EwS cells using the Nuclear Extract Kit (#40010, Active Motif, Carlsbad, CA, USA) according to the manufacturer's protocol. Since the presence of detergents (in the Complete Lysis Buffer and in 1× Hypotonic Buffer from the used kit) may interfere with the Bradford Assay, Pierce™ Detergent Compatible Bradford Assay Kit (Thermo Fisher Scientific) was used to determine the protein concentrations. Serial dilutions of BSA (100–1,500 µg/mL) were prepared in Complete Lysis Buffer for nuclear and whole-cell extracts, or in 1× Hypotonic Buffer for

cytoplasmic protein extracts. Protein concentration was adjusted to 25 µg and used for western blotting as described above. Primary antibody overnight membrane incubations included: rabbit polyclonal anti-LMO7 antibody (1:1,000, #PA5-5428, Invitrogen), mouse monoclonal Lamin A/C (1:200, # sc-7292, Santa Cruz Biotechnology) and rabbit monoclonal anti-GAPDH (1:2,000, #14C10, CST). Secondary antibodies used were mouse anti-rabbit IgG-HRP (1:5,000, #sc-2357, Santa Cruz Biotechnology, Dallas, TX, USA) or anti-mouse IgG-HRP produced in rabbit (1:5,000, # A9044, Sigma-Aldrich) in 5% skim milk, 1 h at RT.

3.6.3. Mass spectrometry and global proteome analysis

Cells were seeded at $1{,}4 \times 10^5$ cells/well in 6-well plates in four biological replicates for global proteome analysis. The next day from seeding, cells were treated with siPOOL targeting either *LMO7* or non-targeting control. At 55 h post-transfection, cells were washed twice with cold DPBS (1×), the plates transferred to ice, and cells lysed with 100 µL 1% sodium deoxycholate-based buffer per well. Cells lysates were transferred to 1.5 mL locked Eppendorf tubes using a cell scraper and boiled at 100 °C, 10 min. Samples were then cooled on ice and stored at −80 °C until further processed by the laboratory of Dr. Ashok Kumar (DKFZ, Heidelberg) as described in Jayavelu et al., 2020.

In brief, heat-denatured and sonicated proteins were digested for 16 h with trypsin and LysC, and peptides were purified using Styroldivinylbenzol-Reversed Phase Sulfonat (SDB-RPS) stage tips, then dried and reconstituted for quantification. For mass spectrometry, 400 ng of peptides were separated on a nanoElute system (Bruker Daltonics Inc, Bremen, Germany) coupled with a TIMSTOF HT mass spectrometer (Bruker Daltonics, Bremen, Germany) operating in DDA-PASEF mode with a 120 min gradient. Data were processed using FragPipe (Version 20) with label-free quantification and match-between-runs enabled, referencing the UniProt human database with a 1% FDR threshold.

Downstream bioinformatics analyses were conducted in Perseus (version 1.6.7.0) and in R (version 4.4.2), with the support and guidance of Linghao Mao and Angelina Yershova (DKFZ, Heidelberg). In R, raw MaxLFQ intensities were imported and processed with the DEP Bioconductor package (version 1.28.0) following the workflow of Zhang et al. (2018). Protein intensities were normalized using variance-stabilizing normalization (version 3.74.0) to remove systematic bias. Missing values (assumed to be “missing-not-at-random”) were imputed by sampling from a left-shifted Gaussian distribution via DEP’s MinProb algorithm ($q = 0.01$). Differential expression between LMO7 KD and NC was carried out with the limma

package (version 3.62.2). Linear models were fitted (lmFit), empirical Bayes moderation applied (eBayes(..., robust = TRUE)), and the KD-NC contrast extracted (makeContrasts, contrasts.fit, eBayes). Data manipulation and table joins (e.g. matching gene IDs) were performed using the tidyverse backend (dbplyr v1.1.4), and gene annotations sourced from org.Hs.eg.db (version 3.20.0).

Ranked $\log_2$ fold changes were then subjected to GSEA using Hallmark gene sets obtained via MsigDB (version 25.1.1). Pathways with FDR adjusted $P< 0.05$ were considered significant, and the top 10 hallmark pathways by absolute normalized enrichment score (NES) were visualized using Python (version 3.10.18, packaged by conda-forge) with Matplotlib and Seaborn libraries in order to generate customized heatmap/bar plots representing enrichment scores and statistical significance.

3.7. *In vivo* experiments

All animal experiments were approved by the government of North Baden and conducted in accordance with the ARRIVE guidelines, the European Community (86/609/EEC), and UKCCCR (guidelines for the welfare and use of animals in cancer research).

NOD/Scid/gamma (NSG) mice have been maintained in individually ventilated cages (IVC) under specific pathogen-free (SPF) conditions with strict dark/light cycles (darkness from 8 p.m. to 6 a.m.), an ambient temperature of 20–24 °C and a humidity of 45–65%.

3.7.1. Subcutaneous EwS cell injection

Cell suspensions in DPBS (1×) of 2×10^6 EwS cells harboring a shRNA against *LMO7* (either A-673/TR/shLMO7 or MHH-ES1/TR/shLMO7 cell lines were used in two separate experiments), mixed with Geltrex™ (#A1413302, Gibco, Thermo Fisher Scientific) in 1:1 ratio. 100 µL of such suspension was injected in the right flank of 10–12-week-old NSG mice. Tumor diameters were measured every second day with a caliper and tumor volume was calculated by the formula (length × width^2) / 2. When tumors reached an average volume of ~100 mm^3, mice were randomly distributed in equal groups. The control group started receiving 5% sucrose (Sigma-Aldrich) in drinking water, while the treatment group started receiving 2 mg/mL Dox BelaDox (Bela-pharm) dissolved into drinking water with 5% sucrose (Sigma-Aldrich). Before tumors in the control group reached the volume of 15 mm in either direction, all mice were killed by cervical dislocation. Other humane endpoints were

determined as follows: ulcerated tumors, loss of ≥ 20% body weight, constant curved or crouched body posture, bloody diarrhea or rectal prolapse, abnormal breathing, severe dehydration, visible abdominal distention, obese Body Condition Scores (BCS), apathy, and self-isolation. At the termination of the experiment, xenografts were excised and smaller part snap frozen in liquid nitrogen for RNA isolation, while the rest of the tumors were fixed in 4%-formalin and paraffin-embedded for histological analyses.

3.7.2. Orthotopic EwS cell injection

All mice (n = 16) were pre-treated with 800 mg/kg/day Metamizole in drinking water as analgesia, 24 h before injection. On the injection day, mice were anesthetized with inhalable isoflurane (1.5–2.5% in volume) and their eyes were protected with Bepanthen eye cream. After disinfection of the injection site, 2×10^5 cells harboring a shRNA against LMO7 in 20 µL DPBS (1×) were directly injected with a 30 G needle (Hamilton, USA) into the right proximal tibia. Mice were subsequently treated with Metamizole in drinking water (800 mg/kg/day) for 24 h. After that, mice were randomized in equal groups and either received 5% sucrose (Sigma-Aldrich) in the drinking water (controls) or 2 mg/mL Dox BelaDox (Bela-pharm) dissolved into drinking water also containing 5% sucrose (treatment group). Primary tumor growth was followed by measuring the leg circumference every second day using a caliper, and tumor volume was calculated with the formula (length × width^2) / 2. Animals were killed at the predefined experimental endpoint, described previously. All inner organs as well as the legs were harvested, weighed, photographed, 4%-formalin-fixed, dehydrated and embedded in paraffin for histology.

3.8. Microscopy

3.8.1. IHC

Dissected mice tumors and metastasis with invaded organs were kept in 4% formalin at RT for 24–48 h. Tumors were then cut in half and fit into a cassette for paraffin embedding. Such cassettes were kept at 4 °C in 50% ethanol solution until full dehydration. Dehydration was performed by the Light Microscopy Core Facility (DKFZ, Heidelberg) by submerging the samples in series of ethanol solutions of increasing concentrations until reaching pure anhydrous ethanol. In cases of bone structures in the sample, after incubation in 4% formalin, bones were briefly washed by submerging the sample into distilled water and then decalcified

using the Decalcifying Solution-Lite (Sigma-Aldrich). Incubation in decalcified solution lasted several days on a rocking platform at 4 °C, and then dehydrated as described above. Cassettes with dehydrated samples were embedded in paraffin using HistoCore Arcadia H - Heated Paraffin Embedding Station (Leica Biosystems, Germany), left to dry and harden, then cut with the Microm HM355S Rotary Microtome (Thermo Fisher Scientific/Microm International GmbH, Walldorf, Germany) for preparation of microscopic slides. Paraffin embedding station and rotary microtome were available for use trough Light Microscopy Core Facility (DKFZ, Heidelberg) booking systems.

3.8.2. Hematoxylin and eosin (H&E) staining for formalin-fixed paraffin-embedded (FFPE) samples

Microscopy slides with FFPE tumor/organ samples were fixed in the staining rack and then transferred through the series of solutions in the fume hood: xylol twice, each 10 min; alcoholic series for watering the slides: 100% EtOH, 100% EtOH, 96% EtOH, 96% EtOH, 80% EtOH and 70% EtOH solution, keeping the staining rack with slides in each for 5 min; then washed twice with distilled water, 5 min each. Samples were then transferred to haematoxylin for 3 min, washed with tap water for 3 min, dipped in eosin for 1 min and washed with distilled water. Next, slides were transferred into a series of increasing ethanol solutions, submerged in each solution 3–5 times (70% EtOH, 80% EtOH, 90% EtOH, 100% EtOH, 100% EtOH). Then slides were incubated in xylol three times, firstly 1 min, then twice 5 min each. Slides were then embedded with Eukitt and covered with cover slips. Slides were left to dry under the fume hood for 24 h. Some of the H&E stainings for the purpose of this thesis were performed by myself and some by Sabrina Knoth and Felina Zahnow.

H&E stained sections were analyzed for the percentage of tumor necrosis over the total tumor area, as well as for mitotic and apoptotic index by counting 10 high-power fields (40×) per sample.

3.8.3. LMO7 antibody staining of FFPE samples

Staining of FFPE slides with LMO7 antibody was performed by the Light Microscopy Core Facility (DKFZ, Heidelberg) services. FFPE slides were stained overnight at 4°C with LMO7 antibody (1:200, Invitrogen) in DAKO antibody diluent (# S2022). For detection, ImmPRESS HRP Universal PLUS Polymere Kit, Peroxidase (Horse Anti- Rabbit/Mouse IgG) (#MP-7800, Vector Laboratories, Burlingame, CA, USA) was used. For all washes TBST pH 7,4 with 0.05% Tween 20 was used.

3.8.4. Immunofluorescence (IF) and confocal microscopy

Cells were seeded at 6×10^3 A-673/TR/shLMO7 (or A-673/TR/shEWSR1::FLI1) and 8×10^3 MHH-ES-1/TR/shLMO7 (or MHH-ES-1/TR/shEWSR1::FLI1) cells per chamber of a 8-well chamber microscope slide µ-Slide 8 Well (# 80826 ibidi GmbH, Gräfelfing, Germany) in 300 µL medium. Cells were treated the next day from seedin with/without Dox and incubated for 72 h. Then, medium was removed, cells washed with 200 µL DPBS (1×), then fixed with 400 µL 4% freshly prepared formaldehyde in DPBS (1×) and incubated at RT, 15 min. Cells were washed three times with 200 µL DPBS (1×), 5 min each and then permeabilized with 200 µL of 0.1% Triton X-100 (Sigma-Aldrich) in DPBS (1×), and incubated for 10 min. After that, cells were washed three times with 200 µL DPBS (1×), 5 min each and then blocked in 200 µL 1% BSA in DPBS (1×) for 1 hour at RT. After removing the blocking buffer, cells were incubated overnight at 4 °C in 200 µL primary antibody solution with rabbit polyclonal anti-LMO7 antibody (1:200, #HPA020923, Atlas Antibodies, Stockholm, Sweden) and mouse monoclonal anti-vinculin antibody (1:500, # sc-73614, Santa Cruz Biotechnology) in 1% BSA (Roth) + 0.25% Tween 20 (Sigma-Aldrich). Then, slides were washed three times with 200 µL DPBS (1×), 5 min each. And incubated with secondary antibodies: donkey anti-mouse IgG (H+L) Alexa Fluor Plus 488 (1:5000, # A32766, Invitrogen), Alexa Fluor 647 goat anti-rabbit IgG (H+L) (1:500, # A21245, Invitrogen) and Alexa Fluor 594 Phalloidin (F-Actin) (1:200, #A12381, Invitrogen) in 1% BSA/0.25% Tween 20 buffer incubated at a RT for 2 hours, in the dark. Finally, secondary antibody solution was removed and cells were washed three times with DPBS (1×), 5 min each. Slides were mounted with ProLong™ Diamond Antifade Mountant with DAPI (Thermo Fisher Scientific) and kept in the dark. Images are taken using the confocal laser scanning microscope ZEISS LSM 710 ConfoCor 3 (Carl Zeiss AG, Jena, Germany) available trough Light Microscopy Core Facility (DKFZ, Heidelberg) booking systems. All images of biological replicates were taken at the same laser intensities, and all images were processed at the same brightness and contrast range so that can be comparable. Images were processed and analyzed using Fiji, an open-source distribution of ImageJ software (ImageJ 1.54f) (Schindelin et al., 2012).

3.9. Spatial transcriptomics

3.9.1. 10x Visium CytAssist spatial gene expression platform

10x Visium CytAssist spatial gene expression on FFPE sample and raw data pre-processing was done in collaboration with the laboratory of Prof. Dr. Moritz Gerstung and PhD student Heng Luo.

A 10 µm sample section was cut from a EwS FFPE sample (KITZ-SARC-0191) using Microm HM 355S (kindly provided by Stephanie Kutchman) and placed on a SuperFrost slide. The sample was dried overnight in a desiccator to eliminate residual moisture after which it was stained with H&E and destained following protocol CG000520 Rev C from 10x Genomics. After decrosslinking, the sample was processed using the 10x Genomics FFPE Spatial Gene Expression 6.5 mm Human Transcriptome Kit (Catalog No. 1000443) following the manufacturer's protocol (CG000495 Rev F) with the Visium CytAssist platform.

The final Visium sequencing library was sequenced on the NovaSeq™ X Series platform using the 1.5B Reagent Kit (100 Cycles) following the manufacturer's protocol. The raw sequencing output was first converted into FASTQ files using the 'mkfastq' function in Space Ranger (version 3.0.0, 10x Genomics). The aligned FASTQ files were subsequently processed using the 'count' function in Space Ranger (version 3.0.0, 10x Genomics) to generate the gene expression count matrix, using the GRCh38-2020-A reference genome and the Visium Human Transcriptome Probe Set v2.0 (GRCh38-2020-A). The spatial transcriptomics count data was manually aligned with CytAssist image using the Loupe Browser.

3.9.2. Downstream data analysis and visualization

Spatial transcriptomic data was analyzed using the scanpy workflow (Wolf et al., 2018). Input data contained 4,503 observations (spatial location on the tissue) and 18,085 gene variables, n_obs × n_vars = 4503 × 18085. Quality control steps included the filtering of spatial features based on min and max count (min_counts = 1,000, max counts = 35,000) as well as filtering out those with >20% mitochondrial genes. Those steps yielded 4,362 spatial locations for downstream analysis. Genes that were detected in less than 10 cells were also filtered out (n = 84). After normalization and logarithmic transformation of the data, 5,000 highly variable genes were selected using scanpy.pp.highly_variable_genes() function with 'seurat' flavor. Dimensionality reduction was performed to summarize the data with 50 principal components,

followed by the construction of a neighborhood graph to model local similarities. Clustering was conducted using the Leiden algorithm (with resolution = 1), and results were visualized in both UMAP and spatial coordinates overlaid on tissue images to preserve anatomical context.

Data from analyzed tumor marker expression, high transcriptional activity and H&E staining was used to define the border of tumor and tumor-adjacent tissue in the sample. Then within defined tumorous tissue, spatial expression of genes of interest was correlated to the expression of genes know to be targets downregulated (EWSR1::ETS_low) or upregulated (EWSR1::ETS_high) by the EWSR1:.ETS fusion, available from Orth et al. (2022). Fusion activity signature was then overlaid on the tissue according to the spatial coordinates of the analyzed sample. The analysis was run in Python version 3.10.18 (packaged by conda-forge).

3.9.3. Pathway analysis in spatial transcriptomics

The computing tool decoupler-py with pathway gene sets from PROGENy (Badia-i-Mompel et al., 2022; Dimitrov et al., 2024; Schubert et al., 2018) was used to visualize pathway activity spatial expression in the patient sample that was transcriptionally profiled using 10x Visium CytAssist. The analysis was run in Python version 3.10.18 (packaged by conda-forge).

3.10. Statistics and data analysis

3.10.1. General statistics

Statistical data analysis was performed using GraphPad Prism 9 (GraphPad Software Inc., CA, USA), if not otherwise specified. Comparison of two groups was carried out using a two-sided Mann-Whitney test and *P*-values were estimated from two-sided statistical tests, if not otherwise specified. For data presented as box-dot plots, the horizontal bars represent the mean and whiskers the SD. The sample size for all *in vitro* experiments was chosen empirically. For *in vivo* experiments, the sample size was predetermined using power calculations with $\beta = 0.8$ and $\alpha < 0.05$ based on preliminary data and in compliance with the 3R system (replacement, reduction, refinement).

3.10.2. 196 EwS patient cohort analysis

Kaplan-Meier survival analyses were performed on 196 EwS primary tumor samples that had been molecularly confirmed and retrospectively collected, as well profiled at the mRNA level by gene expression microarrays in previous studies (Postel-Vinay et al., 2012; Savola et al.,

2011; Scotlandi et al., 2009; Volchenboum et al., 2015). Microarray data was generated using Affymetrix HG-U133Plus2.0, Affymetrix HuEx-1.0-st or Amersham/GE Healthcare CodeLink microarrays and is associated with following Gene Expression Omnibus (GEO) accession codes: GSE34620 (Postel-Vinay et al., 2012), GSE17618 (Savola et al., 2011), GSE12102 (Scotlandi et al., 2009), GSE63157 (Volchenboum et al., 2015), provided with clinical annotations data was normalized separately as previously described (Baldauf et al., 2017). Genes represented on all microarray platforms were kept for further analysis. Batch effects were removed using the ComBat algorithm (Stein et al., 2015) and data processing was done in R. For Kaplan-Meier analyses of overall survival from 196 EwS patient cohort, statistical differences between the groups were assessed by a Mantel-Cox test. A custom code tool named GenEx developed by the former lab mameber Dr. Julia S. Gerke was used for optimal cut-off selection, which tested all possible cut-offs between the 20^{th} and 80^{th} expression percentiles for the largest difference in area under the curves in the Kaplan-Meier analyses (Sannino et al., 2019). Kaplan-Meier analyses testing dose dependency curve of *LMO7* expression were done using tertiles as cut-offs.

In a cohort of 196 EwS patients, patients were stratified into two groups based on median *LMO7* expression levels. The association between *LMO7* expression and disease stage (localized and metastatic) was assessed by chi-square test using the chi2_contingency function from the SciPy Python library (scipy.stats) in Python version 3.10.18 (packaged by conda-forge).

Gene expression data from 196 samples (13,253 genes) was analyzed using single-sample gene set enrichment analysis (ssGSEA) with the GSVA and GSEABase R packages to quantify pathway activity per sample. Survival analysis was then performed by splitting samples into high and low pathway activity groups based on the median enrichment score, followed by Kaplan-Meier curve estimation and log-rank testing to assess survival differences. Multiple testing correction using the Bonferroni method was applied to control false positives across 3,484 pathways, resulting in 12 statistically significant pathways (only fusion activity pathway was shown as part of this thesis FERREIRA_EWINGS_SARCOMA_UNSTABLE_VS_STABLE_DN, from MsigDB). RStudio (R 4.4.0) was used for the purpose of this analysis. This analysis was performed for the purpose of laboratory rotation project from David Wolfhardt.

Additionally, to identify pathways significantly associated with *LMO7* gene expression profile in 196 EwS patient cohort, GSEA was performed in R (version 4.3.0) using the C5 ontology gene sets from MSigDB. As input file ranked correlations between *LMO7* expression and all other genes in the patient cohort were used. Weighted gene co-expression network analysis (WGCNA) was utilized to detect gene modules and assess their associations with phenotypic traits. Resulting network visualizations were generated using Cytoscape (version 3.10.0).

3.10.3. Integrated transcriptomic and proteomic analysis

To identify concordantly expressed genes/proteins, only those expressed at both the mRNA and protein level were retained (n = 6,438). Expression distributions were examined via histograms and density plots, with Pearson's correlation quantifying transcriptomic-proteomic $\log_2$ FC relationships (r = 0.594, $P < 0.0001$). A quadrant-based classification system categorized genes and proteins based on expression patterns using platform-specific thresholds ($|\log_2 FC| > 1$ for genes, $|\log_2 FC| > 0.5$ for proteins, adjusted $P < 0.05$ for both. Data processing and filtering was handled with dplyr function for identifying the variables to plot.

To identify consistently enriched biological processes, fGSEA as performed independently on both datasets using the C2 CGP collection from MSigDB. Normalized enrichment scores (NES) were integrated using quadrant-based classification to identify common pathways, visualized with scatter plots highlighting concordant pathways, defined as $|NES| > 1.5$ and a less stringent cut-off of adjusted $P < 0.5$, without which little to no results were possible from the differentially expressed proteins. All analyses were performed using RStudio (R 4.4.1).

3.10.4. RNA-seq analysis of cells treated with p300/CBP inhibitor

In order to assess the impact of p300 and CREB binding lysine acetyltransferase (p300/CBP) inhibitor (iP300w) on *LMO7* expression in three EwS cell lines (A-673, TC-71, SK-ES-1) treated with/without iP300w (1 µM, for 4 h), FASTQ files and sample sheet from RNA-seq were obtained from Wei et al. (2024) (SRA: PRJNA1161150). Data was analyzed using Nf-core/rnaseq pipeline (version 3.19.0), using star_salmon aligner on GRCh38 reference genome. DESeq2 was used as part of the differential expression analysis downstream of the nf-core/rnaseq pipeline. Differential gene expression across three cell lines in conditions with/without treatment was shown as boxplots and *P*-value was calculated using a two-tailed t-test. The analysis was run in the R version 4.4.3.

3.10.5. Methylation

INFORM EwS patient cohort (n=106) was methylation profiled using array Infinium Methylation EPIC v2.0 Kit (Illumina) and RNA sequenced as part of the INFORM project (KITZ, Heidelberg). Processed data (by Anna Ehlers, DKFZ, Heidelberg) was used for downstream analysis in the locus of *LMO7* gene. Beta values of CpG islands associated with the *LMO7* gene were mapped to their genomic coordinates using the R package minfi (version 1.48.0). These beta values were subsequently correlated with *LMO7* gene expression levels in the same patient cohort using Pearson's correlation coefficient. All analyses were conducted using R version 4.3.0.

3.10.6. ChIP-seq and HiChIP data data visualization - R2, IGV and Juicebox

EWSR1::ETS binding peaks from ChIP-seq data generated as part of the ESCLA project (Orth et al., 2022, GEO: GSE176339) was visualized in the region of *LMO7* using the R2: Genomics Analysis and Visualization Platform (https://hgserver1.amc.nl/cgi-bin/r2/main.cgi). For the purpose of visualization and analysis of published ChIP-Seq, Cut&Run, and FAIRE data from three different EwS cell lines (EW502 from Patel et al. (2012), GSE31838; A-673 and SK-N-MC from Riggi et al. (2014), GSE61953) with a focus on the *LMO7* genomic region, with markers of EWSR1::ETS binding, IGV software was used (version 2.2.8). Same software was used for visualization of histone mark H3K27ac localization and presence under conditions with/without *EWSR1::FLI1* KD in the proximity of *LMO7* transcription start site (TSS) in TC-32 cell line using the dataset from Ebegboni et al. (2024) (GSE243184).

HiChIP dataset used in this thesis was obtained from Prof. Didier Surdez (ETH Zurich), and is published in Surdez et al. (2021), GEO: GSE133228. For data visualization in the region of *LMO7* gene in A-673 cell line, Juicebox software was used (Rao et al., 2014).

3.10.7. Schematics

All schematic representations from the thesis (e.g. method representations, pathways visualizations and similar) were generated in BioRender trough the institutional licence (KITZ, Heidelberg).

3.11. Human samples and ethics approval

All procedures involving human participants and human-derived materials were performed in accordance with the principles of the Declaration of Helsinki. Data generated through the INFORM registry (German Clinical Trial Register, number DRKS00007623; van Tilburg et al., 2021) was made available after internal IRB approval. The analysis of patient material and molecular data has been approved by the ethics committee of the University Hospital Heidelberg (approval ID: S-211/2021). Written informed consent was obtained from all participants (or their legal guardians, where applicable) prior to inclusion in the study. Patient confidentiality and data protection were strictly maintained in compliance with institutional policies and applicable data protection regulations.

Table 3.1. List of primers. All primers oriented in 5' to the 3' direction.

Primer name	Fw primer sequence	Rev primer sequence	Application	NCBI gene ID
shLMO7 490	CCGGCCTGGGTCTTTGTTATCATTTCTCGAGAAATGATAACAAAGACCCAGGTTTTTG	AATTCAAAAACCTGGGTCTTTGTTATCATTTCTCGAGAAATGATAACAAAGACCCAGG	cloning	
shLMO7 491	CCGGGCGTCATTAAGAAGATCAATACTCGAGTATTGATCTTCTTAATGACGCTTTTTG	AATTCAAAAAGCGTCATTAAGAAGATCAATACTCGAGTATTGATCTTCTTAATGACGC	cloning	
shLMO7 492	CCGGGCTATTAACAACACCAAGTTTCTCGAGAAACTTGGTGTTGTTAATAGCTTTTTG	AATTCAAAAAGCTATTAACAACACCAAGTTTCTCGAGAAACTTGGTGTTGTTAATAGC	cloning	
LMO7	TGTTGCCTGTGAGTGTGAC	ACAGTGCTTTCGTATGGAGG	qPCR	4008
RPLP0	GAAACTCTGCATTCTCGCTTC	GGTGTAATCCGTCTCCACAG	qPCR	6175
Hs.Cas9. LMO7.1.AE	/AltR1/ rArCrArGrUrGrGrCrUrArCrGrGrUrGrArCrArUrCrGrUrUrUrUr ArGrArGrCrUrArUrGrCrU /AltR2/		CRISPR-Cas9 crRNA	
LMO7 KO	CAGTTGTGGGCAAACAATTAA	TAAGCCTGAATCTGGAGAGAGA	sequencing colony PCR	
EWSR1-FLI1	GCCAAGCTCCAAGTCAATATGC	GAGGCCAGAATTCATGTTATTGC	qPCR	
1st ChIP peak LMO7	GGCACTTACTCTGAGTTGTCTT	GAACTTATTTGCACTTGCCCTATC	cloning	
1st ChIP peak LMO7 overhangs	ATTTCTCTATCGATAGGTACGGCACTTACTCTGAGTTG	TCGCAGATCTCGAGCCCGGGGAACTTATTTGCACTTGC	cloning	
2nd ChIP peak LMO7	CTGGAAATATAGAGATGTGCAGTCA	ACATAGTCCAAAGCTCCCATTT	cloning	
2nd ChIP peak LMO7 overhangs	ATTTCTCTATCGATAGGTACCTGGAAATATAGAGATGTGC	TCGCAGATCTCGAGCCCGGGACATAGTCCAAAGCTCCC	cloning	
LMO7 distal promoter	CCTTCACTGGCTACTGCTATTC	TCATCAAGGAAGCAGGGAATG	cloning	
LMO7 distal promoter overhangs	CTGGCCGGTACCTGAGCTCGCCTTCACTGGCTACTGCTATTC	CCAACAGTACCGGATTGCCATCATCAAGGAAGCAGGGAATG	cloning	
RV3	CTAGCAAAATAGGCTGTCC		sequencing	
pLKO	GGCAGGGATATTCACCATTATCGTTTCAGA	GACGTGAAGAATGTGCGAGA	sequencing	
circLMO7	ACAGATTGGATTGAAAGAAGCCC	CACACAGCAGAACACCATTTTC	qPCR	
OE_LMO7	CCTGGGTCTTTGTTATCATTTGC	AGTCGTTGCAGTACAGTTGG	qPCR	4008

Table 3.2. List of antibodies.

Type	Target	Catalogue number	Brand	Application	Dilution
1°Ab	Anti-LMO7 (rabbit, polyclonal)	HPA020923	Atlas antibodies	IF, IHC	1:200
1°Ab	LMO7 (rabbit, polyclonal)	PA5-54281	Invitrogen	WB IHC	1:1,000 1:200
1°Ab	Anti-FLI1 (EPR4646) (rabbit, monoclonal)	ab133485	abcam	WB	1:500
1°Ab	Anti β-actin (ACTB) (AC-15) (mouse, monoclonal)	A5441	Sigma-Aldrich	WB	1:5,000
1°Ab	Anti-GAPDH (14C10) (rabbit, monoclonal)	#2118	CST	WB	1:2,000
1°Ab	Lamin A/C (363) (mouse, monoclonal)	sc-7292	Santa Cruz	WB	1:200
1°Ab	Anti-vinculin (7F9) (mouse, monoclonal)	sc-73614	Santa Cruz	IF	1:500
2°Ab	Mouse anti-rabbit IgG-HRP	sc-2357	Santa Cruz	WB	1:2,000
2°Ab	Anti-Mouse IgG-HRP produced in rabbit	A9044	Sigma-Aldrich	WB	1:2,000
2°Ab	Alexa Fluor 594 Phalloidin (F-Actin)	A12381	Invitrogen	IF	1:200
2°Ab	Alexa Fluor 647 goat anti-rabbit IgG (H+L)	A21245	Invitrogen	IF	1:500
2°Ab	Donkey anti-mouse IgG (H+L) Alexa Fluor Plus 488	A32766	Invitrogen	IF	1:5,000

4. RESULTS

4.1. Multi-omics dataset integration for identification of metastasis-relevant genes in EwS

Accumulating evidence suggests that EwS cells can reside in a metastable state with oscillating *FET::ETS* expression levels (Franzetti et al., 2017; Sannino et al., 2017). However, the exact mechanism of how low levels of EWSR1::ETS promote a more metastatic phenotype remained elusive. Therefore, an integrative approach to deepen the understanding of metastatic processes in EwS with clinical relevance was designed, generating a pipeline consisting of several bioinformatics and statistic filtering steps. Firstly, it was important to identify clinically relevant downstream mediators of *FET::ETS*-low phenotype that are strongly upregulated upon reduced activity of the fusion. For that purpose, a bioinformatics pipeline consisting of two bulk transcriptome datasets and one spatial transcriptome of EwS patient sample was utilized (**Figure 4.1a**). The first transcriptomics dataset comprised of five representative EwS cell lines (A-673, MHH-ES-1, SK-N-MC, TC-71 with *EWSR1::FLI1* fusions; and TC-106 with an *EWSR1::ERG* fusion) that were previously genetically modified to enable an shRNA-mediated KD of the respective fusion and transcriptome profiled within ESCLA (Orth et al., 2022, GEO: GSE176339). The second transcriptome dataset consisted of the clinically annotated set of 196 EwS patient tumors for which information on patient overall survival was also available from Baldauf et al. (2017) as well as profiled at the mRNA level by gene expression microarrays in previous studies (Postel-Vinay et al., 2012; Savola et al., 2011; Scotlandi et al., 2009; Volchenboum et al., 2015). Integration of the ESCLA dataset and 196 EwS patient transcriptomic cohort revealed 13 genes that were both strongly upregulated ($\log_2$ FC > 2.5) upon *FET::ETS* silencing and significantly associated with patient outcome (cut-off for each gene at the best percentile; log-rank $P < 0.05$, full list provided in Supplementary Table 1). Of those 13 genes, further filtering that focused only on those that had high expression associated with worse patient outcome resulted in six genes, namely: bone morphogenetic protein 1 (*BMP1*), cysteine-rich angiogenic inducer 61 (*CYR61*), *LMO7*, lysyl oxidase (*LOX*), nidogen 2 (*NID2*) and peptidase inhibitor 15 (*PI15*) (**Figure 4.1b**).

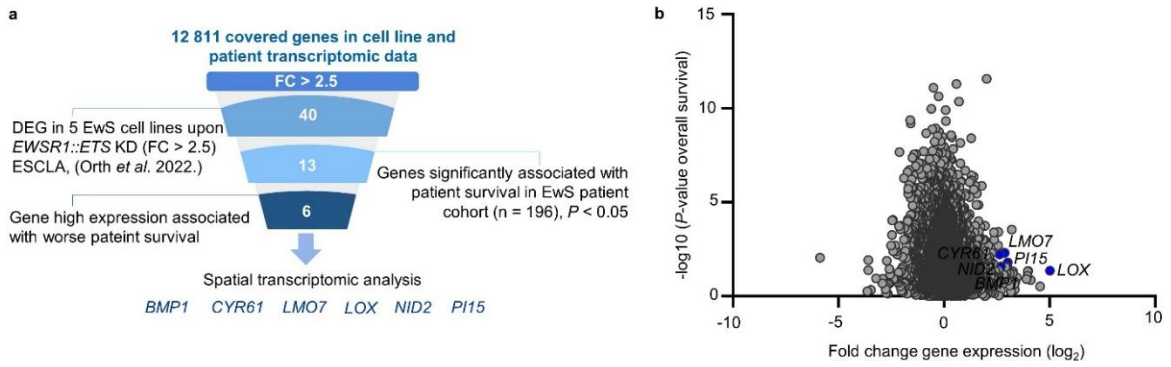

Figure 4.1 Integrative multi-omics approach identified genes with clinical relevance for invasion and metastasis in EwS. a. Workflow depicting an integrative filtering approach to identify DEGs highly expressed (FC > 2.5) in cell lines with *EWSR1::ETS* KD (ESCLA, Orth et al., 2022), genes significantly associated with worse patient outcome (196 EwS patient cohort) and highly expressed at the invasive front in spatial transcriptome profiled EwS patient sample. Numbers represent remaining gene candidates after each filtering step **b.** Plot representing fold change (log_2) gene expression of all candidates enriched in *EWSR1::ETS* KD cell lines (A-673, MHH-ES-1, SK-N-MC, TC-71 and TC-106) within ESCLA dataset and their respective *P*-values from gene expression associated with survival in EwS 196 patient cohort. Highlighted in blue, are six gene candidates (*BMP1*, *CYR61*, *LMO7*, *LOX*, *NID2* and *PI15*) with high expression in low-fusion cell ESCLA lines (FC > 2.5) that are also significantly associated with worse overall patient survival ($P < 0.05$).

The dissemination of tumor cells from primary tumors and the establishment of secondary tumor colonies in distant tissues is a complex, multi-step process known as the invasion-metastasis cascade (Lambert et al., 2017). This process is equipped with changes in genetic and molecular programs driving invasion at the primary site, which are fundamentally intertwined with those enabling metastatic dissemination (Fares et al., 2020). As EMT/MET is less clear in sarcomas than in carcinomas, primarily due to the fundamental differences in their cellular origins and EMT/MET marker expression patterns plasticity in sarcomas (Damerell et al., 2021), I hypothesized that genes involved in local tumor invasiveness will also be involved in metastatic spread. In order to further narrow down the candidates' gene list, having only those involved in both local invasiveness and metastatic spread, spatial transcriptomics analysis from the primary EwS tumor with *EWSR1::FLI1* fusion was performed using 10x Genomics Visium CytAssist Spatial Gene Expression platform within the collaboration with Division of AI in Oncology (Prof. Dr. Moritz Gerstung, DKFZ Heidelberg). The sample for this analysis was a localized EwS tumor in the gluteus of lower extremity from a 28 year old female patient, with tumor purity of 90%. FFPE tumor sample was H&E stained, and brightfield images were captured for subsequent spatial transcriptomics sequencing (**Figure 4.2a**). The spatial transcriptomics count data was manually aligned with CytAssist image using the Loupe

Browser 6 (previously performed in collaboration with the laboratory of Prof. Dr. Moritz Gerstung, DKFZ). After initial quality control and preprocessing of the data, manifold embedding and clustering based on transcriptional similarity enabled analysis and visualization of complex data as both UMAP and spatial coordinates overlaid on tissue images to preserve anatomical context by following the scanpy workflow (Wolf et al., 2018). Clustering resulted in a two-dimensional map displaying nine clusters across the sample. Each cluster was generated according to its top 10 marker genes (**Figure 4.2b**). Among these, one could observe clusters truthfully outlining anatomical and clinical features from the sample. For example, Cluster 6 had desmin (*DES*) and titin (*TTN*) as highly expressed cluster marker genes, and was spatially localized over tumor-adjacent muscle tissue. Similarly, among Cluster 3 marker genes were vascular endothelial growth factor A (*VEGFA*) and RNA binding motif protein 11 (*RBM11*) which were both previously described in EwS and upregulated by EWSR1::FLI1 (Annalora et al., 2018; Nagano et al., 2011). Their spatial expression was localized within the tumor tissue (**Figure 4.2c -** top left, first quadrant). In summary, distinct spatial variances were observed between clusters that recapitulated the anatomical and biological context.

Equivalently interesting was to observe spatial expression for each of the candidates within the anatomical context of the tumor and its adjacent tissue. To define tumor area and tumor-adjacent tissue in the sample, the data from tumor marker expression, transcriptional activity, and H&E staining altogether was analyzed and overlaid on the tissue (**Figure 4.2c -** top left, second quadrant). Of the six candidate genes, only *CYR61* was not covered in the panel, whereas the remaining could be readily detected. There was a common trend observable in the spatial expression of the candidates, whereas the majority of them showed higher expression at the tumor border and in the tumor-adjacent tissue (**Figure 4.2c**). This trend prompted me to investigate the spatial localization and correlation of each candidate gene expression with EWSR1::FLI1 activity signature in the sample. Using the established FET::ETS transcriptome signature from Orth et al., (2022), I inferred FET::ETS activity from the genes up- (EWSR1::ETS_high) or down-regulated (EWSR1::ETS_low) by the fusion in the sample (**Figure 4.2c -** bottom right two quadrants). Furthermore, the spatial expression of the remaining candidates was correlated to the inferred EWSR1::ETS-high and EWSR1::ETS-low activity within previously defined tumor borders (**Supplementary Table 7.2**). Strikingly, of those five genes, *LMO7* exhibited the highest negative correlation ($r = -0.53$, $P < 0.0001$) to EWSR1::ETS-high activity, and also the highest positive correlation ($r = 0.38$, $P < 0.0001$) to EWSR1::ETS-low activity signature. In sum, *LMO7* had a very prominent overexpression

at the invasive front as compared to the tumor center and its expression was negatively correlated with high EWSR1::ETS activity (**Figure 4.2d**).

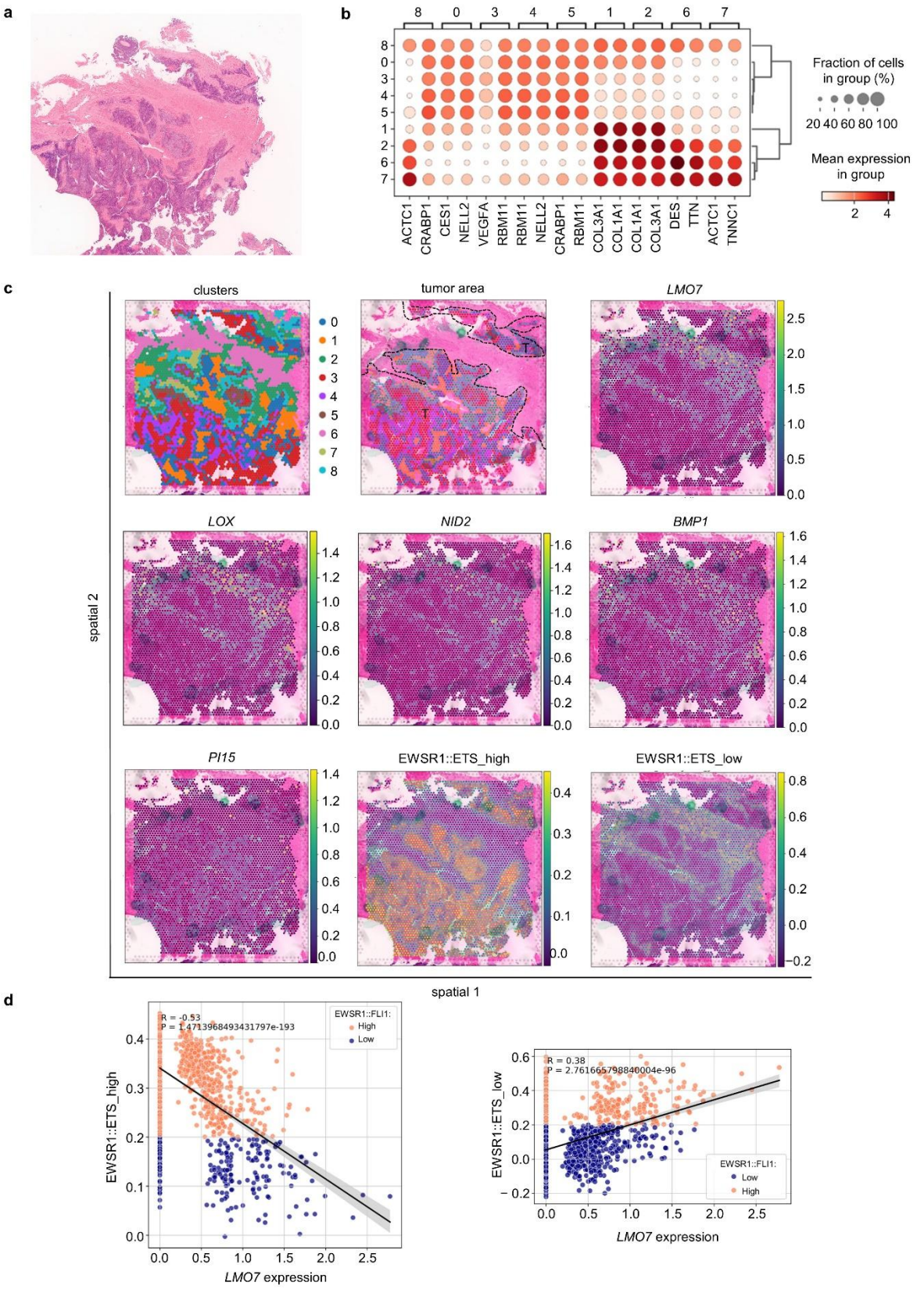

Figure 4.2 Spatial transcriptomics of patient EwS sample revealed high expression of *LMO7* at the invasive front. a. H&E staining of the sample prior to spatial sequencing. **b.** Clustering according to top 10 marker genes. Size of the circle represents number of cells in each group, while the gradient of white-to-red color represents mean expression within the group, with darker red being higher expressed. **c.** Spatial localization of clusters (top left quadrant). Spatial definition of the tumor area using transcriptional activity (median division of counts) with minor adjustments according to the H&E staining and tumor markers. The tumor area was marked with letter T, and its borders with black dashed line (second quadrant). Spatial expression of the five gene candidates that passed previous filtering steps (*LMO7*, *LOX*, *NID2*, *BMP1* and *PI15*). Inferred EWSR1::ETS activity signature from Orth et al. (2022), according to the genes upregulated (EWSR1::ETS_high) or downregulated (EWSR1::ETS_low) by EWSR1::ETS (lowest two right quadrants). Green dots visible on all images are remainings from the writing marker used for selecting the area in processing steps. **d.** Correlation of *LMO7* expression and EWSR1::ETS-high activity within defined tumor borders between (left graph, $r = -0.53$, $P < 0.0001$), and EWSR1::ETS-low activity (right graph, $r = 0.38$, $P < 0.0001$). In orange, cells with EWSR1::ETS-high and in blue cells with EWSR1::ETS-low activity signature.

To determine the association of *LMO7* expression with patient overall survival, the 196 EwS patient cohort was analyzed, firstly stratifying patients according to the best percentile (optimal cut-off) of *LMO7* expression. As shown in **Figure 4.3a**, high *LMO7* expression had a significant association with worse overall survival for EwS patients (Mantel-Cox test, $P = 0.005$). Similar observations were made when stratifying the same patient cohort in tertiles. Here, *LMO7* expression showed a dose-dependency in relation to patient outcome (Mantel-Cox test of low, medium and high *LMO7* expression in EwS patient tumors, $P = 0.0472$) (**Figure 4.3b**). Interestingly, when EWSR1::ETS fusion signature was inferred to the transcriptome data of the 196 EwS patient cohort, low fusion pathway activity group was also significantly associated (Mantel-Cox test, $P = 0.0006$) with worse patient outcome (**Figure 4.3c**). And finally, when 196 EwS patient cohort was ranked according to *LMO7* expression, dichotomized at median expression and then additionally filtered according to clinical data for only primary EwS cases with localized disease, and metastatic cases with observed metastases at diagnosis, Chi-squared test showed a significant association ($P = 0.038$) of *LMO7*-high expression with the presence of metastatic disease at diagnosis (**Figure 4.3d**). Similar observations were made in an available single cell transcriptomic dataset derived from a paired set of EwS cell lines being from the patient primary tumor (CHLA-25) and a metastatic lesion (TTC-466) (unpublished dataset, generated in frame o MD thesis of our lab member Tobias Faehling). Here, *LMO7* was significantly higher expressed ($P = 0.0013$) in the cell line derived from a metastasis (**Figure 4.3e**) as compared to the cell line derived from a primary tumor. In sum, these results indicate that *LMO7* is a novel prognostically relevant gene in EwS, being highly overexpressed at the invasive front of EwS tumors, as well as in patient metastases.

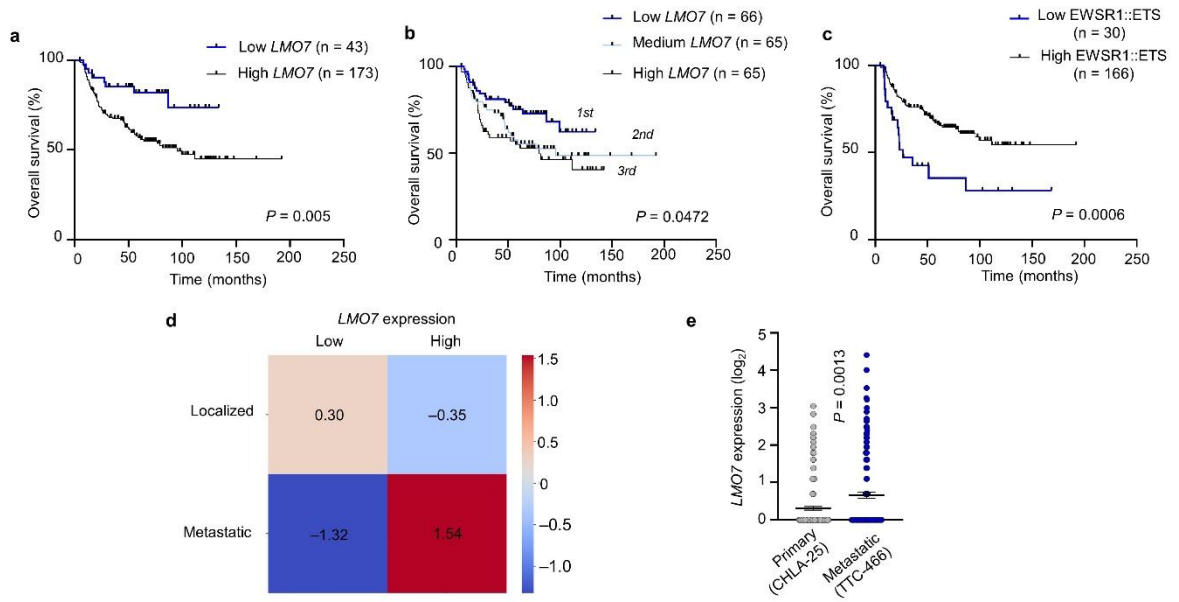

Figure 4.3 *LMO7* expression and fusion activity are associated with patient survival and development of the disease. a. Association of *LMO7* expression with patient overall survival in EwS patient cohort (n = 196). Mantel-Cox test, $P = 0.005$. **b.** Dose-dependency of *LMO7* expression levels in association with patient overall survival in EwS patient cohort (n = 196), when divided in tertiles. Mantel-Cox test of all 3 curves, $P = 0.0472$, and of high and low *LMO7* expression curves $P = 0.0161$. **c.** Association of inferred EWSR1::FLI1 signature (collection used from MSigDB was C2 CGP: FERREIRA_EWINGS_SARCOMA_UNSTABLE_VS_STABLE_DN) with patient overall survival in EwS patient cohort (n = 196). Mantel-Cox test, $P = 0.0006$. **d.** Chi-square statistic on the EwS patient cohort (n = 125, patients from 196 EwS cohort with exclusively localized or metastatic disease at diagnosis, excluding all cases with local relapse or missing clinical annotation). Chosen group was dichotomized by median *LMO7* expression (low, high). Chi-square statistic is the sum of the squares of the Pearson's residuals for all cells in the residual heatmap (Chi-square statistic = 4.32, degrees of freedom for 2×2 table df =1, and $P = 0.038$). **e.** Single cell RNA-sequencing (internal dataset, not published) of matched primary CHLA-25 and metastatic TTC-466 EwS cell lines, focused on differential *LMO7* expression, normalized and $\log_2$ transformed. Two-sided Mann-Whitney test: $P = 0.0013$.

4.2. Oscillations in FET::ETS fusion expression have an impact on LMO7 expression

To further investigate the possible EWSR1::FLI1 regulation of LMO7, a published single-cell RNA-sequencing dataset from A-673 cells with a doxycycline (Dox)-inducible shRNA against *EWSR1::FLI1* (Aynaud et al., 2020, GEO: GSE130025) was re-analyzed with special attention to *LMO7* expression. This dataset demonstrated a strong upregulation of *LMO7* upon *EWSR1::FLI1* silencing and, conversely, strong downregulation of *LMO7* upon Dox-washout and *EWSR1::FLI1* recovery. As well, there was noticeable high expression of *LMO7* in MSCs, the putative cells of origin of EwS, which do not harbor a FET::ETS fusion, while in comparison, there was little to no *LMO7* expression in three EwS patient derived xenografts (PDX) expressing the fusion (**Figure 4.4a**). Similar observations have been made from the bulk RNA expression data, when using three different EwS cell lines (A-673, MHH-ES-1 and SK-N-MC) with Dox-inducible KD of the *EWSR1::FLI* in short-term experiments of 72 h Dox treatment. Here also, *LMO7* expression was significantly upregulated upon *EWSR1::FLI1* KD (**Figure 4.4b**). Additionally, at the protein level there was an increase of LMO7 signal upon EWSR1::FLI1 KD in A-673/TR/shEWSR1::FLI1 cells upon 72 h Dox treatment (**Figure 4.4c**). In longer washout experiments, where cells were treated for 7 days with Dox and then EWSR1::FLI1 re-expression was followed until day 21 on the protein level, LMO7 protein was repressed in EwS cells expressing the fusion but upregulated upon EWSR1::FLI1 KD. After Dox washout and stabilization of EWSR1::FLI1 in the EwS cells, levels of *LMO7* diminished again (**Figure 4.4d**).

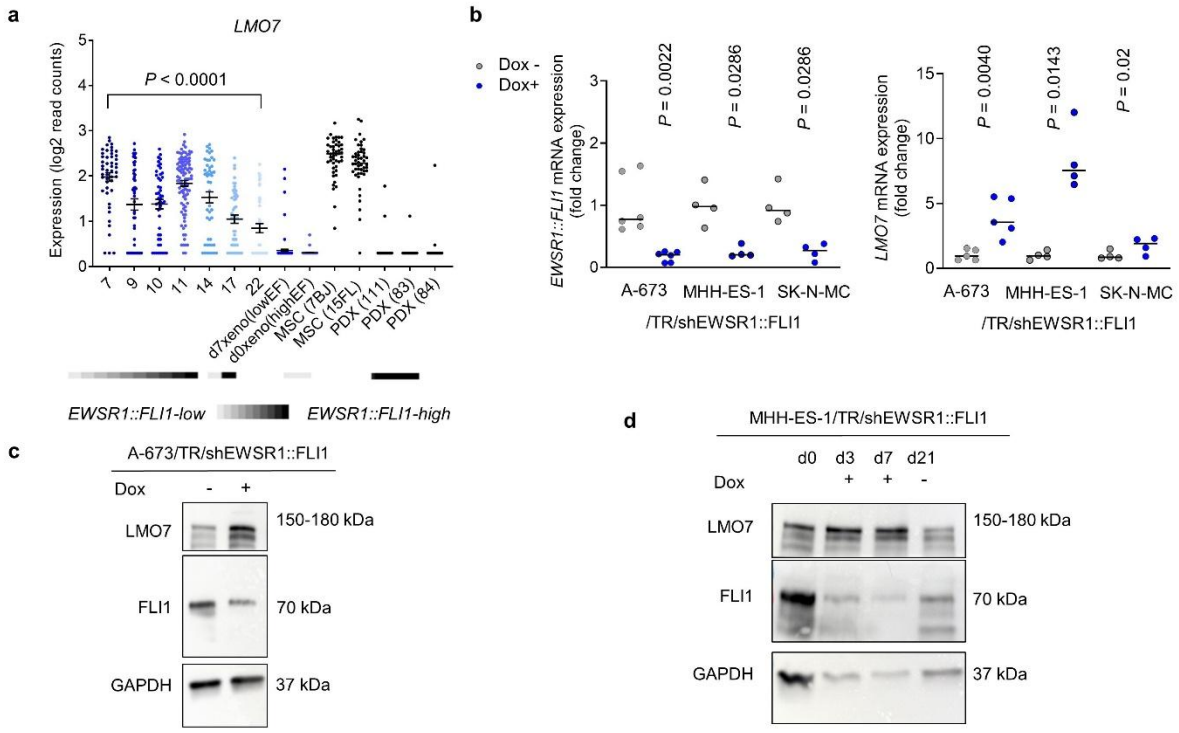

Figure 4.4 EWSR1:.FLI1-high states suppress LMO7 expression. a. Expression of *LMO7* in a single cell RNA-sequencing dataset from A-673/TR/shEWSR1::FLI cell line upon Dox treatment for 7 d followed by Dox washout in the next 15 d. *LMO7* expression in MSCs, and in three EwS patient derived xenografts (PDX) (original dataset from Aynaud et al., (2020), GEO: GSE130025, re-analyzed with special attention to *LMO7* expression). White-to-black gradient indicating increasing *EWSR1:.FLI1* levels. Two-sided Mann-Whitney test between 7 and 22 d of the experimental setup, $P < 0.0001$. **b**. Fusion expression in EwS cells (A-673, MHH-ES-1 and SK-N-MC) containing a Dox-inducible construct for KD of *EWSR1::FLI1*, with/without treatment with Dox for 72 h. *LMO7* expression upon KD of *EWSR1::FLI1* in same cell lines. n ≥ 4 biologically independent experiments. Two-sided Mann-Whitney test. **c.** Western blot using whole cell lysates extracted from A-673/TR/shEWSR1::FLI1 with/without Dox treatment for 72 h. Antibodies against FLI1 and LMO7. Loading control: GAPDH. **d.** Western blot using whole cell lysates from MHH-ES-1/TR/shEWSR1::FLI1 cell line treated with Dox for 7 d (Dox renewal every 48 h), followed by Dox washout in the next 14 d. Antibodies used against EWSR1::FLI1 and LMO7. Loading control: GAPDH.

The opposing expression of EWSR1::FLI1 and LMO7 in many tested systems prompted me to investigate a possible direct *EWSR1::FLI1* regulation of *LMO7* expression. Interestingly, analysis of a ChIP-seq dataset from representative six EwS cell lines, available in R2 Genomic Browser as part of ESCLA, showed two EWSR1::FLI1 DNA binding peaks; one in the proximity of *LMO7* longest transcript TSS and one in the proximity of a shorter *LMO7* transcript TSS (**Figure 4.5a**). EWSR1::ETS binding regions were also identified by R2 Genome Browser as core EWSR1::ETS sites, and were used as a guide to determine which genomic location to clone upstream of a luciferase gene in dual-luciferase reporter system. A

total of three different genomic regions, two of which were core EWSR1::ETS sites (hg19 coordinates: chr13: 76,195,324–76,195,697 and chr13: 76,340,783–76,341,217) were PCR-cloned upstream of the SV40 minimal promoter into a pGL3-Fluc vector and distal *LMO7* promoter upstream from the *LMO7* gene (hg19 coordinates: chr13:76,140,731–76,140,978) was PCR-cloned upstream of luciferase gene into a pGL4-10 vector (**Figure 4.5b**). There were no significant differences in recorded luciferase luminescence upon transfection of the generated reporter systems in A-673 and MHH-ES-1 cells with Dox-inducible EWSR1::FLI1 KD with/without Dox (**Figure 4.5c**).

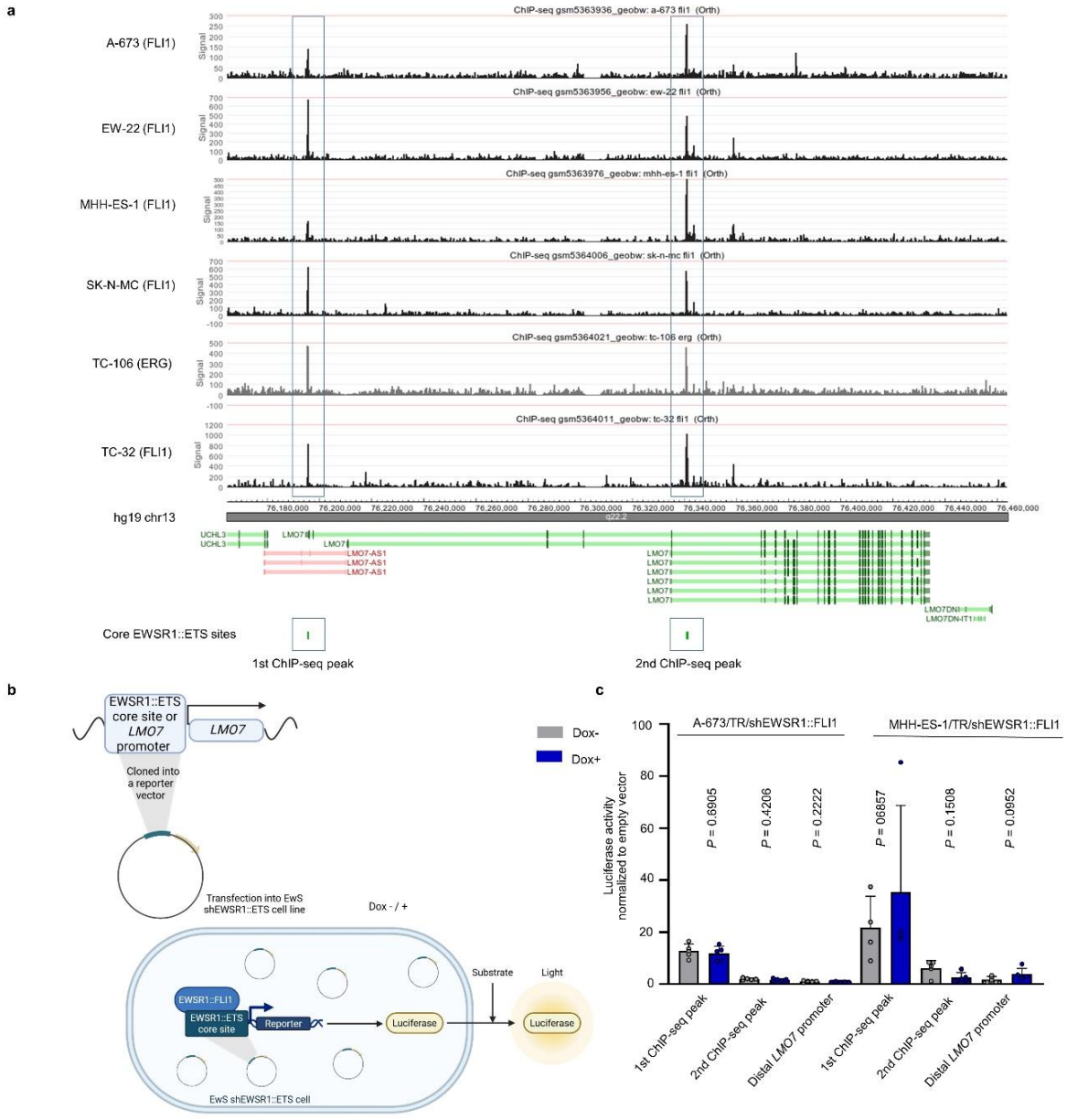

Figure 4.5 *LMO7* is not directly regulated by EWSR1::FLI1 binding in proximity of *LMO7* TSS. **a.** ChIP-seq datasets from FLI1 or ERG DNA binding in six representative EwS cell lines (A-673, EW-22, MHH-ES-1, SK-N-MC, TC-106 and TC-32) from ESCLA dataset (Orth et al., 2022) analyzed in

R2 Genome Browser, with special attention to the genomic region of *LMO7* gene. Blue squares are indicating core ETS sites and EWSR1::ETS binding regions. **b.** Luciferase assay schematic. **c.** Luciferase activity normalized to an empty vector in the conditions with/without Dox. Transfected constructs containing cloned genomic regions of interest (hg19; 1st ChIP-seq peak coordinates: chr13: 76,195,324–76,195,697; 2nd ChIP-seq peak: chr13: 76,340,783–76,341,217 and distal *LMO7* promoter: chr13: 76,140,731–76,140,978) upstream from luciferase gene. Luciferase reporter plasmids were transfected to two EwS cell lines: A-673/TR/shEWSR1::FLI1 and MHH-ES-1/TR/shEWSR1::FLI1, 48 h post treatment with/without Dox. n = 4 biologically independent experiments. Horizontal bars represent the mean and whiskers the SD. Two-tailed Mann-Whitney test ($P > 0.05$)**.**

Hi-ChIP data from Prof. Dr. Didier Surdez (ETH, Zurich) performed in A-673 cell line also showed no direct binding of EWSR1::FLI in the proximity of the *LMO7* TSS, but a possible regulation from a distal unknown chromatin region (indicated with loops). The strongest interaction indicated with an arrow does not include FLI1 peaks (**Figure 4.6a**). Additionally, re-analysis of published ChIP-Seq, Cut&Run, and FAIRE data from three different EwS cell lines (EW502 from Patel et al., 2012, GSE31838; and A-673 and SK-N-MC from Riggi et al., 2014, GSE61953) with a focus on the *LMO7* genomic region demonstrated no direct EWSR1::FLI1 binding in the proximity of *LMO7* TSS in the conditions of with/without EWSR1::FLI1 KD (**Figure 4.6b**). However, re-analysis of the presence and localization of histone mark H3K27ac in ChIP-seq datasets from Ebegboni et al., (2024) (GSE243184) in the proximity of *LMO7* TSS, showed strong opening of chromatin. Enrichment of activating histone marks such as H3K27ac under conditions of EWSR1::FLI1 KD suggests an epigenetic regulation of this gene downstream of the fusion (**Figure 4.6c**).

Recent studies in EwS have shown that pharmacological inhibition of p300/CBP histone acetyltransferases, reduces H3K27ac in EwS and could show effective results both *in vitro* and *in vivo* (Wei et al., 2024). Thus if transcription of *LMO7* is regulated via p300 acetyltransferase activity and H3K27ac, then pharmacological inhibition of p300 would also reduce the expression of *LMO7* and cause a phenotypically similar effect to *LMO7* KD. Reanalysis of RNA-seq data from Wei et al. (2024) (SRA: PRJNA1161150), indicated significant downregulation of *LMO7* expression in all three tested EwS cell lines (A-673, SK-ES-1 and TC-71) upon treatment with p300/CBP inhibitor (iP300w) and could be an indication of regulatory mechanism upstream of *LMO7* in EwS, which is pharmacologically targetable (**Figure 4.6d**).

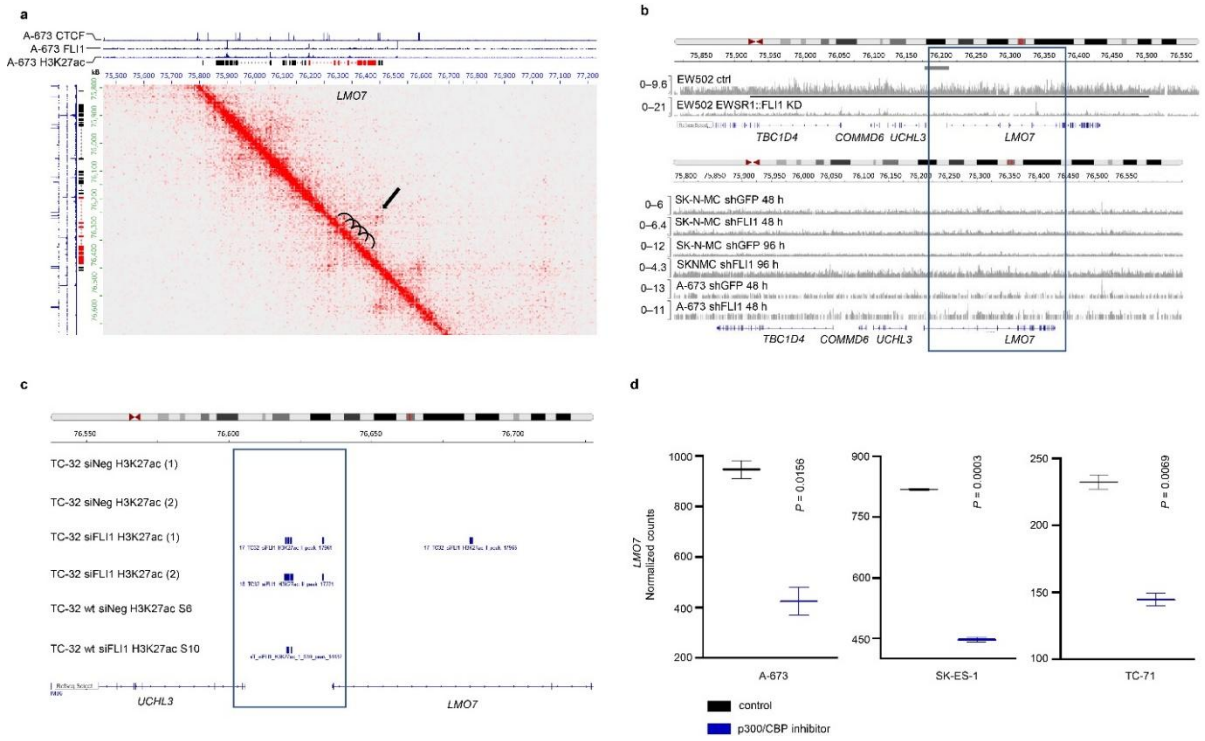

Figure 4.6 H3K27ac in proximity of *LMO7* TSS is present only in *EWSR1::FLI1* KD cells and H3K27ac inhibitors significantly decrease *LMO7* expression in EwS. a. CTCF**,** FLI1 and H3K27ac Hi-ChIP data at *LMO7* genomic locus in A-673 cell line, dataset obtained from Prof. Didier Surdez (ETH Zurich), full dataset published in Surdez et al. (2021), GEO: GSE133228. The strongest interaction indicated with an arrow, and a possible regulation from a distal unknown chromatin region indicated with loops. **b.** ChIP-seq datasets from FLI1 reanalyzed from Patel et al., (2012) (GSE31838), top & Riggi et al., (2014) (GSE61953), bottom, with special attention to the genomic region of *LMO7* gene in the conditions with EWSR1::FLI1 expression (shGFP, for 48 and 96 h) and in conditions of *EWSR1::FLI1* KD (shFLI1) for two tested cell lines: A-673 and SK-N-MC. **c.** Histone mark H3K27ac localization and its presence under conditions with/without *EWSR1::FLI1* KD. Original dataset from Ebegboni et al., (2024) (GSE243184), re-analyzed focusing on the area upstream from *LMO7* TSS in TC-32 cell line. **d.** Re-analysis of RNA-seq dataset from Wei et al., (2024) (SRA: PRJNA1161150), with special focus on *LMO7* expression in cell lines A-673, SK-ES-1 and TC-71 upon treatment with p300/CBP inhibitor (iP300w). Unpaired two-tailed t-test, boxplot at the median and whiskers at min and max individual values. n = 2 biologically independent experiments.

To further investigate epigenetic transcriptional regulation of *LMO7*, DNA methylation analysis was performed for the genomic region of *LMO7* gene, using EwS patient dataset (n = 106) from the INFORM registry (KITZ, Heidelberg). DNA methylation analysis done with Infinium Methylation EPIC Array v1 (Illumina) was available for this group of patients and revealed a total of 77 CpG islands corresponding to the *LMO7* gene. Correlation analysis of *LMO7* expression with methylation (Beta-value) in this EwS patient cohort identified six loci that were statistically significantly positively correlated with *LMO7* expression in this group of patients, while none significantly negatively correlated with *LMO7* expression (**Figure**

4.7a). **Figure 4.7b** shows genomic localization of all CpG islands that were corresponding to *LMO7* gene in this array, while the ones significantly correlated with *LMO7* expression are highlighted with red squares. Of the significant six CpG islands, five were located within the *LMO7* gene body, except the first one, cg22227965 (**Figure 4.7b**, most left square). This CpG island (UCSC_RefGene_Group: TSS1500), is localized 217 bp upstream of the *LMO7* TSS and also significantly correlated with *LMO7* expression in EwS patients (P = 0.003). Those observations show that methylation of cg22227965 upsream of *LMO7* TSS as well as five CpG islands within *LMO7* gene body are associated with *LMO7* expression in this group of EwS patients.

In sum, previous results indicate that *LMO7* expression is affected by EWSR1::FLI1 presence/absence, which also impacts H3K27ac histone acetylation in the genomic region upstream of *LMO7* TSS. As well, in EwS patient samples there is yet another layer of *LMO7* transcriptional regulation where the vicinity of *LMO7* TSS and its gene body are methylated on several genomic locations that are significantly associated with its expression.

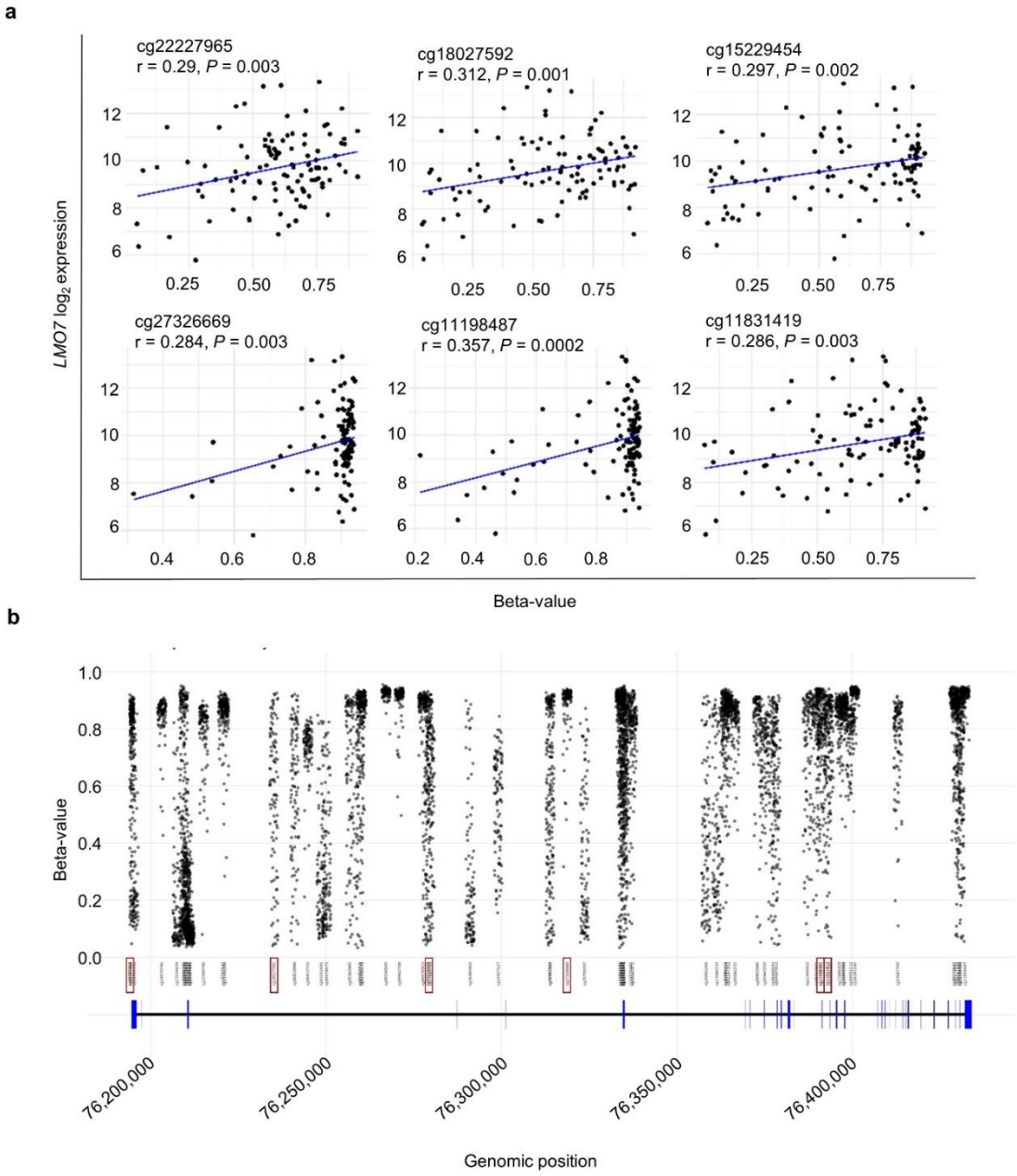

Figure 4.7 *LMO7* gene body methylation positively correlates with its transcriptional activation in EwS patient tumors from the INFORM registry. a. Correlation of *LMO7* $\log_2$ expression and Beta-value shown for six CpG islands in the area of *LMO7* gene that are significantly positively correlated ($P < 0.05$) with *LMO7* expression in INFORM group of patients (n = 106). Methylation profiling performed using Infinium Methylation EPIC Array v1 (Illumina). **b**. Genomic positions of all 77 CpG islands from the array that were indicated to be corresponding to *LMO7* gene. Significantly positively correlated CpG islands with *LMO7* expression from previous analysis (n = 6) are indicated with red squares (from left to right: cg22227965, cg18027592, cg15229454, cg27326669, cg11198487, cg11831419). Genomic location of *LMO7* gene in hg 19 genome version is chr13:76,194,571–76,434,006 and Beta-values for each patient were disclosed above each genomic position.

4.3. Cytoskeleton remodeling and muscle differentiation pathways associate with EWSR1::ETS-low activity area and *LMO7*-high expression in EwS patient datasets

To gain insight into the cell signaling and spatial pathway activity variations in the EWSR1::ETS-low activity area, that is also *LMO7*-high expression area, I utilized the computing tool decoupler-py with pathway gene sets from PROGENy (Badia-i-Mompel et al., 2022; Dimitrov et al., 2024; Schubert et al., 2018). This tool enabled visualization of pathway activity spatial expression for many cancer-relevant signaling pathways on EwS patient sample. There was a trend readily observable for several pathways being higher activated in the EWSR1::ETS-low area. In this area, higher expression was observed for TGFβ, Janus kinase/signal transducers and activators of transcription (JAK-STAT), tumor necrosis factor alpha (TNFα), p53, epidermal growth factor receptor (EGFR), nuclear factor-kappa B (NFκB) and TNF-related apoptosis-inducing ligand (TRAIL) signaling pathways, while MAPK and phosphoinositide 3-kinase (PI3K) signaling pathways had lower expression in EWSR1::FLI1-low area (**Figure 4.8a**).

To further gain insight in the pathways directly correlated to *LMO7* expression, I analyzed a transcriptomic dataset of 196 EwS patients with special attention to *LMO7* associated pathways. For that purpose, I carried out GSEA using the C5 ontology gene sets collection from MSigDB, and subsequent WGCNA of *LMO7* correlated genes in 196 EwS patient cohort. In agreement with the literature, WGCNA confirmed pleiotropic enrichments of gene signatures mainly comprising extracellular matrix remodeling, muscle development, cell adhesion, actin binding, and integrin signaling (**Figure 4.8b**), all of which play important roles in cell migration and metastasis (Cao et al., 2023; Franzetti et al., 2017; He et al., 2019; Wrenn et al., 2023).

Apart from the spatial overlap of the EWSR1::FLI1-low activity area and *LMO7*-high expression area, pathway analysis of those regions, as well as GSEA of 196 EwS patient cohort for pathways correlated with *LMO7* expression also showed functional commonalities. Pathways higher expressed in EWSR1::FLI1-low activity area in spatial transcriptomic analysis, overlaps to a great extent with many functions in which *LMO7* takes part in patient cohort analysis. TNFα, EGFR, TGFβ, JAK-STAT and NFκB pathways all regulate genes and proteins that control cell movement, including integrins, actin-binding proteins, and MMPs (Margadant & Sonnenberg, 2010; Misra et al., 2012; Wu & Zhou, 2010; Xue et al., 2023),

while they are also implicated in muscle cell migration, differentiation, and repair, where most prominent is their role in inhibiting muscle cell differentiation (Alter et al., 2008; Bakkar et al., 2008; Deng et al., 2024; Girardi et al., 2021; Kim et al., 2021; Sitcheran, Cogswell & Baldwin, 2003; Shirakawa et al., 2021, Sun et al., 2007).

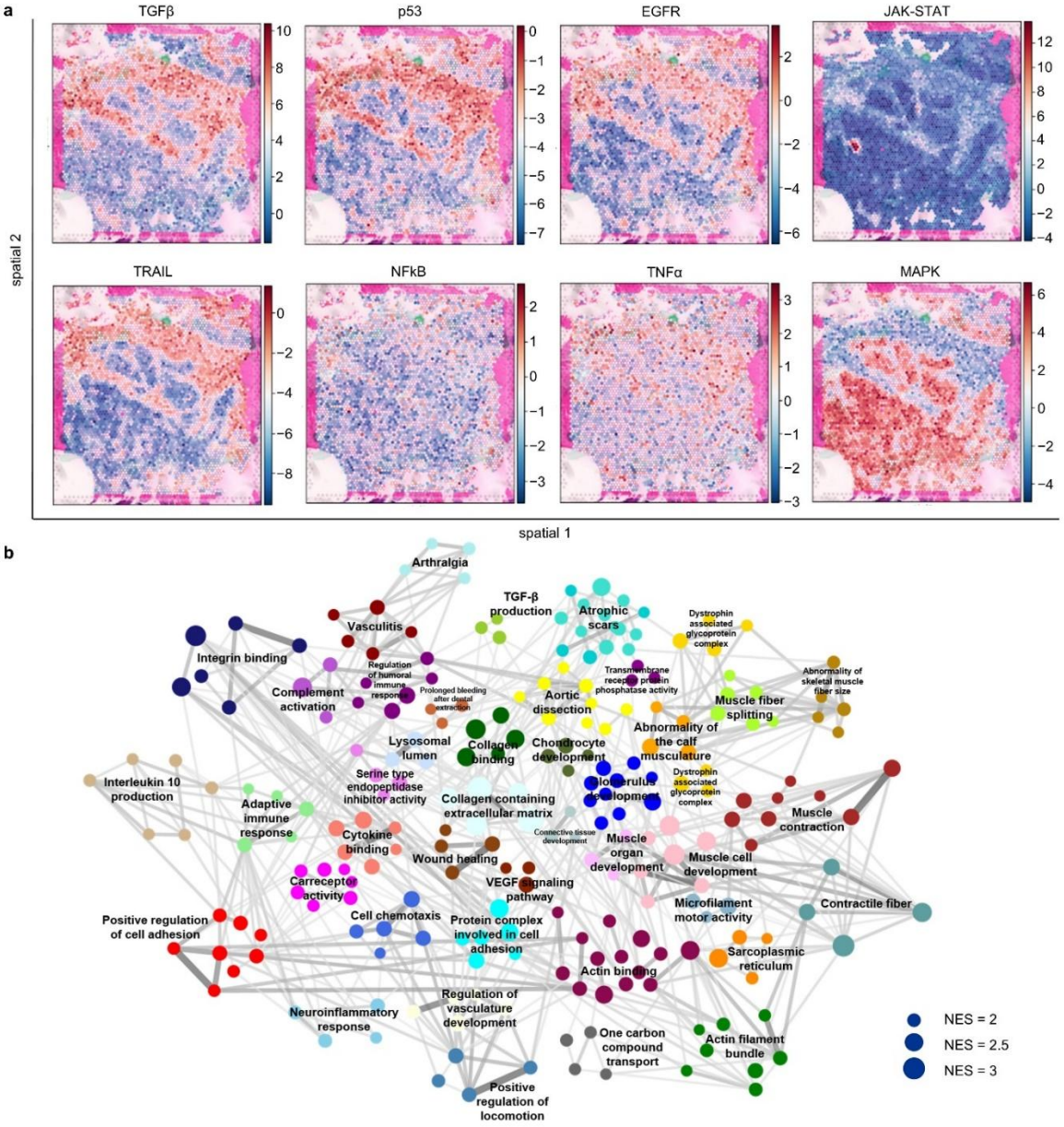

Figure 4.8 Cell signaling pathways enriched in EwS patient samples reveal spatial overlap with fusion states and enrichment of cell migration correlated with *LMO7* expression. a. Selection of cell signaling pathways that have activation patterns corresponding to the distinct areas of EWSR1::FLI1 activity in spatial transcriptomics of EwS patient tumor. **b.** WGCNA of cell signaling pathways positively correlated with *LMO7* expression in 196 EwS patient cohort. Size of each nodule corresponds Normalized Enrichment Score (NES), and color to the specific pathway. $|NES| > 2$, $P < 0.05$.

4.4. Multi-omics LMO7 pathway characterization higlihts its role in EMT of EwS cells

To better discriminate which of these pleiotropic effects are directly mediated by LMO7, a simultaneous transcriptomic and proteomic profiling of three EwS cell lines (A-673, MHH-ES-1, TC-32) with/without RNA interference-mediated silencing of *LMO7* was carried out. To that end, a specific siPOOL targeting *LMO7* (si-G050-4008, siTOOLs Biotech GmbH) or non-targeting negative control (NC) siPOOL (si-C005) was employed that maximizes the on-target effect, while minimizing potential off-target effects (Hannus et al., 2014). As well, a relatively early time point after transfection (55 h), was chosen to capture better, likely acute effects of *LMO7* KD rather than late potentially compensatory effects. As shown in **Supplementary Figure 7.2a**, the employed siPOOL (at a concentration of 5 nM) led to a 9–13% *LMO7* residual expression on average per cell line. Affymetrix Clariom D Human microarrays and data preprocessing captured 21,324 uniquely mapped transcript IDs (with available Entrez ID and excluding small, non-coding pseudogene or similar RNA transcripts). Pre-processed expression matrices were analyzed using limma, yielding $\log_2$ fold changes and adjusted *P*-values for *LMO7* knockdown versus negative control conditions pooled across cell lines. The employment of a siPOOL targeting *LMO7*, resulted in *LMO7* as the single most downregulated transcript between treatment and negative control but also, there was a downregulation in many ECM and cancer relevant transcripts like matrix metallopeptidase 2 (*MMP2*), synaptotagmin 11 (*SYT11*), and mitogen-activated protein kinase kinase kinase 12 (*MAP3K12*) (**Figure 4.9a**). Interestingly, when performing GSEA on pooled samples from all three tested cell lines, the strongest downregulated pathway in Hallmark gene sets (MSigDB) was EMT, followed by mitotic spindle and among others myogenesis. Among upregulated pathways were ones related to immune response like interferon alpha and gamma response (**Figure 4.9b**).

Furthermore, the same experimental setup in three EwS cell lines was utilized for capturing the changes in cells on the proteome level upon *LMO7* KD. Here, after 55 h of siPOOL treatment, protein lysates were delivered for mass spectrometry-based proteomics in collaboration with the lab of Dr. Ashok Kumar. The analysis yielded a set of 7,799 proteins. In PCA samples clustered according to the cell line of origin, while Z-score heat map in **Figure 4.9c** highlights the first cluster (Cluster 1), which separated the samples according to LMO7 KD. Within Cluster 1, 15% of all proteins were marked by Perseus software as related to cell cycle, which consisted of proteins like aurora kinase A (AURKA), Rho associated coiled-coil containing protein kinase 1 (ROCK1), and mitotic arrest deficient 2 like 2 (MAD2L2).

Furthermore, GSEA on pooled samples from all three tested cell lines using the Hallmark gene sets (MSigDB) revealed EMT as the strongest downregulated pathway, resembling transcriptomic analysis, followed by downregulation in apical junction and mitotic spindle. Here, the strongest upregulated pathway was oxidative phosphorylation but also, interferon alpha response was upregulated similar to the transcriptomic analysis (**Figure 4.9d**).

Integrative analysis of transcriptomic and proteomic data was performed in order to find common candidates downstream of LMO7 that were also downregulated at both the RNA and protein level. Pre-processed expression matrices were analyzed using limma, yielding $\log_2$ fold changes and adjusted *P*-values for LMO7 knockdown versus negative control conditions pooled across cell lines. To identify concordantly expressed genes/proteins, only features present in both cases (n = 6,438) were retained. There were many interesting hits, some of which roles were previously described in EwS metastasis like IL1RAP (Zhang et al., 2021a) or actin beta (ACTB) (Katschnig et al., 2017) (**Figure 4.9e**). To identify consistently enriched biological processes, GSEA was performed independently on both datasets using the C2 CGP collection from MSigDB. Normalized enrichment scores (NES) were integrated using quadrant-based classification to identify common pathways, visualized with scatter plots highlighting concordant pathways (|NES| > 1.5, adjusted *P*-value < 0.5, otherwise no/almost no results for fGSEA analysis on differentially expressed pathway list depending on selected gene set collection). Strikingly, integrative GSEA analysis revealed negative enrichment of genes upregulated in the EMT upon TGFβ stimulation, as well as oxidative phosphorylation positively enriched (**Figure 4.9f**) further supporting a role of LMO7 in cell migration and metastasis.

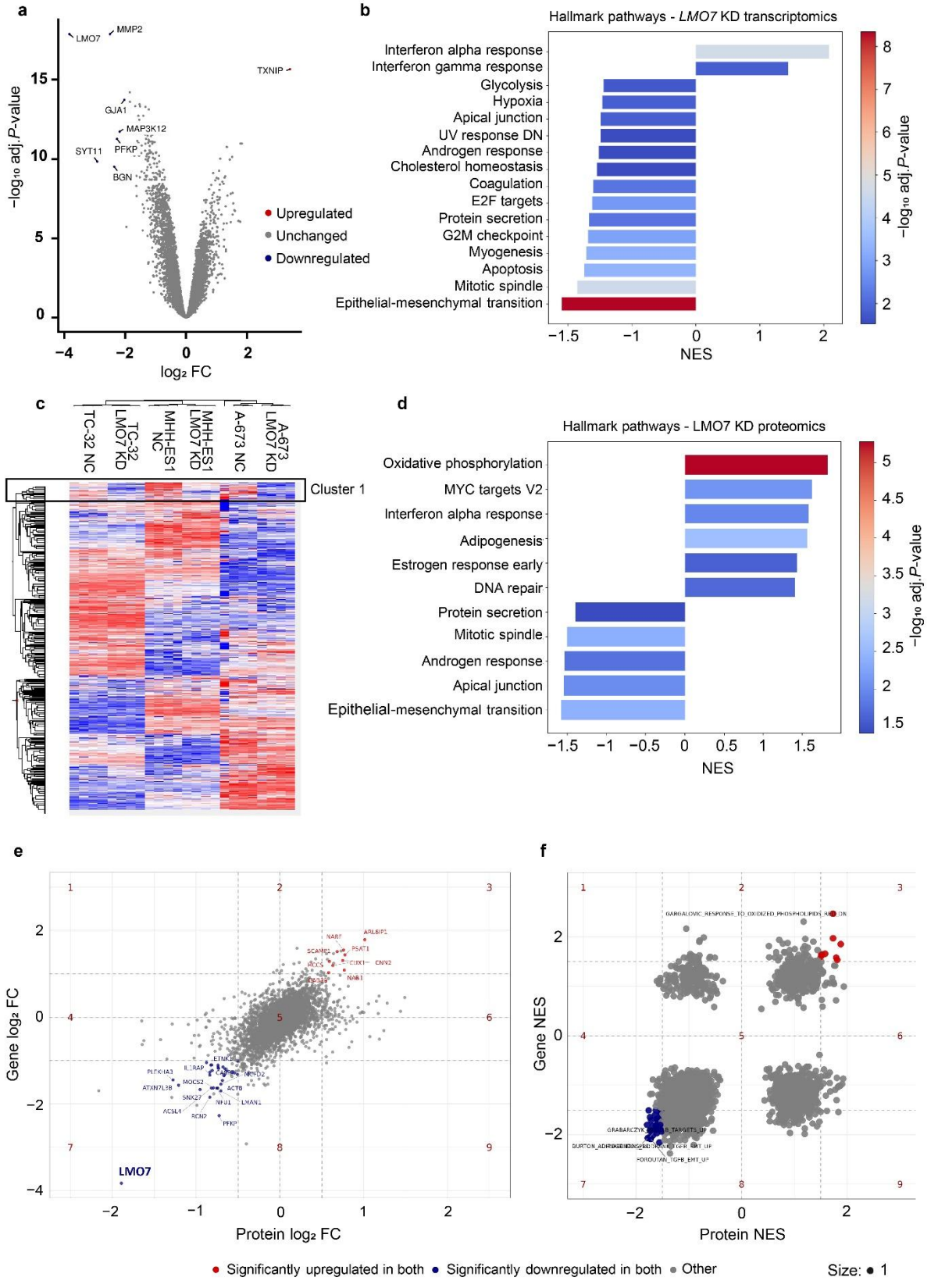

Figure 4.9 Integrated transcriptomics and proteomics of LMO7 downstream pathways reveal enrichment of EMT signaling, and ACTB. a. Volcano plot showing the most significantly up- or down-regulated genes in transcriptomic analysis upon 55 h *LMO7* KD in three EwS cell lines (A-673, MHH-ES-1, TC-32).The blue dots indicate significantly differentially downregulated, while red

upregulated genes ($|\log_2 FC| > 2$; $P < 0.05$). **b.** Most significantly differentially expressed pathways from transcriptomic analysis in two conditions (NC and *LMO7* KD) in three EwS cell lines (A-673, MHH-ES-1 and TC-32) from curated gene sets Hallmarks (MSigDB). Red represents higher and blue represents lower $-\log_{10}$ adjusted *P*-value. $|NES| > 1.5$, $P_{adj} < 0.05$. **c.** Heat map based on the Z-score of proteomic analysis of two conditions (NC and LMO7 KD) in 3 EwS cell lines (A-673, MHH-ES-1, TC-32). Cluster 1 highlighted as the one containing detected proteins that are affected by the condition of LMO7 KD. **d.** Most significantly differentially expressed pathways from proteomic analysis in two conditions (NC and LMO7 KD) in three EwS cell lines (A-673, MHH-ES-1 and TC-32) from curated gene sets Hallmarks (MSigDB). Red represents higher and blue represents lower $-\log_{10}$ adjusted *P*-value. $|NES| > 1.5$, $P_{adj} < 0.05$. **e.** Integrated analysis of transcriptomic and proteomic datasets performed in two conditions (NC and LMO7 KD), in three EwS cell lines (A-673, MHH-ES-1 and TC-32). The blue dots indicate significantly differentially commonly downregulated, while red upregulated genes and proteins, $|\log_2 FC| > 1$ for genes, $|\log_2 FC| > 0.5$ for proteins, $P_{adj} < 0.05$ for both. **f.** Analysis of differentially expressed pathways on integrated transcriptomic and proteomic datasets from two conditions (NC and LMO7 KD), in three EwS cell lines (A-673, MHH-ES-1 and TC-32) using C2 CGP collection (MSigDB). The blue dots indicate significantly concordantly differentially downregulated, while red upregulated pathways, ($|NES| > 1.5$, $P_{adj} < 0.5$* otherwise no/almost no results for fGSEA analysis on DEP list depending on selected gene set collection.

4.5. Nucleo-cytoplasmic localization of LMO7 in EwS cells

LMO7 has been previously described as a nucleocytoplasmic shuttling protein in HeLa cells (Holaska et al., 2006). This was an indication to further investigate LMO7 localization in EwS cells. For that purpose, cellular fractionation followed by immunoblotting, and IF imaging were performed. Firstly, cytoplasmic and nuclear fractioning followed by immunoblotting confirmed the presence of LMO7 in both cell fractions, under conditions with/without Dox in A-673/TR/shEWSR1::FLI1 cells (**Figure 4.10a**). Interestingly, LMO7 signal in the nuclear fraction was stronger in EWSR1::FLI1 KD condition, which was in line with previous findings of this thesis (**Figure 4.4**).

Secondly, LMO7 localization was also validated via IF. For that purpose, as well as to further investigate phenotypical changes in EwS cells upon *LMO7* KD *in vitro* and *in vivo* (in detail explained in the following chapters), EwS cell lines with Dox-inducible shRNA targeting *LMO7* were generated utilizing lentiviral transduction system. Those cell lines contained Dox-inducible shRNA targeting *LMO7*, named hereafter A-673/TR/shLMO7 and MHH-ES-1/TR/shLMO7, using one of two different shRNAs against *LMO7* (sh491, targeting 5´UTR and CDS, and sh492 targeting CDS only), and respective non-targeting controls. Using generated cell lines for IF imaging, LMO7 (white) localization could be readily detected within the nuclei (DAPI, blue) and in the cytoplasm of EwS cells. In the nucleus, LMO7 staining had

a specular pattern, while in the cytoplasm it was more fibrous. However, upon *LMO7* KD, both nuclear and cytoplasmic signal were reduced (**Figure 4.10b**).

Due to LMO7 potential role in EwS metastasis and involvement with cellular cytoskeleton, I also performed cellular staining with phalloidin, which binds to F-actin, a filamentous, polymeric form of β-actin (ACTB) (red), followed by IF imaging. Here, upon *LMO7* KD there was a noticeable reduction of not only LMO7 (white) signal, but also F-actin (red) signal, as well as reduction in their colocalization signal normalized to DAPI (**Figure 4.10 c–d**). These results are directly concordant with previous findings from integrative transcriptomic and proteomic analysis, which indicated ACTB as one of the top hits being downregulated upon *LMO7* KD (**Figure 4.9e**).

Conversely, upon IF imaging of ACTB and LMO7 in A-673/TR/shEWSR1::FLI1 and MHH-ES1/TR/shEWSR1::FLI1 cells with Dox inducible *EWSR1::FLI1* KD, both ACTB (phalloidin) and LMO7 were found to have enhanced IF signal (**Figure 4.10e**). This was concordant with previous findings of this thesis on LMO7 expression in respect to EWSR1::FLI1 oscillations (**Figure 4.2** and **Figure 4.4**), as well as with findings from the literature on ACTB in EwS cells (Chaturvedi et al., 2014; Franzetti et al.,2017; Katschnig et al., 2017). Finally, in order to test potential involvement of LMO7 with focal adhesions, A-673/TR/shLMO7 and MHH-ES-1/TR/shLMO7 cells were stained for vinculin (green). Upon *LMO7* KD, vinculin staining showed reduced/absent punctate pattern (especially in A-673/TR/shLMO7_492 cells, **Figure 4.10f**), suggesting compromised cell-matrix adhesion and disrupted focal adhesion formation that could further affect the migration ability of *LMO7* KD cells. Strong reduction of LMO7 (white) signal was noticeable in MHH-ES-1/TR/shLMO7 upon addition of Dox and *LMO7* KD, as well as general reduction of vinculin (green) signal (**Figure 4.10g**).

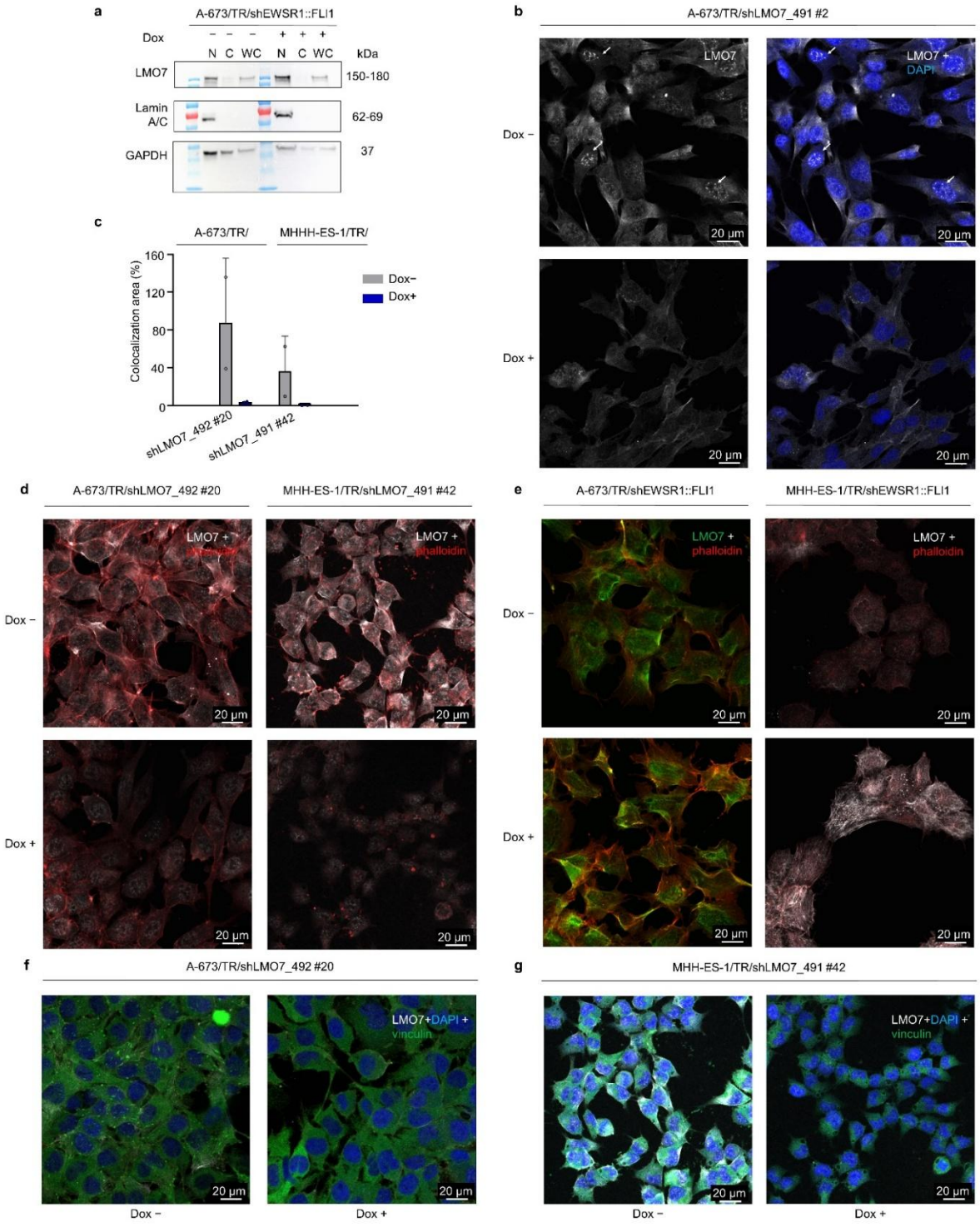

Figure 4.10 LMO7 has a nucleo-cytoplasmic cellular localization and colocalizes with actin. a. Immunoblotting of protein extracts after cellular fractionation using Nuclear Extract Kit (Active Motif). Nuclear (N), cytoplasmic (C), and whole cell lysates (WC) of proteins extracted from A-673/TR/shEWSR1::FLI1 cells upon treatment with/without Dox for 72 h. Antibodies used against: LMO7, Lamin A/C (only nuclear localization) and GAPDH (mostly cytoplasmic localization). **b.** Representative IF images of A673/TR/shLMO7_491 #2 cells treated with/without Dox for 72 h. Specular nuclear localization of LMO7 indicated with arrows. LMO7 (white) and DAPI nuclear staining (blue). Results are representative of three experiments. **c.** Colocalization area (%) of LMO7 and phalloidin signal, according to the area and brightness above set threshold for both channels and

normalized to DAPI staining. Area of colocalization assesed using Fiji. Results are representative of two experiments. Horizontal bars represent the mean and whiskers the SD. **d.** Representative IF images of A-673/TR/shLMO7_492 #20 and MHH-ES-1/TR/shLMO7_491 #42 cells treated with/without Dox for 72 h. LMO7 (white) and phalloidin- F-actin (red) staining. **e.** Representative IF images of A-673/TR/shEWSR1::FLI1 and MHH-ES-1/TR/shEWSR1::FLI1 cells treated with/without Dox for 72 h. LMO7 (green) and phalloidin- F-actin (red) staining, colocalization area (yellow to orange) (left panel) and LMO7 (white) and phalloidin- F-actin (red) (right, panel). **f–g.** Representative IF images of A-673/TR/shLMO7_492 #20 and MHH-ES-1/TR/shLMO7_491 #42 cells treated with/without Dox for 72 h. LMO7 (white), vinculin (green) and DAPI nuclear staining (blue). Results are representative of three experiments. All IF images in all panels are adjusted to the same brightness and contrast.

4.6. LMO7 reduces clonogenicity and metastatic burden of EwS *in vitro* and *in vivo*

To functionally investigate the role(s) of LMO7 in EwS cells *in vitro* and *in vivo*, two previously descrbed EwS cell lines were generated utilizing lentiviral transduction system so that they contain Dox-inducible shRNA targeting *LMO7*. Dox-treatment after 72 h in both A-673/TR/shLMO7 and MHH-ES-1/TR/shLMO7 led to efficient KD of *LMO7* at the mRNA, with 15–20% residual *LMO7* expression after KD, and also at the protein level (**Figure 4.11a**). Since outgrowth of single cells is a key feature of metastasis (Celià-Terrassa & Kang, 2016), 2D CFAs were carried out using previously generated cell lines with Dox-inducible *LMO7* KD. As shown in **Figure 4.11b**, conditional KD of *LMO7* dramatically reduced the capacity of single EwS cells to form colonies when seeded at low densities and was statistically significant for both shRNAs targeting *LMO7* in both A-673 and MHH-ES-1 cell lines ($P_{\text{A-673/TR/shLMO7\_491}} = 0.0317$; $P_{\text{A-673/TR/shLMO7\_492}} = 0.0317$; $P_{\text{MHH-ES-1/TR/shLMO7\_491}} = 0.0286$; $P_{\text{MHH-ES-1/TR/shLMO7\_492}} = 0.0286$). Such phenotype was not observed in non-targeting control cell lines (**Figure 4.11b**). To validate these results with two independent methods, constitutional CRISPR-Cas9 mediated knockout (KO) of *LMO7* or Dox-inducible overexpression (OE) of full-length *LMO7* were generated in EwS cell lines A-673 and TC-32. For both methods, change in expression levels of LMO7 at the protein level were tested using immunoblotting. Additionally, *LMO7* KO with frameshift mutation was confirmed with gel electrophoresis and Sanger sequencing. Notably, knockout of *LMO7* phenocopied the result from the CFAs observed upon shRNA-mediated knockdown of the gene, leading to an even stronger reduction in colony formation in respective cell line ($P = 0.0286$) (**Figure 4.11c**). In contrast, conditional OE of *LMO7* significantly enhanced clonogenic capacity of TC-32 cells ($P = 0.0286$) (**Figure 4.11d**).

In order to further validate the functional role of LMO7 in EwS, 3D sphere viability as well as migration assays were performed. *LMO7* silencing reduced 3D sphere viability of A-

673 and MHH-ES-1 EwS cells (**Figure 4.11e**) measured with CellTiter-Glo Luminescent Cell Viability Assay. Since the omics-analyses of patient data and cell lines (**Figure 4.2c, d**; **Figure 4.3a, d**, and **Figure 4.9b, d**) suggested a role of LMO7 in migration and invasion, I next carried out transwell migration assays of EwS cell lines with/without Dox treatment for *LMO7* KD induction. Cells were pretreated with/without Dox for 72 h and serum-starved for final 24 h, before being seeded in transwell inserts. Here, migration towards an FCS-rich compartment was assessed after 24 h, when cells were fixed and stained with crystal violet. Absorbance was measured at 600 nm only for the cells that migrated through the porous transwell membrane to the FCS-rich compartment. As shown in **Figure 4.11f**, *LMO7* silencing significantly reduced cellular migration in two different cell line models when comparing absorbance of treatment and control.

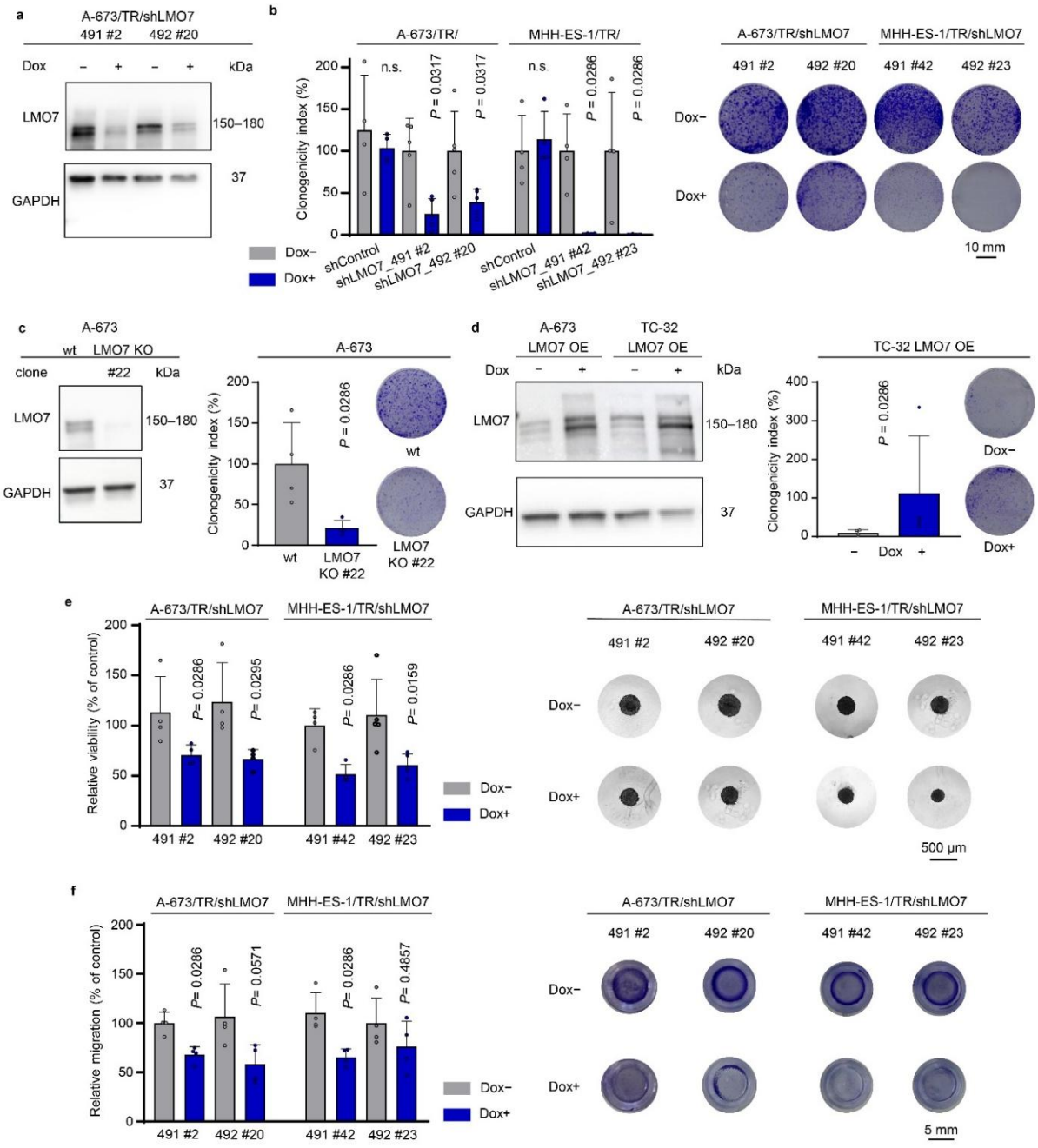

Figure 4.11 Silencing of *LMO7* leads to decreased clonogenicity and migratory potential of EwS cells *in vitro*. a. Representative western blot of LMO7 protein expression after establishing single cell clones with independent Dox-inducible shRNA targeting LMO7 (491, 492) in A-673/TR/ and MHH-ES-1/TR/ cells. **b.** Relative clonogenicity of single clones A-673/TR/shLMO7_491 #2, A-673/TR/shLMO7_492 #20, MHH-ES-1/TR/shLMO7_491 #42 and MHH-ES-1/TR/shLMO7_492 #23 cells following 10 days of Dox-treatment (left) and representative colony images (right). n = 4 biologically independent experiments. Horizontal bars represent the mean and whiskers the SD. Two-tailed Mann-Whitney test. **c.** Representative western blot of LMO7 protein expression after establishing single cell clones with constitutive *LMO7* KO in A-673 cell line (left). Relative clonogenicity of A-673 wt and A-673-LMO7KO #22, following 10 days of Dox-treatment and representative colony images (right). Scale bar corresponds to the one in b. n = 4 biologically independent experiments. Horizontal bars represent the mean and whiskers the SD. Two-tailed Mann-Whitney test. **d.** Representative western

blot of LMO7 protein expression after establishing cell lines with Dox-inducible LMO7 OE in A-673 and TC-32 cell line (left). Relative clonogenicity of TC-32-LMO7OE, following 10 days of Dox-treatment and representative colony images (right). Scale bar corresponds to the one in b. n = 4 biologically independent experiments. Horizontal bars represent the mean and whiskers the SD. Two-tailed Mann-Whitney test. **e.** Relative cell viability of A-673/TR/shLMO7 and MHH-ES-1/TR/shLMO7 (491 and 492) spheroids, assessed by CellTiter-Glo assay, following 96 h treatment with/without Dox (left) and representative images of spheroids (5× objective, right). n = 4 biologically independent experiments. Horizontal bars represent the mean and whiskers the SD. Two-tailed Mann-Whitney test. **f.** Relative cell migration of A-673/TR/shLMO7 and MHH-ES-1/TR/shLMO7 (491 and 492) cells pretreated for 72 h with/without Dox. Cell migration assessed by transwell assay, in the span of 24 h from seeding cells in both conditions (left). Representative images of cells that migrated across the transwell porous membrane (8 μm), (right). n = 4 biologically independent experiments. Horizontal bars represent the mean and whiskers the SD. Two-tailed Mann-Whitney test.

In order to further validate the findings on the role(s) of LMO7 for EwS tumor growth and migration, generated cell lines with Dox-inducible *LMO7* KD were utilized for *in vivo* experiments. Firstly, in order to follow the local tumor growth, A-673/TR/shLMO7_491 #2 was injected subcutaneously into immunocompromised Nod/Scid/gamma (NSG) mice. Similar to observations made *in vitro*, where *LMO7* KD led to reduction of sphere formation (**Figure 4.11e**), the effect was also mirrored in an *in vivo* setting where a significant delay of local tumor growth was observable in mice upon Dox treatment (P = 0.002) (**Figure 4.12a,** left). Furthermore, IHC of mice tumors stained for LMO7 (brown) revealed successful *LMO7* KD in Dox-treated mice, as well as confirmed nucleo-cytoplasmic localization of LMO7 (**Figure 4.12a**, right). Additionally, this reduction in local tumor growth upon *LMO7* KD was accompanied by a significant reduction of mitotic index (P = 0.0003) and a proportionally significant increase in the number of apoptotic bodies (P = 0.0003), while no significant differences in percentage of necrotic area among two conditions were observed (**Figure 4.12b**). Even stronger effect on local tumor growth was observed in MHH-ES-1/TR/shLMO7_492 #23, where local tumors were significantly smaller in size and weight in comparison with control mice ($P_{\text{tumor volume}}$ = 0.0007, $P_{\text{tumor weight}}$ < 0.0001) (**Figure 4.12c**, left and lower panel). Furthermore, H&E staining of these tumors revealed that the remaining tissue growth in the Dox-treated group was scar/fat tissue (**Figure 4.12c**, right panel), which further confirmed the tumor regression phenotype upon *LMO7* KD, displayed in the growth curve.

To further test the role of LMO7 in migration and metastatic spread *in vivo*, a spontaneously metastasizing orthotopic xenograft mouse model was used. Here, *LMO7* KD not only significantly suppressed primary tumor growth in the tibial bone (P = 0.0002) but also

showed significant inhibition of cell ability to form metastases *in vivo* in all animals tested (P = 0.0014) (**Figure 4.12d**). Likewise, macro-metastases in the liver of Dox-treated mice were completely absent (P = 0.0014), and their liver weight was significantly smaller (P = 0.0002) than in control mice (**Figure 4.12d**, right and below). Collectively, these *in vitro* and *in vivo* data confirm a functional role of LMO7 in tumor progression and metastasis of EwS.

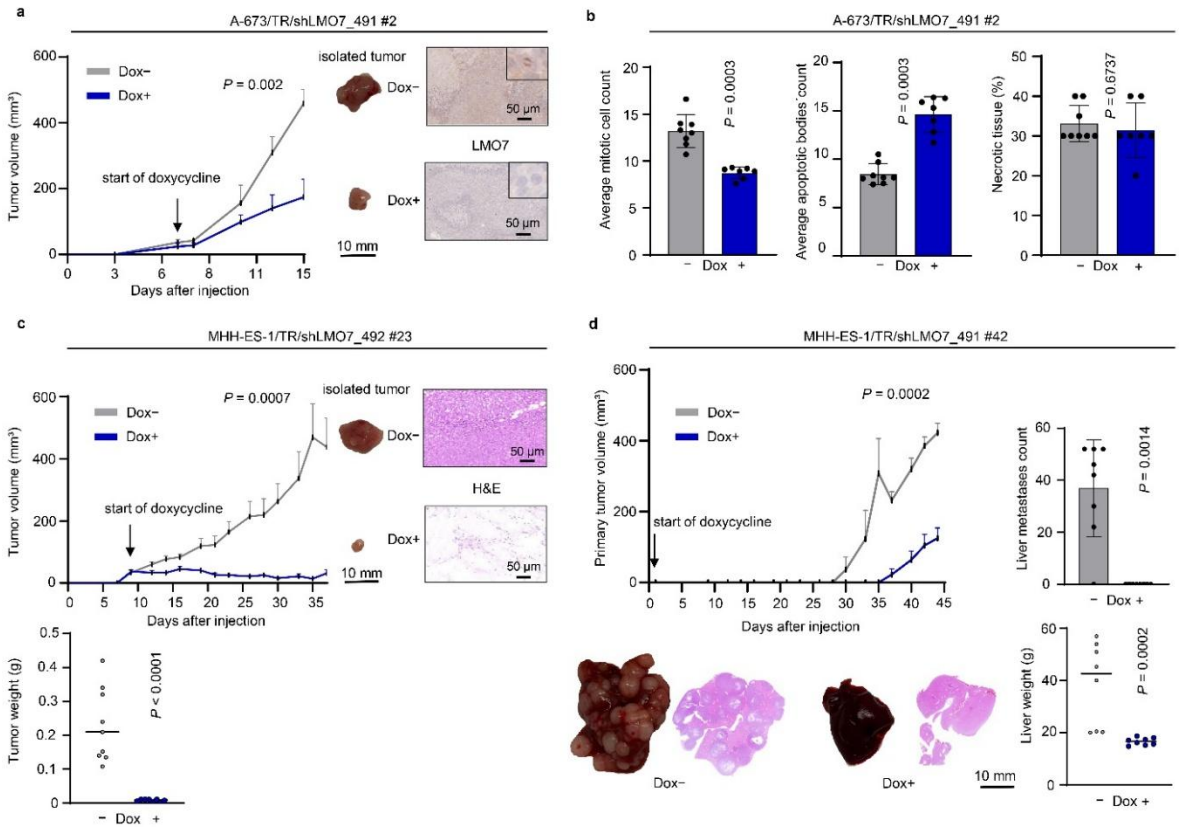

Figure 4.12 LMO7 promotes tumor growth and metastasis of EwS *in vivo*. a. Measurements of tumor volumes (mm^3) over time (days) in subcutaneous injection of A-673/TR/shLMO7_491 #2 with/without Dox-mediated *LMO7* silencing (left). n = 8 animals/condition. Unpaired two-tailed Mann-Whitney test for endpoint tumor sizes. Representative images of xenografts (scale bar at 10 mm) and respective IHC stainings using anti-LMO7 antibody (PA5-54281, Invitrogen) at 40× objective magnification (right). Scale bar at 50 µm. **b.** Average mitotic cell count, apoptotic bodies and necrotic area in each H&E xenograft staining from subcutaneous injection A-673/TR/shLMO7_491 #2 cells. For each xenograft H&E staining, ten fields at 40× objective magnification were observed per sample and average of each was used to make a graph. n = 8 biologically independent xenografts/condition. Horizontal bars represent the mean and whiskers the SD. Two-tailed Mann-Whitney test. **c.** Measurements of tumor volumes (mm^3) over time (days) in subcutaneous injection of MHH-ES-1/TR/shLMO7_492 #23 with/without Dox-mediated *LMO7* silencing (left). n = 9 animals/condition. Horizontal bars represent the mean and whiskers the SD. Two-tailed Mann-Whitney test for endpoint tumor sizes. Representative xenograft images (scale bar at 10 mm) and their respective H&E stainings at 40× objective magnification (right). Scale bar at 50 µm. Tumor weight of both groups at the endpoint (below). n = 9 biologically independent xenografts. Two-tailed Mann-Whitney test. **d.** Measurements of leg circumference (mm^3) over time (days) in orthotopically injected MHH-ES-1/TR/shLMO7_491

#42 with/without Dox-mediated *LMO7* silencing into right tibia bone (left). n = 8 biologically independent animals/conditions. Unpaired two-tailed Mann-Whitney test for endpoint tumor sizes. Number of hepatic macro-metastases observed in each mouse (right). n = 8 animals/condition. Horizontal bars represent the mean and whiskers the SD. Two-tailed Mann-Whitney test. Representative images of livers with respective H&E staining of both conditions (below). Liver weight (g) of both groups at the endpoint. n = 8 animals/condition. Two-tailed Mann-Whitney test.

4.7. *circLMO7* is dependent on *LMO7* expression levels *in vivo*

Circulating tumor cells and exosomes are the key for transitioning and preparing tumor microenvironment for local invasion and metastatic spread (Liu et al., 2022; Luo et al., 2023; Zhan et al., 2023). This prompted me to investigate further if LMO7 could have a direct impact on communication between cells to aid in transitioning from localized invasiveness to metastatic spread. A recent study from Luo et al. (2024) showed that circular *LMO7* RNA (*circLMO7*) was transmitted via exosomes and was important in osteosarcoma development, while Wei et al. (2017) showed its importance for inhibiting myoblast differentiation. *circLMO7* is derived from circular covalent binding of exons 3, 4 and 5 spliced from parental linear *LMO7* mRNA (**Figure 4.13a**) (Luo et al., 2024). Given the circular structure of *circLMO7*, I utilized the specifically designed RT-qPCR junctional primers from Luo et al. (2024) for quantification of *circLMO7,* which do not attach to the parental *LMO7* gene. In order to capture both possible intra- and extracellular *circLMO7*, RNA was isolated from xenograft tumors from previously described mouse experiments. Parts of tumorous tissue (including the stroma and extracellular matrix) were lysed for downstream analysis. **Figure 4.13b** shows both significant downregulation of parental linear *LMO7* mRNA (P = 0.003) and significant downregulation of *circLMO7* (P = 0.0007) in the same mice tumors upon Dox treatment. The downregulation of *circLMO7* upon parental gene KD is a direct consequence of reduced primary transcript availability, which shows that *circLMO7* is transcriptionally coupled to its host gene. As previously shown, *LMO7* expression is significantly associated with worse prognosis and metastatic disease in EwS and with spontaneous development of metastases in EwS *in vivo* models (**Figure 4.3; Figure 4.12**).

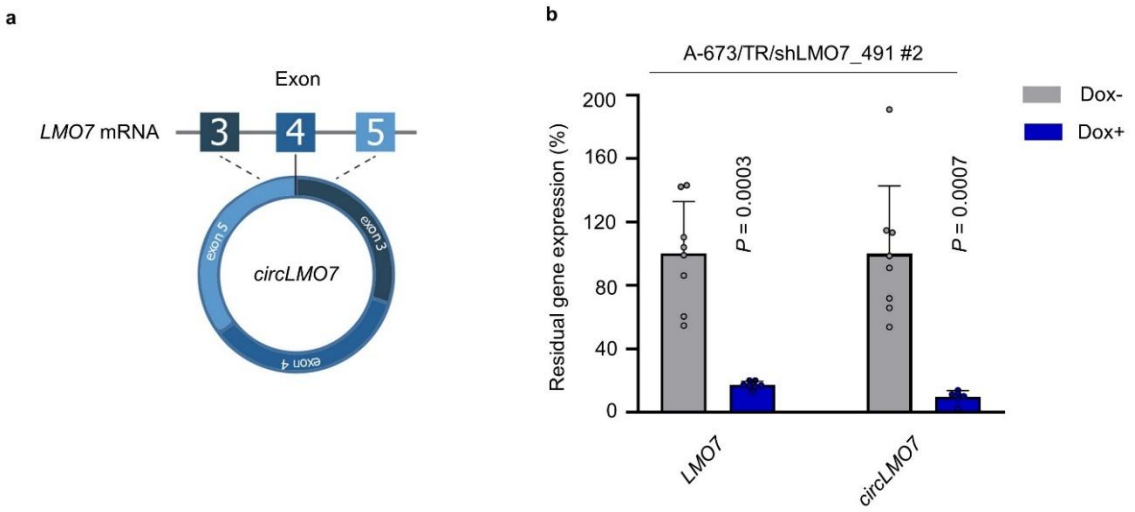

Figure 4.13 *circLMO7*, exosomally-transmitted small circular RNA, has reduced expression in EwS upon LMO7 KD. a. Schematic of *circLMO7* structure. *circLMO7* is derived from circular covalent binding of exons 3, 4 and 5 spliced from parental gene *LMO7* mRNA. Figure modified according to Luo et al. (2024), PMID: 38742566. Open Access article published with license by Taylor & Francis Group, LLC. The article has been distributed under a Creative Commons CC BY license, whereas reuse of this material for non-commercial/educational purposes is possible without obtaining additional permissions. **b.** *LMO7* mRNA and *circLMO7* expression, measured in RNA isolated from mice tumors. *RPLP0* was used as a housekeeping gene in both cases. *circLMO7* primer sequences for RT-qPCR obtained from the study by Luo et al. (2024).

5. DISCUSSION

5.1. Implications of multi-omics approach for elucidating the metastatic process and discovery of novel clinically relevant targets in EwS

Omics technologies have revolutionized cancer research by enabling the comprehensive characterization of the molecular complexities that drive tumor initiation, progression, and heterogeneity (Chakraborty et al., 2024). The integration of omics technologies provides an unprecedented opportunity to bridge basic scientific discoveries with translational applications, ultimately informing novel diagnostics, biomarkers, and personalized therapeutic strategies for cancer patients (Yates et al., 2025).

One of the biggest projects that integrated knowledge from omics-technologies in EwS was the Ewing Sarcoma Cell Line Atlas (ESCLA), a comprehensive resource profiling 18 EwS cell lines using whole-genome sequencing, DNA methylation arrays, gene expression and splicing arrays, proteomics, and ChIP-seq for fusion proteins and histone marks. This atlas enabled the study of expression regulation, cellular heterogeneity, and the impact of fusion oncogene knockdown in EwS cell lines (Orth et al., 2022). Similar studies have also continued recently utilizing a spontaneous metastasis mouse model in EwS (Chicón-Bosch et al., 2025). These studies have combined transcriptomics, proteomics, and methylomics to identify key drivers of metastasis and poor prognosis in this disease. By integrating various omics technologies, signaling cascades and candidate genes enriched in metastases have been identified, that could be influencing EwS agressivness. Experimental validation of two of these candidates, cyclic AMP-responsive element-binding protein 1 (CREB1) and lipoxygenase homology domain-containing protein 1 (LOXHD1), showed an association with migration and clonogenic potential (Chicón-Bosch et al., 2025). Additionally, studies that utilize single-cell technologies in EwS are just starting to develop in recent years, while spatial technologies are fully lacking. The first comprehensive study that utilized patient material using single-cell RNA-sequencing to study the TME of EwS was from Visser et al. (2023). However, scRNA-seq studies ultimately lack the spatial information required to correlate transcriptional state dynamics with tumor topography (Arora et al., 2023), while spatial transcriptomics can obtain information about the TME and cell heterogeneity within the tissue context (Jin et al., 2024). Such technologies combined with patient material and clinical data, generate a powerful tool in bridging the gap between fundamental cancer biology and clinical oncology, leading to

significant advancements in cancer diagnostics, treatment, and patient outcomes (Chakraborty et al., 2024).

Despite these and other advances, the mechanisms driving metastasis in EwS remain incompletely understood. Omics approaches, especially spatial and single-cell technologies, are helping to unravel the intra- and inter-tumor heterogeneity that complicates patient treatment (Chakraborty et al., 2024). Such technologies could be of remarkable use in EwS research, particularly given the fact that the main FET::ETS fusion driver of EwS is heterogeneously expressed within tumor tissue (Franzetti et al., 2017). For that purpose, the aim of this thesis was to fill the gap in the knowledge by exploiting the advancements in omics technologies to investigate EwS tumor heterogeneity, local invasiveness, and metastatic spread with a quest for clinically relevant molecular targets.

5.2. EWSR1::FLI1 drives spatially and transcriptionally different programs

As described earlier, spatial transcriptomic technologies have enabled us to study tumor heterogeneity at unprecedented level and unraveled functional roles of spatially close/distant regions. I hypothesized that by utilizing spatial transcriptomics in EwS patient samples, heterogeneity of *EWSR1::FLI1* expression could detected in a regional/zonal manner within the tumor mass.

Reports have shown that cancer cells at the leading edge are more invasive than cancer cells inside the tumor core (Yan et al., 2021). The leading edge (or invasive front) of a solid tumor is defined as the border region where the tumor mass directly interacts with the surrounding stroma, a zone critical for tumor-stroma communication and tumor progression (Ji et al., 2020; Mo et al., 2024). In addition, it has been reported that genes associated with worse outcome for tumor patients are part of the signature expressed in the leading tumor edge in comparison with the tumor core (Arora et al., 2023). Results of this thesis also support such hypothesis and show that indeed in EwS, the invasive tumor front also expresses signatures that are associated with worse patient outcome. Namely, the invasive front of a EwS patient sample that was spatial transcriptomic profiled was enriched for EWSR1::FLI1-low activity signature and higher *LMO7* expression, which are both associated with worse patient outcome and metastatic disease in EwS. This would support the initial hypothesis that EwS tumors do not have a random EWSR1::FLI1 expression heterogeneity, but that EWSR1::FLI1 expression shows a regional/zonal patterning with the tumor core being predominantly composed of

EWSR1::FLI1-high expressing cells while theinvasive front is enriched for EWSR1::FLI1-low expressing cells. In order to closer describe the EWSR1::FLI1-low activity signature only within EwS tumor cells I included several methods which defined tumorous from non-tumorous tissue (see Methods). In this way I was able to distinguish the cells in the tumor that have true EWSR1::FLI1-low activity signature, from adjacent non-tumorous tissue that has no fusion expression at all. Furthermore, it has been described in the literature that leading tumor edge has a unique set of molecular signatures and is enriched in genes related to EMT, MMPs, TGF-β, EGF and invasive immunosuppressive signaling (Arora et al., 2023; Bastola et al., 2020; Quail & Joyce, 2013; Wu et al., 2021). Also, gene expression profile of the leading edge is often conserved across different cancer types, reflecting common mechanisms of invasion, while the profile of the tumor core is more tissue-specific (Arora et al, 2023). Pathway spatial analysis of the EwS patient sample also revealed higher enrichment of TGF-β, TNFα and EGFR signaling in EWSR1::FLI1-low activity area.

Pathways expressed at invasive tumor front of EwS are related to cell movement, actin and integrin binding, immunosuppressive programs. Namely, TNFα, EGFR, TGFβ, JAK-STAT and NFκB pathways all regulate genes and proteins that control cell movement, including integrins, actin-binding proteins, and MMPs (Margadant & Sonnenberg, 2010; Misra et al., 2012; Wu & Zhou, 2010; Xue et al., 2023). In addition, TGF-β along with other chemokines, establishes an immunosuppressive microenvironment that promotes metastasis and tumor progression in EwS (Kumar et al., 2025).

Zonular expression of transcriptional programs would implicate possibility of dual anticancer treatment where tumors with such transcriptionally distinct programs would need at least two combined therapies for successful treatment. One that would target cells from the leading edge and one that is targeting tumor core. Indeed, *in silico* modeling in oral squamous cell carcinoma showed that drug response predictions differ between tumor core and leading edge, suggesting that these regions may require distinct therapeutic strategies (Arora et al., 2023). Hence, it is tempting to speculate that optimal effect in EwS would be gained in firstly applying the treatment targeting the leading edge with special focus on TGF-β, EMT and immune TME, after which targeted therapy for tumor core would be applied such as hypoxia-targeted agents, chemotherapy, or targeting cancer unique markers of more proliferative EwS cells. Such concept would then also be applicable to any solid malignancy that has spatially and transcriptionally distinct phenotypes. Targeting both zones can address the heterogeneity within tumors and reduce the risk of drug resistance. EWSR1::FLI1-low and high signatures

have been known as contributing factors in EwS tumorigenesis as well as being phenotypically and functionally distinct (Chaturvedi et al., 2012; Franzetti et al., 2017; Willis et al., 2013), but so far, have never been recognized as two spatially separate transcriptional programs. In order to confirm zonal expression pattern of EWSR1::ETS on a larger cohort of patients, future efforts should include spatial transcriptomic profiling of additional patient samples, ideally from both soft tissue and bone localized EwS which are recognized to have different impact on overall patient survival (Applebaum et al., 2011).

5.3. EWSR1::FLI1 regulation of metastasis relevant genes

The EWSR1::FLI1 fusion protein acts as an aberrant transcription factor (Jo, 2020) that has both activating and repressive functions in EwS cells that drive oncogenesis (Riggi et al, 2014). While research has mainly focused on EWSR1::FLI1 gene-activating (neo-enhancer) functions (Gangwal et al., 2008; Johnson et al., 2017; Orth et al., 2022), some studies have highlighted EWSR1::FLI1-repressive role that is also critical to the EwS tumor biology (Riggi et al., 2014; Sankar et al., 2013). EWSR1::FLI1 has both direct and indirect mechanisms of gene repression (Yasir et al., 2023). It can directly repress transcription by binding to canonical ETS motifs and displacing wild type ETS transcription factors from mesenchymal enhancers (Riggi et al., 2014). Some earlier described indirect mechanisms of gene repression involve the activation of transcriptional repressors like NKX2-2 (Owen et al., 2008) or recruiting repressive protein complexes (Tomazou et al., 2015).

On the example of *LMO7* it was shown that its expression in EwS cells in not regulated through direct EWSR1::ETS binding in the proximity of *LMO7* TSS. However, LMO7 had significant changes in expression dependent on EWSR1::FLI1 oscillations. LMO7 was enriched in a EWSR1::FLI1-low cell state, both at the RNA and protein level (**Figure 4.4**). But in two reanalyzed ChIP-seq datasets (Patel et al., 2012; Riggi et al., 2014) and HIChip data, there was no direct EWSR1::FLI1 binding signals in the vicinity of *LMO7* TSS, neither in the condition with/witout *EWSR1::FLI1* KD. Similar observations were also recorded when cloning ETS-core sites found in the proximity of *LMO7* TSS, upstream of luciferase gene and expressing it in the conditins with/witout *EWSR1::FLI1* KD (**Figure 4.5**). However, it has been described by Riggi et al. (2014) that EWSR1::FLI1 interacts with p300, a transcriptional coactivator with histone acetyltransferase activity that can epigenetically regulate gene expression through histone acetylation. They observed strong p300 signals in activated

EWSR1::FLI1 binding sites and dynamic changes in p300 occupancy that were closely coordinated with decreases in H3K27ac in activated sites and increases in H3K27ac at repressed sites upon depletion of the fusion (Riggi et al., 2014). This prompted me to investigate if *LMO7* is transcriptionally regulated through histone modifications, which have been shown on a large genome scale, as a common mechanism of regulation of EWSR1::FLI1-repressed genes (Riggi et al., 2014). Fusion binding sites are classified as repressed if EWSR1::FLI1 depletion results in increased H3K27ac and p300 signals, and those were also enriched for ETS motives. When re-analyzing the ChIP-seq datsets from Ebegboni et al. (2024), in the vicinity of *LMO7* TSS, there was an enrichment of H3K27ac upon *EWSR1::FLI1* KD. As well, proximity of *LMO7* TSS was enriched with ETS motives.This would chategorize *LMO7* as a EWSR1::FLI1-repressed gene. In sum, results of this thesis show that *LMO7* is not directly regulated by EWSR1::FLI1 binding in the vicinity of TSS, but rather suggest it is epigenetically regulated EWSR1::FLI1 target through histone acetylation.

Recent studies in EwS have shown that pharmacological inhibition of p300/CBP histone acetyltransferases reduces H3K27ac in EwS and could show effective results both *in vitro* and *in vivo* (Wei et al., 2024). Also, target genes of p300 in EwS have been linked to worse patient outcome (Wei et al., 2024). Thus if *LMO7* gene activation is regulated via p300 acetyltransferase activity and H3K27ac, then pharmacological inhibition of p300 would also reduce the expression of *LMO7* and cause a phenotypically similar effect to *LMO7* KD. Reanalysis of RNA-seq data from Wei et al. (2024) (GEO, SRA: PRJNA1161150), with special attention to *LMO7*, indicated significant downregulation of *LMO7* expression in all three tested EwS cell lines upon treatment with p300/CBP inhibitor (iP300w) and could be an indication of regulatory mechanism upstream of *LMO7* in EwS, that could be pharmacologically targeted. Future endeavors should include testing p300/CBP inhibitor on PDX models that have distinct *LMO7* expression levels (high vs. low) or on metastasis and localized EwS tumor derived PDXs to compare whether the efficiency of this drug is dependent on *LMO7* expression levels.

5.4. *LMO7* gene body methylation

Yet another epigenetic layer regulating *LMO7* expression in EwS is gene body DNA methylation. DNA methylation in promoters is well known to silence genes and is the therapeutic target of methylation inhibitors (Yang et al., 2014). In human genomes, Rauch et al. (2009) and Maunakea et al. (2010) first confirmed that methylated gene body regions

correlated with higher levels of gene transcription (Wang et al., 2022). Similarly, in cancer, gene body methylation is frequently associated with transcriptional activation, not silencing (Jjingo et al., 2012; Wang et al., 2022). Gene body methylation is important cellular mechanism because it can affect processes such as histone modification (Jeziorska et al., 2017), alternative splicing (Faustino & Cooper, 2003), and spurious transcription (Neri et al., 2017). In EwS, studies have mapped methylation patterns across the genome and discovered that EwS-specific hypermethylated CpG islands overlapped with developmental regulators of various lineages, including polycomb-repressed regions in pluripotent stem cells, AP-1 binding sites, and binding sites of various developmental transcription factors (Sheffield et al., 2017), though it was not clearly specified whether these changes included promoter regions exclusively or gene bodies as well. The results of this thesis show that several CpG islands within the *LMO7* gene body are significantly correlated with its higher expression in EwS patient samples. Additionally, there was one CpG in the proximity of *LMO7* TSS that was outside gene body but also associated with *LMO7* higher expression in a set of patient samples. This particular CpG island could serve a regulatory role and have similar function like the one earlier described in the literature of glioblastoma, where *LMO7* promoter methylation caused upregulation of *LMO7* expression (Oyinlade et al., 2018). It is also important to highlight that *LMO7* higher expression was also significantly associated with worse patient outcome and development of metastatic disease in EwS patients. Such results would indicate that methylation near the *LMO7* TSS as well as *LMO7* gene body methylation could be important for fueling the *LMO7*-related metastatic phenotype in EwS. Still, further comparative methylation studies done in healthy and EwS cells, as well as CRISPR-based tools to experimentally alter the methylation status (Vojta et al., 2016) would be need to fully elucidate this mechanism.

DNA methylation is a complex process, and usage of DNA methylation inhibiting agents in EwS can not only reduce promoter DNA methylation of silenced tumor suppressors like p53 and many others (Cristalli et al., 2022; Hossain & Ray, 2014; Ryland et al., 2016), but could also be used to reduce the methylation of gene bodies of genes like *LMO7*, that are have methylation associated with higher gene expression and are metastasis promoting genes in EwS. Studies performed in other cancers show that DNA methyltransferase (DNMT) inhibition tends to reverse EMT and inhibit tumor metastasis (Bu et al., 2018; Cui et al., 2018; Galle et al., 2020). In EwS such agents are currently in the research stage (Cristalli et al., 2022). Nevertheless, other genes relevant for the development of EwS might have different methylation patterns than what we know now, thus extensive research (also including gene

body methylation) should be done prior to further clinical applications of DNA methylation inhibiting agents in EwS.

5.5. EMT/MET plasticity and metastatic processes in EwS

In tumors, EMT is a cellular process in which cells lose their epithelial characteristics and acquire mesenchymal features (Pastushenko & Blanpain, 2019). EMT is a fundamental process for cancer progression, particularly metastasis (Allgayer et al., 2025). Cells undergoing EMT acquire mesenchymal traits such as increased motility, invasiveness, and resistance to apoptosis which are associated with aggressive tumor behavior and poor prognosis (Kong et al., 2011). In many tumors it is known that high EMT score has worse prognosis for the patient (Kahlert et al., 2017; Li et al., 2022; Xiao et al., 2022). EMT has long been viewed as a binary process with two distinct cell populations, epithelial and mesenchymal (Hay, 1995). It is often defined by the loss of the epithelial markers like E-cadherin, and gain of the mesenchymal markers expression like vimentin (Yamashita et al., 2018). However, recent research reveals that EMT occurs gradually through multiple cellular states. These states express varying degrees of epithelial and mesenchymal markers and can exibit intermediate morphological, transcriptional, and epigenetic characteristics. Such intermediate states, often termed hybrid or partial EMT, exist between fully epithelial and fully mesenchymal cell phenotypes (Nieto et al., 2016; Pastushenko et al., 2018). Hybrid epithelial/mesenchymal states have been identified as particularly tumorigenic and metastatic, with some evidence suggesting they may be even more aggressive than fully mesenchymal phenotypes (Chakraborty et al., 2020). Interestingly, cells exhibiting partial EMT were spatially localized at the leading edge of the tumor in the patient cohort of head and neck squamous cell carcinoma (Puram et al., 2017).

However, in sarcomas, hybrid epithelial/mesenchymal state might be the default state since those tumors normally express both epithelial and mesenchymal markers (Sannino et al., 2017), and especially pediatric and soft tissue sarcomas are among the most aggressive malignancies known (Damerell et al., 2021). Furthermore, in EwS there is a genetic fusion that might be fueling those hybrid epithelial/mesenchymal states even more, being itself heterogeneously expressed and influencing the shifts between more epithelial and more mesenchymal phenotypes (Silveira et al., 2023; Wiles et al., 2013). Here, I showed with the example of *LMO7*, a gene highly enriched in the more mesenchymal/migratory-like EWSR1::FLI1-low state (Franzetti et al., 2017), that *LMO7* is an important factor fueling EMT

and metastatic phenotype in EwS. Namely, *LMO7* KD caused significant downregulation of the EMT pathway at both the transcriptomic and proteomic level (**Figure 4.9**). EMT being the most downregulated pathway upon *LMO7* KD, could indicate that LMO7 is likely an important positive regulator of the EMT process in EwS. Such dual proteotranscriptomic decrease in EMT underscores that the effect is robust and not limited to post-transcriptional or post-translational regulation, suggesting that LMO7 acts either directly in the EMT network or in a critical upstream signaling pathway. Transcriptomic analysis of *LMO7* KD cells further highlighted significant downregulation of metalloproteinases (namely, *MMP1* and *MMP2*), which are one of the most important factors for the disassembly of the ECM and its constituents, are elevated in most cancer types, and are frequently associated with poor prognosis (Fares et al., 2020).

Integrative analysis of transcriptomic and proteomic datasets upon *LMO7* KD further highlighted TGF-β stimulated EMT as being most commonly downregulated, while oxidative phosphorylation pathways being most commonly upregulated. This could indicate that TGF-β signaling has a strong influence on EMT in EwS and that decrease of *LMO7* expression causes reduction of such signaling, as well as metabolic shift towards oxidative phosphorylation.

Firstly, TGF-β plays a dual and context-dependent role in normal tissues and tumors, where it maintains tumor suppressor effects in normal cells and early carcinomas, but its cytostatic effects are often lost during the progression of the disease and then it promotes EMT-driven progression and metastasis (Lebrun et al., 2012). TGF-β further supports cancer growth and progression by activating tumor angiogenesis and cancer-associated fibroblasts and enabling the tumor to evade inhibitory immune responses (Hao et al., 2019). Genes promoting EMT and TGF-β signaling often also suppress interferon responses and immune surveillance, facilitating immune escape and tumor progression via immunosuppressive tumor microenvironment, resistance to cytotoxic T cells and NK cells (Tseng et al., 2022). This would further also be supported with the results of both transcriptomic and proteomic analysis of *LMO7* KD in EwS cells, where upon *LMO7* KD, there was an increase in interferon α and γ signaling. Those results would strongly suggests that LMO7 plays a suppressive role on interferon-mediated immune responses and is a key mediator of immune evasion in EwS. Recent work from Daley et al. (2025), further supports this with findings in EwS TME being highly immunosuppressive due to the high TGF-β, low interferon, and low human leukocyte antigen (HLA) class I expression.

Proteomic analysis of LMO7 KD cells further suggested a significant downregulation of many non-canonical TGF-β branches (KEGG Medicus, MsigDB pathway analysis, **Supplementary figure 7.3**), like downregulation of signaling in c-Jun N-terminal kinase (JNK), ERK and Ras homolog family member A (RhoA), as well as downregulation of talin-vinculin signaling. To further support findings that LMO7 promotes EMT through mainly affecting non-canonical TGF-β signaling in EwS, future studies should aim to test canonical vs non-canonical separation (Clayton et al., 2020). Perform time-resolved western blots after TGF-β1 stimulation for p-Smad2/3 and p-Smad-independent arms (p-JNK, p-ERK, p-p38 and phosphorylated myosin phosphatase target subunit 1, p-MYPT1) (Sheikh et al., 2025) in EwS cells with/without *LMO7* KD. Additionally, reduced number of focal adhesions in confocal microscopy (anti-vinculin staining) upon *LMO7* KD, could further reflect disruptions in this mechanotransduction platform that connects mechanical force sensing with TGF-β non-canonical pathway activation driving metastasis and EMT progression (Xu et al., 2017).

Secondly, LMO7 causes a shift in EwS cell metabolism. EwS cells have significantly more glycolytic activity compared to their non-malignant counterparts (Dasgupta et al., 2017). The Warburg effect uses glycolysis as a source of energy, even in well-oxygenated environments (Hanahan & Weinberg, 2011), and enables cancer cells to avoid excess reactive oxygen species generation from mitochondrial respiration and thus gain increased anoikis resistance and survival advantage for metastasis (Lu et al, 2015). Enhanced glycolysis in tumors supports not only tumor growth but also invasion, metastasis, drug resistance, and immune evasion, through acidification it is impacting the TME, affecting stromal and immune cell function, and is recognized as a poor prognostic feature across multiple cancer types (Zhao et al., 2024; Zhou et al., 2022). In EwS, increased glycolysis and the Warburg effect is associated with increased cancer progression (Jiang et al., 2022). Also, high expression of glycolytic genes in EwS is associated with worse patient outcome (unpublished data from 196 EwS patient cohort, analyzed by a Master student of our lab, David Wolfhart). *LMO7* KD showed a significant reduction in glycolysis in transcriptomics and metabolic shift towards oxidative phosphorylation in proteomic analysis. Additionally, P300 earlier described in this thesis as likely upstream regulator of *LMO7* expression is one of the key transcriptional coactivator contributing EMT through various signaling pathways including TGF-β (Ko et al., 2013; Liao et al., 2013), Wnt/β-catenin (Inoue et al., 2016; Sun et al., 2000) and hypoxia inducible factor 1 subunit alpha (HIF-1α) (Shao et al., 2023). p300/CBP are essential coactivators that bind HIF-1α, which is necessary for HIF-1α-mediated transcription of

hypoxia-inducible genes. This includes about 30–50% of HIF-1α downstream targets responsible for responses to low oxygen, such as EMT and metabolic reprogramming (Luo & Wang, 2018). Thus, p300 alongside HIF-1α is involved in the transcriptional activation of glycolytic genes to shift cancer cells toward glycolysis (the Warburg effect), a metabolic phenotype that supports EMT and cancer metastasis (Zhang et al., 2021b). Upon *LMO7* KD, a likely downstream effector of p300/CBP in EwS, there was a reduction in glycolytic pathways, a metabolic shift towards oxidative metabolism and suppressed EMT. Nevertheless, the classic distinctions between glycolytic and oxidative tumors must be carefully reconsidered because hybrid phenotypes may confer more adaptable behaviors for soft tissue sarcoma cells (Miallot et al., 2021). To further follow up on previous discoveries, it would be desirable for future studies to preform a Seahorse experiments on EwS cells with/without *LMO7* KD to directly measure cellular metabolism, specifically the rates of oxygen consumption and extracellular acidification (Caines et al., 2022).

Lastly, both transcriptomic and proteomic analysis revealed significant influence of *LMO7* KD on mitotic spindle. This suggests that LMO7 supports both cell proliferation (via mitosis) and EMT-driven invasive phenotypes. Also, the role of LMO7 in cell division was earlier described in the literature, where overexpression of LMO7 caused a spindle assembly checkpoint defect (Tzeng et al., 2018). Here, IHC analysis of mouse xenograft tumors showed LMO7 staining colocalized with mitotic spindles in actively dividing cells, and confirmed decrease of mitotic cells upon *LMO7* KD in H&E staining.

The integrative approach employed in this thesis further highlighted the influence of LMO7 on ACTB, a key cytoskeleton protein, important in EwS fusion-low cells for cytoskeleton remodeling, invasion and metastasis (Chaturvedi et al., 2014; Franzetti et al., 2017; Katschnig et al., 2017). Previously mentioned, TGF-β-induced EMT, also involves extensive actin cytoskeleton reorganization. TGF-β signaling through both Smad-dependent and Smad-independent pathways induces the dissolution of epithelial structures, formation of actin stress fibers, increased cell motility, formation of invadopodia (Katsuno et al., 2013; Xu et al., 2009). IF imaging further strengthened the influence of LMO7 on cytoskeleton in EwS cells. Here, the colocalization area of LMO7 and filamentous actin (stained with phalloidin) was to great extent overlapping, and diminished upon *LMO7* KD (**Figure 4.10**). This provides direct spatial evidence that the LMO7 is associated with actin cytoskeleton structures. Such colocalization is typical for actin-binding proteins, adaptor proteins, cytoskeletal regulators, or signaling molecules that modulate or are modulated by actin dynamics (Haynes et al., 2011;

Nurmagambetova et al., 2023), and was also earlier described in the literature in the context of LMO7 interaction with F-actin network in other cell types (Du et al., 2019; Matsuda et al., 2022; Zhen et al., 2022).

In sum, those results would indicate that LMO7 is a critical positive regulator or mediator of the TGF-β-driven EMT pathways and cytoskeletal rearrangements in EwS. LMO7 corroborates interference with the cytoskeletal remodeling required for the mesenchymal transition, indicating an influence on of cell motility and metastatic potential. Altogether, this observations would align with phenotypical changes *in vitro* and *in vivo* upon *LMO7* KD, where it significantly influenced primary tumor growth and completely abrogated metastasis formation *in vivo*, supporting its importance in EwS tumorigenesis.

5.6. Limitations of the study and future perspective

This study was envisioned as one with translational cancer research potential. As such, it ideally serves for bridging the gap between fundamental cancer biology and clinical oncology, with strong potential to test research questions directly on patient derived data and facilitate the application of results toward future clinical practice (Luo et al., 2025). In order to use the most available source of patient tumor material, FFPE samples available from pathology archives (Patel et al., 2007) and for the purpose of analyzing them with spatial transcriptomic, a suitable method needed to be chosen. 10x Visium CytAssist enabled processing of FFPE samples available from the archival tumors. It allowed the analysis of gene expression across whole transcriptome, not limited to predefined panel of genes (Lim et al., 2025). However, transcripts in this method are assigned to a 55 μm^2 diameter, typically capturing transcripts from 1–10 cells (for EwS, this method captures ~5 cells/spot), giving relatively high spatial resolution for most tissue contexts (Zhu et al., 2023). Therefore the resolution is not truly single-cell, because each spot contains a composite signal, the total counts for each gene are a sum from the different cell types present in that location (Lim et al., 2025). Bioinformatics methods like deconvolution are a processing step to resolve cell type heterogeneity within each spot and recover near single-cell resolution information (Kleino et al., 2022). Reference-based deconvolution method uses single-cell RNA sequencing data from the similar source, ideally from the same patient or a closely matched cohort, as a reference to estimate the proportions of different cell types that would best explain the overall expression profile of a given spot (Wang et al., 2025). This reliance on single-cell transcriptomics references constrains the

spatial mapping of cell types to those in the reference (especially problematic is heterogeneity between patients), which may present limitations if there are missing cell types, mismatched cell types, perturbations, and batch effect differences between the single-cell transcriptomics reference and spatial transcriptomic data to be deconvolved (Miller et al., 2022).

Recently, several reference-free deconvolution methods emerged, that do not fully rely on the single cell data, while in practice, many researchers try both approaches or use reference-free methods initially and then refine results with single-cell references when such are available (Miller et al., 2022). However, single-cell RNA sequencing from the same patient tissue or similar cohort wasn't available and I opted for using the readout from few EwS cells localized in one spot to get insight in spatial expression patterns of genes of interest. Thus, I applied processing steps similar to what reference-free deconvolution method would do, but to determine the tumor border (separate tumor cells from tumor-adjacent tissue) which was important to define for my research question. For that purpose several steps for characterizing the tumor area have been utilized: number of transcript counts (tumor cells, especially aggressive tumors like EwS have several times higher global transcription rates than normal tissues (Zatzman et al., 2022)), tumor marker genes, in addition to histology defined tumor border to separate the tumorous from tumor adjacent tissue. It has been also known from the literature that defining the tumor border can be especially challenging in tumors with infiltrative growth patterns and that many tumors in pan-cancer studies have shown subtle or gradual transitions in gene expressions between tumor and adjacent non-tumor tissue that often result in intermediate or overlapping gene expression states (Aran et al., 2017). This can further blur the distinction in gene expression profiles in cell types and it becomes difficult or impossible for reference-free deconvolution methods to tell them apart. So, ideally the future efforts that would intend to study transcriptional programs in different cells of EwS TME, or interactions between EwS and tumor stroma should include single-cell scale resolution spatial transcriptomic methods like 10x Visium HD or Stereoseq (Lim et al., 2025). Additionally, in the future, if there is availability of such patient material, bearing in mind the rarity of EwS cases on 1 million people (Chakraborty et al., 2018), single-cell sequencing of primary, metastatic and circulating tumor cells from the same patient could be utilized to further elucidate the changes in EWSR1::ETS expression on the spatial and single-cell resolution scale during the progression of the disease. Furthermore, the research of this thesis revealed the importance of LMO7 for EwS invasion and metastasis, and in the previously suggested studies it would be attractive to explore possible differences in *LMO7* expression on the single-cell

resolution scale in named paired patient material. Such project design would enable deeper understanding of metastatic dissemination beyond EwS that is applicable to other, especially fusion-driven tumor entities.

Additionally, it would be interesting to observe if there are possible differences in LMO7 nuclear and cytoplasmic cellular roles (both in healthy and tumorous cells like EwS). According to previous results in EwS cells, LMO7 had both nuclear and cytoplasmic localization (**Figure 4.10**). The localization in EwS cells has been determined through IHC and IF staining, using different brands of antibodies and additionally using the method of cellular fractionation to rule out the non-specific staining. However, the limitation is that both brands of antibodies were polyclonal antibodies targeting the same epitope of LMO7 and were the only ones available on the market. Unfortnately, a third antibody tested, a mouse monoclonal antibody aginst LMO7 (B-7, #sc-376807, Santa Cruz), did not work in our hands. Also, cellular fractionation was yielding very low protein concentrations for cytoplasmic and whole-cell protein fraction since the used kit (Nuclear Extract Kit, Active Motif) was mainly designed for extraction of nuclear protein fraction. Still, dual localization of LMO7 has been already recognized in other cell types (Holaska et al., 2006; Possidonio et al., 2016) and also suggested due to the structure of its protein domain containing nuclear localization signal (Gomes et al., 2021). While LIM domain can have both nuclear and cytoplasmic roles in cells (Sala & Ampe. 2018), CH domain of LMO7 is responsible for actin binding in the cytoplasm (Du et al., 2019). Still, there are new studies emerging, that are showing the presence of actin also in the nucleus (Serebryannyy & de Lanerolle, 2020), although direct binding to nuclear actin via CH domain needs further investigation.

Such dual localization reflects that LMO7 is a multifunctional and possibly shuttle protein with roles in both cellular compartments. Additionally, LMO7 staining pattern was different depending on its location. In the nucleus, LMO7 had specular (punctate) and in the cytoplasm, fibrous staining pattern. Cytoplasmic fibrous staining and actin colocalization often denotes a role in actin filament organization and cytoskeletal remodeling, key for migration, invasion, and morphology in EMT (Haynes et al., 2011). Punctate nuclear pattern suggests regulation of gene expression, likely associated with transcriptional complexes (Davis et al., 2013), chromatin remodeling (Zaidi et al., 2005), participation in nuclear bodies (Shishido-Hara, 2010) or nuclear speckles (Voss & Wang, 2023). If those roles are cell type specific, or if and how they have an impact on various diseases in which LMO7 was earlier described (EDMD (Holaska et al., 2006), hearing loss (Du et al., 2019), pancreatic cancer (Liu et al.,

2012), breast cancer (Hu et al., 2011)) could be a focus for further investigations. For that purpose, one could generate LMO7 mutants, targeting the nuclear localization signal (Gomes et al., 2021; Notaro et al., 2021) and a mutant that won't be able to bind actin (Moriyama et al., 1992) requiring a mutation in CH domain of LMO7 (Du et al., 2019). Further, phenotypically characterize, as well as transcriptome and proteome profile the mutants in comparison to wildtype LMO7 to see which pathways/functions have been compromised upon introducing the mutations.

As already mentioned previously, LMO7 was described in many diseases beyond cancer, but to my knowledge, there are no drugs currently available that can target LMO7 directly. Thus, knowing the localization and consequences of mutating each protein domain are essential for directly pharmacologically targeting LMO7. Alternatively, an upstream or downstream protein of LMO7 pathway in EwS cells could be drug targeted to generate a phenotypic effect similar to *LMO7* KD. For that purpose, according to the previously provided evidence (**Figure 4.6d**), an inhibitor of p300/CBP was suggested, which is and upstream regulator of *LMO7* transcription. While p300/CBP inhibitor (iP300w) is effective in downregulating *LMO7* expression, has shown promise in EwS preclinical studies (Wei et al., 2024), and is being explored as a potential therapeutic, it has not yet progressed to clinical trials in humans. However, there is potential in other drugs targeting LMO7 downstream pathways like cytoskeleton disrupting drugs that may act on actin cytoskeleton depolymerization. Cytochalasin D can reduce cell size and F-actin content and reverse EMT by causing the loss of the mesenchymal markers in various metastatic cell lines (Jay Shankar & Nabi, 2015). Still, Cytochalasin D is not approved for clinical use and is primarily a research tool due to toxicity (Jay Shankar & Nabi, 2015). Additionally, there are other drugs like Celecoxib, that inhibited EwS cell migration via actin modulation (Behr et al., 2015), and is currently included in several clinical trials for other cancers (Tołoczko-Iwaniuk et al., 2019).

Finally, the discovery of *circLMO7* expression in EwS is tightly connected to the availability of parental gene *LMO7* transcript, thus could have prognostic value in EwS disease course and would make a promising candidate for non-invasive liquid biopsies, namely blood samples in suspected EwS patients. *circLMO7* has been found as part of exosomes in osteosarcoma (Luo et al., 2024) and is important for gastric cancer progression (Cao et al., 2021). However, the limitation of this project was that *circLMO7* has not been isolated directly from exosomes where circRNA is most abundant (Dou et al., 2016) but from xenograft tumor tissue that included tumor cells and surrounding stromal components. Isolating circRNA

exclusively from exosomes would be a direct proof of communication between the tumor, its surrounding and distal organs. Still, bodily fluids for isolating exosomes, like blood from mice models where tumors were growing, are very low in volume (usually 100-200 µL per sample, to avoid harming the mouse or affecting its physiology) and would thus yield extremely low RNA concentrations. And EwS patient blood samples were not available for this study. Additionally, there might be limitations of background noise if there is endogenous mice circRNA that could complicate signal detection. Thus, future endeavors could consider *circLMO7* and/or *LMO7* expression profiling in exosomes and CTCs from EwS patients' blood. CTCs and exosomes are the key for transitioning and preparing tumor microenvironment for local invasion and metastatic spread (Shi et al., 2024), and if there is a marker of such process, it would enable capturing metastatic dissemination in an earlier time point and in a non-invasive way. Better stratification of patients at diagnosis would indicate better treatment options and higher rates of survival.

6. CONCLUSION

Metastasis is the leading cause of cancer related death, and in sarcomas, this is no different (Nandra et al., 2015). Despite many advances in multi-omics technologies and translational cancer research, the mechanisms driving metastasis in EwS remain incompletely understood. Single-cell and spatial technologies are of remarkable use in EwS research because of their ability to dissect the expressional heterogeneity of the FET::ETS fusion (Franzetti et al., 2017), the main driver of EwS tumorigenesis (Flores & Grohar, 2021). Using spatial transcriptomic profiling of EwS patient tumor, this study elucidated that EWSR1::ETS-high and -low cells have zonal expression within the tumor mass, showing spatially and transcriptionally distinct programs. The EwS tumor core has a predominantly EWSR1::FLI1-high activity signature, while the invasive front (leading edge) of the tumor has a predominantly EWSR1::FLI1-low activity signature. Thus, the invasive front contains more migratory and metastatic-like cells, that are considered to be important for EwS metastatic spread (Franzetti et al., 2017). Analysis of genes enriched in EWSR1::FLI1-low cells showed high expression of the clinically relevant gene *LMO7*, which is significantly associated with worse overall patient survival and development of metastatic disease in a larger EwS patient cohort (n = 196). Integration of the data from two EwS studies (Aynaud et al., 2020; Orth et al., 2022) as well as functional experiments in cell lines with Dox-inducible *EWSR1::ETS* KD, resulted in finding that EWSR1::ETS is having a repressive effect on LMO7. Additionally, re-analysis of ChIP-seq data from Ebegboni et al. (2024) indicated that *LMO7* expression could be epigenetically regulated through presence of activating H3K27ac marks only in the condition of *EWSR1::FLI1* KD. This axis, regulating *LMO7* expression, has the potential to be pharmacologically exploited utilizing inhibitor of histone acetyltransferase complex p300/CBP (iP300w), that has previously shown effective results both *in vitro* and *in vivo* in EwS cells (Wei et al., 2024), and also showed significant downregulation of *LMO7* expression in comparison with untreated cells.

Integrative transcriptome and proteome profiling of EwS cells upon *LMO7* KD, highlighted LMO7 as an important factor associated with EMT and cytoskeleton remodeling in EwS cells. Among the commonly and significantly downregulated genes and proteins upon *LMO7* KD was ACTB. Additionaly, IF imaging in EwS cells displayed colocalization of LMO7 and F-actin, further emphasizing the impact of LMO7 on actin remodeling. Moreover, transcriptomic and proteomic pathway analysis showed that *LMO7* KD also reduced the

immunosuppressive TME and metabolic shift towards glycolytic metabolic activity which are known to be associated with increased cancer progression in EwS (Jiang et al., 2022). Functional experiments proved that *LMO7* KD decreases the capacity of EwS cells for clonogenic growth and migration *in vitro*. Additionally, *LMO7* KD significantly slowed down primary tumor growth, and caused complete absence of metastasis *in vivo*. These findings underscore the potential of LMO7 as a prognostic biomarker for better stratification of EwS patients at diagnosis, while there is also potential for therapeutic targeting of p300-LMO7-actin axis that could limit tumor growth and prevent metastasis, improving clinical outcomes of EwS patients (**Figure 6.1**).

In sum, these results identify LMO7 as clinically relevant key downstream target of FET::ETS fusions in EwS, and provide an example of how the integration of functional, spatial, and clinical data can shed light on mechanisms by which local invasiveness contributes to metastatic dissemination in cancer.

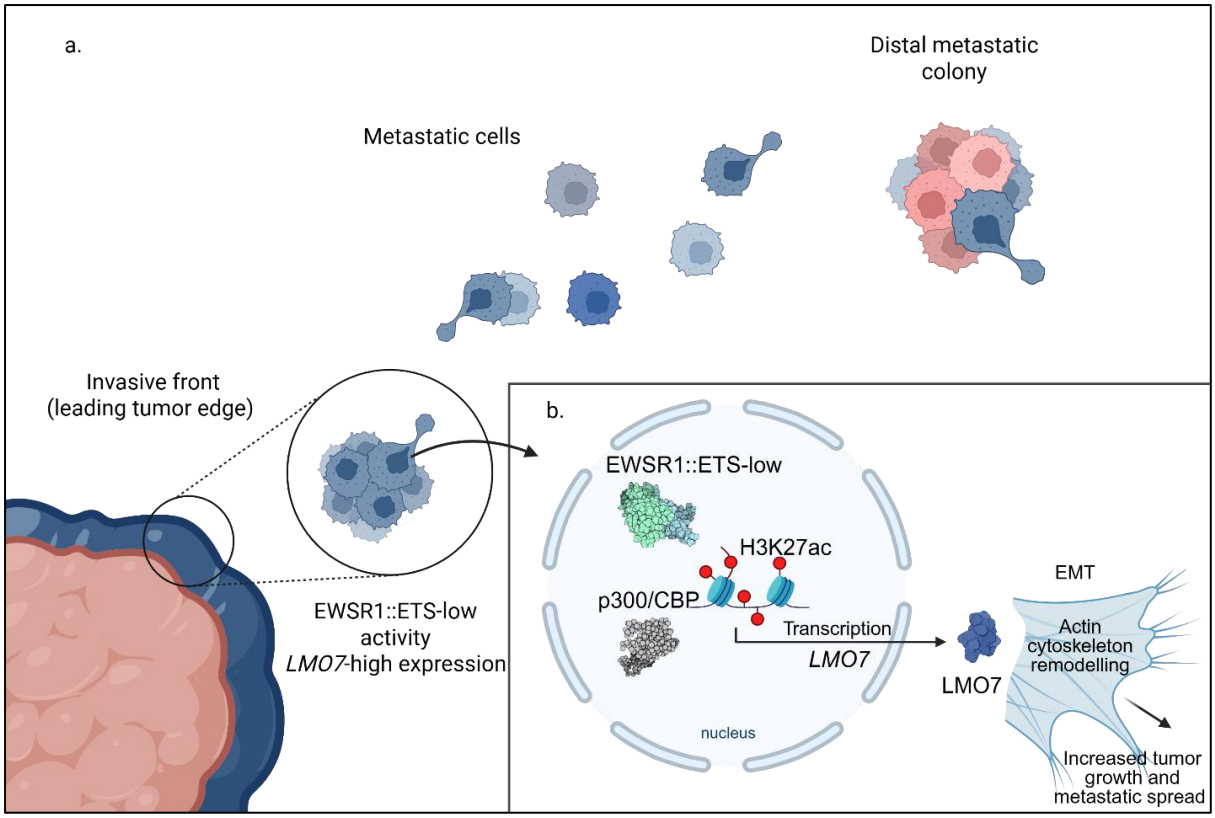

Figure 6.1. Schematic representation of the proposed role of LMO7 on EwS local invasiveness and metastatic spread. a. Localized EwS tumor has spatially and transcriptionally distinct programs fueling primary tumor growth and metastatic spread. Signatures enriched in tumor invasive front are EWSR1::FLI1-low activity and *LMO7*-high expression, both associated with worse patient outcome in EwS patient cohort (n = 196). **b.** In the cells with EWSR1::FLI1-low activity, histone acetyltransferase complex p300/CBP causes transfer of activating H3K27ac marks in the proximity of *LMO7* TSS and enhances *LMO7* transcription. Then, LMO7 enhances EMT transcriptional programs in EwS cells, colocalizes with F-actin and impacts actin cytoskeleton remodeling. Such changes in the cells of leading tumor edge are supportive of local tumor invasiveness and metastatic spread and are mirrored in phenotypic assays *in vitro* and *in vivo*.

7. SUPPLEMENTARY INFORMATION

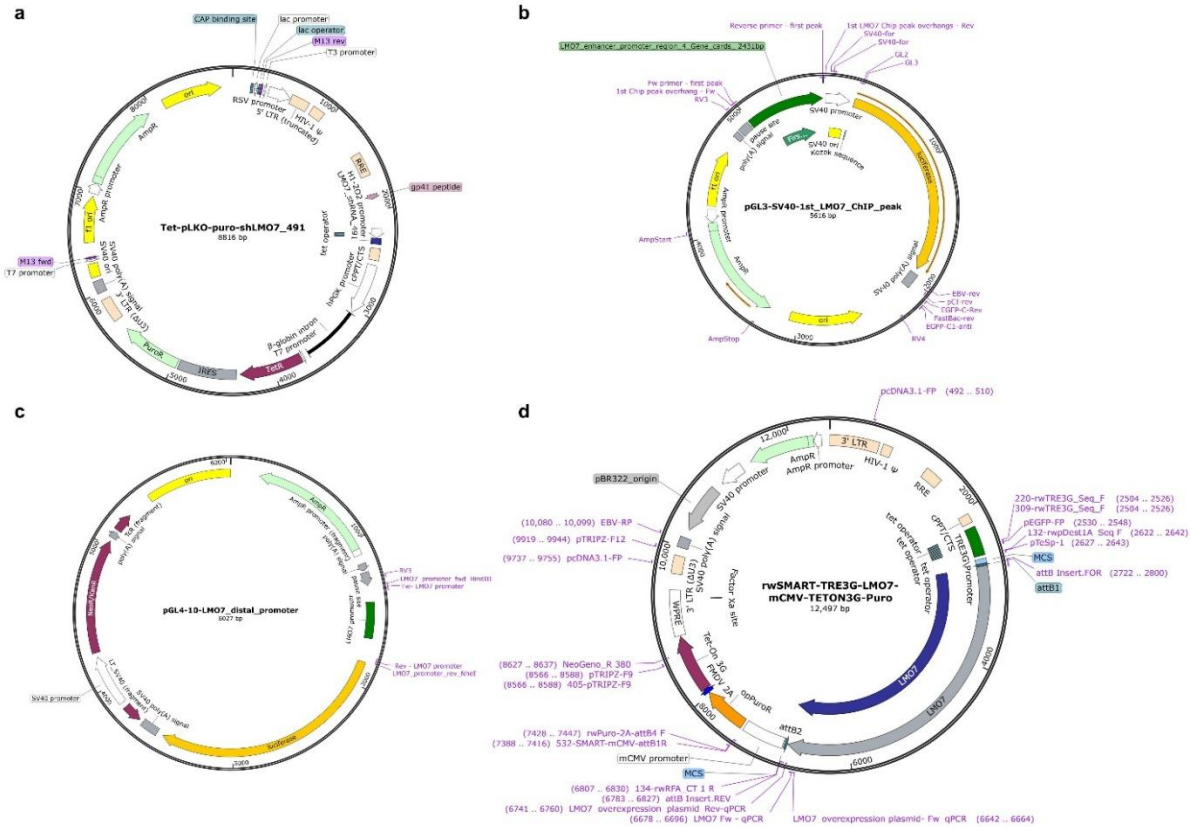

Supplementary figure 7.1 Representative plasmid maps of cloned constructs. All *in silico* cloning and plasmid maps of this thesis were generated in SnapGene (version 7.2.1). **a.** Tet-pLKO-puro (Addgene, #21915) with integrated shRNA sequence targeting *LMO7*. Here shown sequence (indicated in blue) was cloned in the plasmid using shLMO7_491 primers (Table 3.1) and restriction enzymes AgeI-HF and EcoRI-HF. **b.** pGL3-Fluc (Promega, #E1761) with integrated DNA fragment that contains the 1st ChIP-seq FLI binding peak (indicated in R2 browser as hg19, chr13: 76,195,324–76,195,697). Here shown sequence (indicated in dark green) was cloned in the plasmid using NEBuilder HiFi DNA assembly protocol and primers with overhangs indicated in the table Table 3.1. Same protocol was used for cloning of 2nd ChIP-seq FLI peak (indicated in R2 browser as hg19, chr13: 76,340,783–76,341,217), primers in Table 3.1. **c.** pGL4-10 (Promega, #9PIE665) with integrated fragment that contains the distal *LMO7* promoter (hg19 coordinates: chr13: 76,140,731–76,140,978). Here shown sequence (indicated in dark green) was cloned in the plasmid using NEBuilder HiFi DNA assembly protocol and primers with overhangs indicated in the table Table 3.1. **d.** rwSMART-TRE3G_LMO7-mCMV-TETON3G-Puro plasmid with integrated *LMO7* transcript variant 1 (NM_005358.5) indicated in blue, generated with the help of the Cellular Tools Core Facility (DKFZ, Heidelberg).

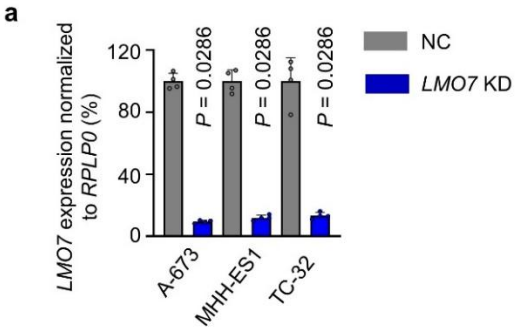

Supplementary figure 7.2 RT-qPCR validation of *LMO7* expression upon 55 h siPOOL treatment in RNA samples for Affymetrix transcriptome profiling. *LMO7* expression normalized to housekeeping gene *RPLP0*. Analysis done in 3 EwS cell lines: A-673, MHH-ES1 and TC-32. n = 4 biologically independent experiments. Horizontal bars represent the mean and whiskers the SD. Two-tailed Mann-Whitney test.

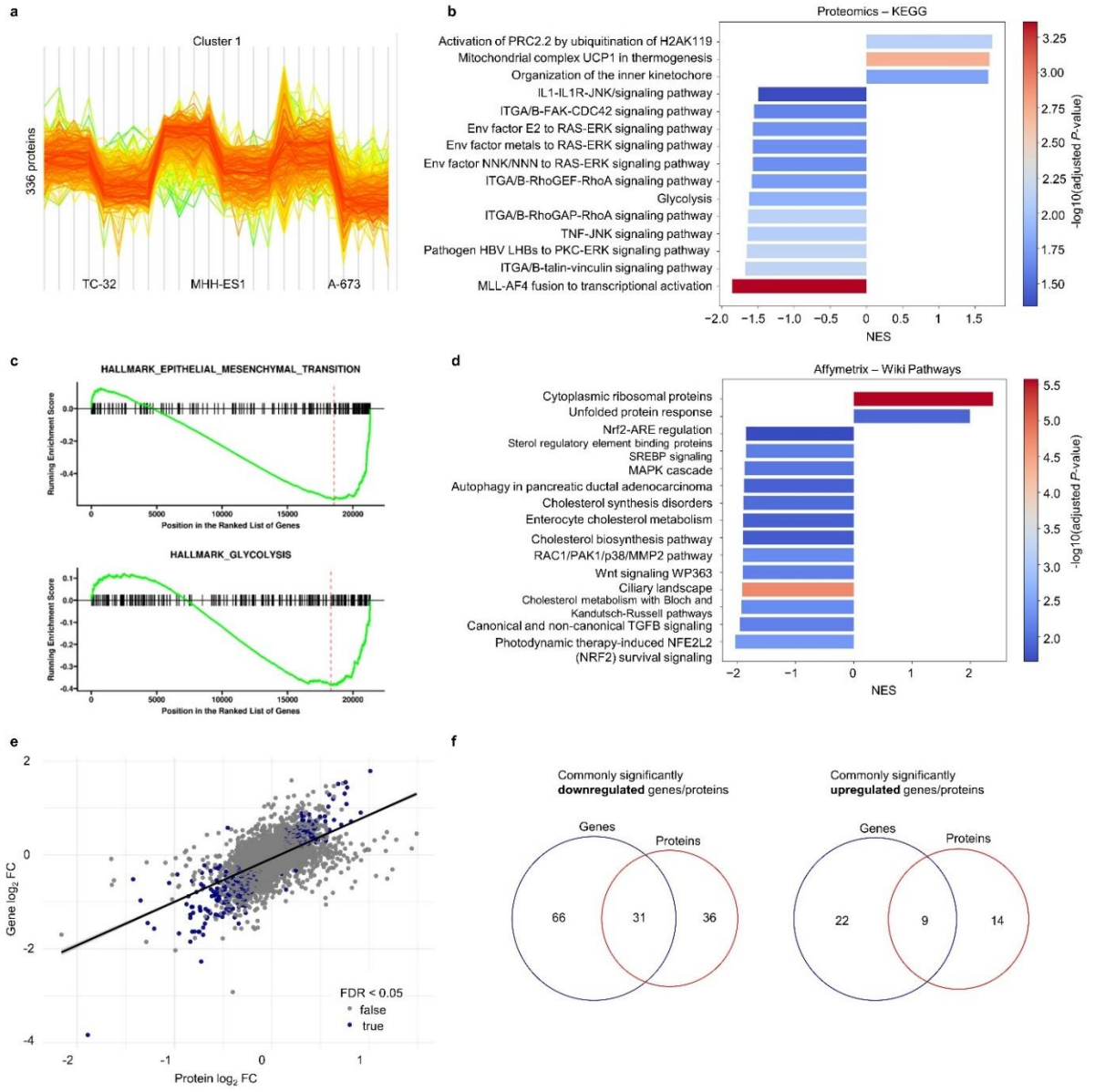

Suplementary figure 7.3 Integrated transcriptomics and proteomics of LMO7 downstream pathways. a. Cluster profile plot of Cluster 1, from of proteomic analysis in two conditions (NC and LMO7 KD) in three EwS cell lines (A-673, MHH-ES-1 and TC-32). Oscilations in protein expressions in this cluster correspond to n = 336 proteins. **b.** Most significantly differentially expressed pathways from proteomic analysis in two conditions (NC and LMO7 KD) in three EwS cell lines (A-673, MHH-ES-1 and TC-32) from curated gene sets KEGG Medicus (MSigDB). Red represents higher and blue represents lower $-\log_{10}$ adjusted *P*-value. $|\text{NES}| > 1.5$, $P_{adj} < 0.05$. **c.** A GSEA enrichment plot of EMT and glycolysis pathways from curated gene sets (Hallmark, MSigDB) of transcriptomic analysis upon *LMO7* KD in three EwS cell lines (A-673, MHH-ES-1 and TC-32) displaying a running enrichment score (green) of a given gene set over the ranked gene list. The black vertical lines indicate the specific genes from the Hallmark set that appear at different positions in the ranked gene list and a red dashed line indicating the location of maximum enrichment score. **d.** Most significantly differentially expressed pathways from transcriptomic analysis in two conditions (NC and *LMO7* KD) in three EwS cell lines (A-673, MHH-ES-1 and TC-32) from curated gene sets WikiPathways (MSigDB). Red represents higher and blue represents lower $-\log_{10}$ adjusted *P*-value. $|\text{NES}| > 1.5$, $P_{adj} < 0.05$. **e.** Correlation plot between gene and protein expression from commonly expressed genes and proteins in

transcriptomic and proteomic analysis (n = 6,438) in two conditions (NC and LMO7 KD) in three EwS cell lines (A-673, MHH-ES-1 and TC-32). Filtered retained commonly expressed genes/proteins from limma analyses were utilized for producing the correlation plot. Person's r = 0.594, $P < 0.0001$. **f.** Venn diagrams showing commonly significantly downregulated (left panel) and upregulated (right panel) genes/proteins in both datasets, $|\log_2 FC| > 1$ for genes, $|\log_2 FC| > 0.5$ for proteins, $P_{adj} < 0.05$ for both. For more clarity, genes/proteins from the interception of Venn diagrams are shown in **Supplementary table 7.5**.

Supplementary Table 7.1 Initial filtering and integration of transcriptomics ESCLA data (Orth et al., 2022) and 196 EwS patient cohort data. Most DEGs in 5 EwS ESCLA cell lines (A-673, MHH-ES-1, SK-N-MC, TC-71 and TC-106) with EWSR1::FLI1/ERG KD (FC > 2.5) and significance of each gene for EwS patient survival 196 EwS patient cohort.

Gene ID	Gene name	DEG in 5 EwS cell lines with EWSR1::ETS KD (FC > 2.5) ESCLA, (Orth et al., 2022.)	SD	Significance for EwS patient survival (n = 196) *P*-value	Best percentile group size (%)	Significance
4015	*LOX*	5.022	3.416	0.044	79	low gene expression
4907	*NT5E*	4.548	3.709	0.305	75	low gene expression
133	*ADM*	4.106	3.188	0.138	24	high gene expression
3488	*IGFBP5*	3.979	2.376	0.045	77	high gene expression
3490	*IGFBP7*	3.966	2.789	0.05	35	low gene expression
5806	*PTX3*	3.955	5.482	0.082	21	high gene expression
22943	*DKK1*	3.907	5.720	0.125	79	low gene expression
57522	*SRGAP1*	3.452	1.720	0.102	64	high gene expression
5228	*PGF*	3.369	1.693	0.185	57	low gene expression
633	*BGN*	3.347	2.788	0.44	77	high gene expression
27063	*ANKRD1*	3.344	4.580	0.224	64	low gene expression
10252	*SPRY1*	3.266	3.264	0.048	31	high gene expression
1281	*COL3A1*	3.249	1.081	0.062	48	low gene expression
1410	*CRYAB*	3.204	3.722	0.000285	20	high gene expression
5122	*PCSK1*	3.169	3.173	0.585	78	high gene expression
5054	*SERPINE1*	3.139	3.480	0.165	24	low gene expression
22822	*PHLDA1*	3.117	3.103	0.063	43	low gene expression
55691	*FRMD4A*	3.101	1.356	0.267	77	low gene expression
51050	*PI15*	3.017	3.777	0.016	58	low gene expression
5328	*PLAU*	2.995	3.752	0.15	35	low gene expression
27303	*RBMS3*	2.993	0.971	0.152	22	low gene expression
649	*BMP1*	2.992	1.810	0.027	80	low gene expression
51200	*CPA4*	2.975	4.445	0.062	80	low gene expression
4256	*MGP*	2.916	3.155	0.029	30	high gene expression
2200	*FBN1*	2.890	2.939	0.088	73	high gene expression
4008	*LMO7*	2.870	1.624	0.005	22	low gene expression
4811	*NID1*	2.827	1.851	0.074	63	high gene expression
3371	*TNC*	2.760	1.112	0.232	63	high gene expression
22795	*NID2*	2.697	1.599	0.026	54	low gene expression
2012	*EMP1*	2.696	2.167	0.502	80	high gene expression
30846	*EHD2*	2.636	1.614	0.163	23	high gene expression
3491	*CYR61*	2.629	2.826	0.006	25	low gene expression
4016	*LOXL1*	2.593	1.630	0.078	40	low gene expression
10079	*ATP9A*	2.589	1.810	0.933	20	low gene expression
4897	*NRCAM*	2.588	1.707	0.131	59	low gene expression
10608	*MXD4*	2.572	1.119	0.000385	21	high gene expression
9411	*ARHGAP29*	2.569	3.528	0.041	25	high gene expression
84159	*ARID5B*	2.562	0.905	0.002	79	high gene expression
9052	*GPRC5A*	2.548	3.393	0.166	35	low gene expression
7057	*THBS1*	2.523	3.171	0.077	20	low gene expression

Supplementary table 7.2 Pearson's correlation of spatial gene expression and EWSR1::ETS-high and -low activity signature imputed from Orth et al. (2022). Shown values are for those gene candidates that passed previous filtering steps in bioinformatics pipeline, and are calculated considering candidate's gene expression only within defined tumor borders in the EwS patient sample.

Gene ID	Gene name	Person's correlation	*P*-value	P_{adj}	Pearson's correlation	*P*-value	P_{adj}
		High EWSR1::FLI1 score			Low EWSR1::FLI1 score		
4008	*LMO7*	−0.525	1.47E-193	8.83E-193	0.383	2.76E-96	1.10E-95
4015	*LOX*	−0.330	2.52E-70	7.57E-70	0.375	4.50E-92	1.35E-91
22795	*NID2*	−0.278	9.41E-50	2.26E-49	0.330	3.90E-70	9.37E-70
649	*BMP1*	−0.206	1.81E-27	2.71E-27	0.241	2.32E-37	3.10E-37
51050	*PI15*	0.267	1.32E-45	2.27E-45	-0.146	1.87E-14	2.24E-14

Supplementary table 7.3 Output from the differential expression analysis (limma) of Affymetrix data. Most differentially expressed genes from transcriptomic analysis in two conditions (NC and LMO7 KD) in three EwS cell lines (A-673, MHH-ES-1 and TC-32), |FC | > 1.3.

Gene	logFC	AvgExpr	*P*-value	P_{adj}
LMO7	-3.834	9.486	6.405E-23	1.326E-18
SYT11	-2.920	11.687	5.538E-13	1.431E-10
MMP2	-2.501	10.465	1.243E-22	1.326E-18
BGN	-2.360	11.047	1.233E-12	2.987E-10
PFKP	-2.271	14.338	7.926E-15	5.452E-12
MAP3K12	-2.186	8.220	1.979E-15	1.919E-12
GJA1	-2.032	12.311	4.278E-18	1.825E-14
FABP3	-1.961	5.459	4.869E-08	1.909E-06
ELK3	-1.896	9.494	1.501E-11	2.354E-09
NEK7	-1.851	11.130	1.149E-18	6.123E-15
RCN2	-1.847	13.382	6.795E-18	2.415E-14
SFXN3	-1.780	8.496	1.424E-13	4.744E-11
GFRA2	-1.769	9.779	6.827E-16	8.088E-13
LMAN1	-1.702	14.879	1.976E-13	6.194E-11
RPS6KC1	-1.698	8.623	7.911E-14	3.183E-11
SNX27	-1.672	13.459	1.800E-17	4.799E-14
MFAP4	-1.671	13.203	6.024E-16	7.557E-13
ACTB	-1.637	12.863	3.442E-11	4.993E-09
NFU1	-1.637	10.484	8.429E-16	8.988E-13
ACSL4	-1.635	9.390	7.658E-16	8.595E-13
MOCS2	-1.631	10.838	5.906E-12	1.145E-09
TMEM64	-1.627	9.296	2.105E-10	2.088E-08
RASSF8	-1.606	9.924	1.172E-14	7.351E-12
FAM73A	-1.600	9.143	1.592E-13	5.143E-11
ARPC1B	-1.576	10.412	1.118E-13	4.090E-11
ATXN7L3B	-1.570	9.587	1.079E-16	1.913E-13
MCL1	-1.569	13.855	1.875E-14	9.752E-12
NAV1	-1.559	12.116	2.443E-15	2.265E-12
PADI2	-1.548	9.615	2.004E-13	6.194E-11
MCFD2	-1.547	12.086	1.132E-13	4.090E-11
DENND6A	-1.541	10.800	2.249E-16	3.426E-13
EIF5A2	-1.532	10.591	1.187E-17	3.617E-14
LOX	-1.522	8.046	7.699E-12	1.398E-09
AZIN1	-1.515	13.570	2.061E-17	4.883E-14
RAB11FIP2	-1.473	9.437	1.184E-13	4.140E-11
TNFRSF12A	-1.464	11.801	2.731E-12	6.131E-10
CALM1	-1.462	16.218	4.942E-16	6.586E-13
CASP7	-1.461	10.703	3.143E-14	1.426E-11
PLEKHA3	-1.449	11.376	4.895E-16	6.586E-13
DCLRE1A	-1.431	11.262	1.054E-09	7.441E-08
TGFBI	-1.427	9.291	8.865E-08	3.217E-06
TRIM37	-1.407	9.601	1.166E-16	1.913E-13

NT5E	-1.404	10.264	3.879E-09	2.230E-07
CA5B	-1.386	9.715	1.388E-15	1.409E-12
RGS7BP	-1.383	7.750	2.004E-09	1.266E-07
LRP8	-1.376	9.228	3.715E-12	7.617E-10
DDAH1	-1.370	12.719	1.124E-11	1.915E-09
RAB8B	-1.350	10.691	7.336E-14	3.008E-11
LRRC58	-1.348	12.046	3.732E-15	2.932E-12
IL1RAP	-1.339	13.742	2.353E-14	1.103E-11
TCF4	-1.337	13.599	2.480E-17	5.288E-14
TMOD3	-1.328	13.468	3.815E-13	1.043E-10
N4BP2	-1.328	10.105	5.779E-12	1.141E-09
SGOL2	-1.322	10.125	1.127E-11	1.915E-09
ARHGEF40	-1.320	6.998	9.152E-11	1.049E-08
LZIC	-1.319	11.806	8.196E-15	5.462E-12
CPD	-1.312	9.109	6.885E-12	1.299E-09
ABHD3	-1.305	8.376	2.199E-13	6.699E-11
SYTL5	-1.301	9.362	8.407E-11	9.796E-09
-				
CNN2	1.306	13.430	3.245E-06	6.524E-05
CD24	1.309	6.479	2.291E-06	4.955E-05
SLC2A3	1.332	10.925	3.965E-14	1.725E-11
AMBN	1.338	7.819	2.589E-08	1.131E-06
EPHA4	1.345	11.740	4.193E-14	1.788E-11
RNF122	1.362	8.433	1.975E-10	1.981E-08
PSAT1	1.437	15.878	4.005E-13	1.081E-10
F11R	1.464	8.313	1.428E-10	1.522E-08
MYD88	1.466	9.881	2.174E-08	9.687E-07
SCAMP1	1.513	10.237	2.427E-13	7.289E-11
OCLN	1.527	12.588	5.996E-09	3.204E-07
C12orf73	1.528	8.147	1.215E-10	1.357E-08
NARF	1.548	11.627	8.572E-10	6.301E-08
NEB	1.588	12.079	2.784E-09	1.677E-07
LOC647859	1.606	12.896	3.156E-09	1.869E-07
DKK1	1.723	7.413	1.737E-08	8.017E-07
SLITRK6	1.779	7.414	2.000E-08	9.037E-07
ARL6IP1	1.787	14.242	2.147E-14	1.063E-11
STK40	1.831	11.232	2.192E-14	1.063E-11
TXNIP	3.414	8.696	3.032E-20	2.155E-16

Supplementary table 7.4 Output from the differential expression analysis (limma) of proteomics data. Most differentially expressed proteins from proteomic analysis in two conditions (NC and LMO7 KD) in three EwS cell lines (A-673, MHH-ES-1 and TC-32), |FC | > 1.

Protein	logFC	AvgExpr	*P*-value	P_{adj}
RPS6KC1	-2.162	17.137	1.205E-02	1.204E-01
LMO7	-1.891	16.442	3.867E-08	1.093E-05
CTSS	-1.649	16.693	5.421E-02	2.953E-01
KIAA0232	-1.644	16.510	6.889E-02	3.353E-01
GTF2A1	-1.622	15.959	5.727E-03	7.637E-02
SETD1B	-1.425	16.115	2.850E-03	4.675E-02
C18orf32	-1.348	16.279	1.075E-03	2.483E-02
NEK7	-1.290	17.549	2.680E-02	1.936E-01
MCUR1	-1.286	16.973	7.210E-02	3.440E-01
PLEKHA3	-1.275	15.561	1.261E-03	2.761E-02
ASH1L	-1.233	15.931	3.835E-03	5.727E-02
ATXN7L3B	-1.209	16.890	7.759E-07	1.037E-04
YIPF4	-1.093	17.116	1.631E-02	1.444E-01
GOLT1B	-1.054	15.968	1.408E-03	2.965E-02
TBC1D9	-1.024	15.942	1.116E-02	1.144E-01
LATS1	-1.020	17.422	4.967E-03	6.841E-02
-				
TMEM120B	1.002	20.063	1.076E-01	4.282E-01
DMAC1	1.012	17.466	1.437E-01	4.950E-01
ARL6IP1	1.013	18.652	4.244E-08	1.155E-05
TMA7	1.057	16.104	2.549E-01	6.414E-01
RET	1.073	15.674	1.426E-01	4.942E-01
KRT18	1.153	17.300	2.195E-01	5.984E-01
VKORC1	1.173	17.559	2.446E-02	1.841E-01
RNF10	1.184	17.754	1.499E-02	1.365E-01
AIFM2	1.188	20.045	2.181E-01	5.967E-01
MAN2A2	1.241	17.535	1.159E-01	4.452E-01
GULP1	1.280	15.407	2.607E-02	1.908E-01
HMGXB3	1.439	16.915	1.322E-01	4.785E-01
RECQL5	1.489	18.540	1.459E-01	4.992E-01

Supplementary table 7.5 Most significantly concordantntly up- or downregulated genes and their proteins covered in both transcriptomic and proteomic datsets. Interesection of Venn diagrams listed in the table for clarity. Integrated analysis of transcriptomic and proteomic datasets performed in two conditions (NC and LMO7 KD), in three EwS cell lines (A-673, MHH-ES-1 and TC-32). Significantly concordantly differentially downregulated or upregulated genes and proteins, |log2FC| > 1 for genes, |log2FC| > 0.5 for proteins, Padj < 0.05 for both.

Gene and Protein	Common category
CAB39	Upregulated
NAB1	Upregulated
CUX1	Upregulated
HCCS	Upregulated
CNN2	Upregulated
PSAT1	Upregulated
SCAMP1	Upregulated
NARF	Upregulated
ARL6IP1	Upregulated
LMO7	Downregulated
PFKP	Downregulated
RCN2	Downregulated
LMAN1	Downregulated
SNX27	Downregulated
ACTB	Downregulated
NFU1	Downregulated
ACSL4	Downregulated
MOCS2	Downregulated
ATXN7L3B	Downregulated
MCFD2	Downregulated
CASP7	Downregulated
PLEKHA3	Downregulated
RAB8B	Downregulated
IL1RAP	Downregulated
N4BP2	Downregulated
LZIC	Downregulated
TRIM2	Downregulated
ETNK1	Downregulated
THUMPD1	Downregulated
PALM3	Downregulated

8. LITERATURE

Adane, B., Alexe, G., Seong, B. K. A., Lu, D., Hwang, E. E., Hnisz, D., ... & Stegmaier, K. (2021). STAG2 loss rewires oncogenic and developmental programs to promote metastasis in Ewing sarcoma. *Cancer cell*, *39*(6), 827-844.

Allgayer, H., Mahapatra, S., Mishra, B., Swain, B., Saha, S., Khanra, S., ... & Kundu, G. C. (2025). Epithelial-to-mesenchymal transition (EMT) and cancer metastasis: the status quo of methods and experimental models 2025. *Molecular Cancer*, *24*(1), 167.

Alter, J., Rozentzweig, D., & Bengal, E. (2008). Inhibition of myoblast differentiation by tumor necrosis factor α is mediated by c-Jun N-terminal kinase 1 and leukemia inhibitory factor. *Journal of Biological Chemistry*, *283*(34), 23224-23234.

Annalora, A. J., O'Neil, S., Bushman, J. D., Summerton, J. E., Marcus, C. B., & Iversen, P. L. (2018). A k-mer based transcriptomics approach for antisense drug discovery targeting the Ewing's family of tumors. *Oncotarget*, *9*(55), 30568.

Antonescu, C. R., & Dal Cin, P. (2014). Promiscuous genes involved in recurrent chromosomal translocations in soft tissue tumours. *Pathology*, *46*(2), 105-112.

Apfelbaum, A. A., Wrenn, E. D., & Lawlor, E. R. (2022). The importance of fusion protein activity in Ewing sarcoma and the cell intrinsic and extrinsic factors that regulate it: A review. *Frontiers in oncology*, *12*, 1044707.

Applebaum, M. A., Worch, J., Matthay, K. K., Goldsby, R., Neuhaus, J., West, D. C., & DuBois, S. G. (2011). Clinical features and outcomes in patients with extraskeletal Ewing sarcoma. *Cancer*, *117*(13), 3027-3032.

Aran, D., Camarda, R., Odegaard, J., Paik, H., Oskotsky, B., Krings, G., ... & Butte, A. J. (2017). Comprehensive analysis of normal adjacent to tumor transcriptomes. *Nature communications*, *8*(1), 1077.

Arora, R., Cao, C., Kumar, M., Sinha, S., Chanda, A., McNeil, R., ... & Bose, P. (2023). Spatial transcriptomics reveals distinct and conserved tumor core and edge architectures that predict survival and targeted therapy response. *Nature communications*, *14*(1), 5029.

Aynaud, M. M., Mirabeau, O., Gruel, N., Grossetête, S., Boeva, V., Durand, S., ... & Zinovyev, A. (2020). Transcriptional programs define intratumoral heterogeneity of Ewing sarcoma at single-cell resolution. *Cell reports*, *30*(6), 1767-1779.

Badia-i-Mompel, P., Vélez Santiago, J., Braunger, J., Geiss, C., Dimitrov, D., Müller-Dott, S., ... & Saez-Rodriguez, J. (2022). decoupleR: ensemble of computational methods to infer biological activities from omics data. *Bioinformatics advances*, *2*(1), vbac016.

Bakkar, N., Wang, J., Ladner, K. J., Wang, H., Dahlman, J. M., Carathers, M., ... & Guttridge, D. C. (2008). IKK/NF-κB regulates skeletal myogenesis via a signaling switch to inhibit differentiation and promote mitochondrial biogenesis. *Journal of Cell Biology*, *180*(4), 787-802.

Baldauf, M. C., Orth, M. F., Dallmayer, M., Marchetto, A., Gerke, J. S., Rubio, R. A., ... & Grünewald, T. G. (2017). Robust diagnosis of Ewing sarcoma by immunohistochemical detection of super-enhancer-driven EWSR1-ETS targets. *Oncotarget*, *9*(2), 1587.

Bastola, S., Pavlyukov, M. S., Yamashita, D., Ghosh, S., Cho, H., Kagaya, N., ... & Nakano, I. (2020). Glioma-initiating cells at tumor edge gain signals from tumor core cells to promote their malignancy. *Nature communications*, *11*(1), 4660.

Beauchamp, E., Bulut, G., Abaan, O., Chen, K., Merchant, A., Matsui, W., ... & Üren, A. (2009). GLI1 is a direct transcriptional target of EWS-FLI1 oncoprotein. *Journal of Biological Chemistry*, *284*(14), 9074-9082.

Behr, C. A., Hesketh, A. J., Barlow, M., Glick, R. D., Symons, M., Steinberg, B. M., & Soffer, S. Z. (2015). Celecoxib inhibits Ewing sarcoma cell migration via actin modulation. *Journal of Surgical Research*, *198*(2), 424-433.

Bierbaumer, L., Katschnig, A. M., Radic-Sarikas, B., Kauer, M. O., Petro, J. A., Högler, S., ... & Kovar, H. (2021). YAP/TAZ inhibition reduces metastatic potential of Ewing sarcoma cells. *Oncogenesis*, *10*(1), 2.

Biermann, J. S., Hirbe, A., Ahlawat, S., Bernthal, N. M., Binitie, O., Boles, S., ... & Lyons, M. (2025). Bone Cancer, Version 2.2025, NCCN Clinical Practice Guidelines In Oncology. *Journal of the National Comprehensive Cancer Network*, *23*(4).

Boone, M. A., Taslim, C., Crow, J. C., Selich-Anderson, J., Byrum, A. K., Showpnil, I. A., ... & Lessnick, S. L. (2021b). The FLI portion of EWS/FLI contributes a transcriptional regulatory function that is distinct and separable from its DNA-binding function in Ewing sarcoma. *Oncogene*, *40*(29), 4759-4769.

Boone, M. A., Taslim, C., Crow, J. C., Selich-Anderson, J., Watson, M., Heppner, P., ... & Winstanley, M. (2021a). Identification of a novel FUS/ETV4 fusion and comparative analysis with other Ewing sarcoma fusion proteins. *Molecular Cancer Research*, *19*(11), 1795-1801.

Bosma, S. E., Ayu, O., Fiocco, M., Gelderblom, H., & Dijkstra, P. D. S. (2018). Prognostic factors for survival in Ewing sarcoma: a systematic review. *Surgical oncology*, *27*(4), 603-610.

Brohl, A. S., Solomon, D. A., Chang, W., Wang, J., Song, Y., Sindiri, S., ... & Khan, J. (2014). The genomic landscape of the Ewing Sarcoma family of tumors reveals recurrent STAG2 mutation. *PLoS genetics*, *10*(7), e1004475.

Bu, X., Zhang, X., Xu, J., Yang, H., Zhou, X., Wang, H., & Gong, L. (2018). Inhibition of DNA methyltransferase 1 by RNA interference reverses epithelial-mesenchymal transition in highly metastatic 95D lung cancer cells by inhibiting the Wnt signaling pathway. *Oncology Letters*, *15*(6), 9242-9250.

Bull, E. C., Singh, A., Harden, A. M., Soanes, K., Habash, H., Toracchio, L., ... & Green, D. (2025). Targeting metastasis in paediatric bone sarcomas. *Molecular Cancer*, *24*, 153.

Caines, J. K., Barnes, D. A., & Berry, M. D. (2022). The use of seahorse XF assays to interrogate real-time energy metabolism in cancer cell lines. In *Cancer Cell Biology: Methods and Protocols* (pp. 225-234). New York, NY: Springer US.

Cao, B., Sun, H., Fan, Z., Khawar, M. B., Cai, L., Yu, S., ... & Sun, H. (2023). Integrative analyses of bulk microarray data to discover genes, pathways, and immune infiltration characteristics associated with targeting of Ewing sarcoma. *Journal of Cancer Research and Clinical Oncology*, *149*(10), 6967-6977.

Cao, J., Zhang, X., Xu, P., Wang, H., Wang, S., Zhang, L., ... & Xu, Z. (2021). Circular RNA circLMO7 acts as a microRNA-30a-3p sponge to promote gastric cancer progression via the WNT2/β-catenin pathway. *Journal of Experimental & Clinical Cancer Research*, *40*(1), 6.

Celià-Terrassa, T., & Kang, Y. (2016). Distinctive properties of metastasis-initiating cells. *Genes & development*, *30*(8), 892-908.

Chakraborty, P., George, J. T., Tripathi, S., Levine, H., & Jolly, M. K. (2020). Comparative study of transcriptomics-based scoring metrics for the epithelial-hybrid-mesenchymal spectrum. *Frontiers in bioengineering and biotechnology*, *8*, 220.

Chakraborty, S., Sharma, G., Karmakar, S., & Banerjee, S. (2024). Multi-OMICS approaches in cancer biology: New era in cancer therapy. *Biochimica et Biophysica Acta (BBA)-Molecular Basis of Disease*, *1870*(5), 167120.

Chaturvedi, A., Hoffman, L. M., Jensen, C. C., Lin, Y. C., Grossmann, A. H., Randall, R. L., ... & Beckerle, M. C. (2014). Molecular dissection of the mechanism by which EWS/FLI expression compromises actin cytoskeletal integrity and cell adhesion in Ewing sarcoma. *Molecular biology of the cell*, *25*(18), 2695-2709.

Chaturvedi, A., Hoffman, L. M., Welm, A. L., Lessnick, S. L., & Beckerle, M. C. (2012). The EWS/FLI oncogene drives changes in cellular morphology, adhesion, and migration in Ewing sarcoma. *Genes & cancer*, *3*(2), 102-116.

Chavan, M., Dhakal, S., Singh, A., Rai, V., Arora, S., Mallipeddi, M. C., & Das, A. (2023). Ewing sarcoma genomics and recent therapeutic advancements. *Pediatric Hematology Oncology Journal*, *8*(1), 50-65.

Chicón-Bosch, M., Sánchez-Serra, S., Rosàs-Lapeña, M., Costa-Fraga, N., Besalú-Velázquez, J., Illa-Bernadí, J., ... & Tirado, Ò. M. (2025). Multi-omics profiling reveals key factors involved in Ewing sarcoma metastasis. *Molecular oncology*, *19*(4), 1002-1028.

Choi, E. Y. K., Gardner, J. M., Lucas, D. R., McHugh, J. B., & Patel, R. M. (2014, January). Ewing sarcoma. In *Seminars in diagnostic pathology* (Vol. 31, No. 1, pp. 39-47). WB Saunders.

Clayton, S. W., Ban, G. I., Liu, C., & Serra, R. (2020). Canonical and noncanonical TGF-β signaling regulate fibrous tissue differentiation in the axial skeleton. *Scientific Reports*, *10*(1), 21364.

Cripe, T. P. (2011). Ewing sarcoma: an eponym window to history. *Sarcoma*, *2011*(1), 457532.

Cristalli, C., Manara, M. C., Valente, S., Pellegrini, E., Bavelloni, A., De Feo, A., ... & Scotlandi, K. (2022). Novel targeting of DNA methyltransferase activity inhibits Ewing sarcoma cell proliferation and enhances tumor cell sensitivity to DNA damaging drugs by activating the DNA damage response. *Frontiers in endocrinology*, *13*, 876602.

Cui, H., Hu, Y., Guo, D., Zhang, A., Gu, Y., Zhang, S., ... & Fan, H. (2018). DNA methyltransferase 3A isoform b contributes to repressing E-cadherin through cooperation of DNA methylation and H3K27/H3K9 methylation in EMT-related metastasis of gastric cancer. *Oncogene*, *37*(32), 4358-4371.

Dai, X., Theobard, R., Cheng, H., Xing, M., & Zhang, J. (2018). Fusion genes: A promising tool combating against cancer. *Biochimica et Biophysica Acta (BBA)-Reviews on Cancer*, *1869*(2), 149-160.

Daley, J. D., Mukherjee, E., Ferraro, D., Bhaskar, S., Green, A., Meyer, E. M., ... & Bailey, K. M. (2025). SARC028 Samples Reveal an Interplay between TGF-β, IFN Signaling, and Low HLA Class I Expression as Contributors to Ewing Sarcoma Checkpoint Blockade Resistance. *Clinical Cancer Research*, *31*(17), 3805-3816.

Damerell, V., Pepper, M. S., & Prince, S. (2021). Molecular mechanisms underpinning sarcomas and implications for current and future therapy. *Signal transduction and targeted therapy*, *6*(1), 246.

Dasgupta, A., Kurenbekova, L., Patel, T. D., Rajapakshe, K., Ghosal, G., Nirala, B., ... & Yustein, J. (2023). Modeling Ewing sarcoma lung metastasis. *Current protocols*, *3*(2), e670.

Dasgupta, A., Trucco, M., Rainusso, N., Bernardi, R. J., Shuck, R., Kurenbekova, L., ... & Yustein, J. T. (2017). Metabolic modulation of Ewing sarcoma cells inhibits tumor growth and stem cell properties. *Oncotarget*, *8*(44), 77292.

Davis, J. R., Mossalam, M., & Lim, C. S. (2013). Controlled access of p53 to the nucleus regulates its proteasomal degradation by MDM2. *Molecular pharmaceutics*, *10*(4), 1340-1349.

Dedeic, Z., Cetera, M., Cohen, T. V., & Holaska, J. M. (2011). Emerin inhibits Lmo7 binding to the Pax3 and MyoD promoters and expression of myoblast proliferation genes. *Journal of cell science*, *124*(10), 1691-1702.

Dehner, C. A., Warmke, L. M., Umphress, B., Malik, F., Cloutier, J. M., Dermawan, J. K., ... & Folpe, A. L. (2025). Superficial Neurocristic FET:: ETS Fusion Tumor: Expanding the Clinicopathological and Molecular Genetic Spectrum of a Recently Described Entity. *Modern Pathology*, *38*(2), 100656.

Delattre, O., Zucman, J., Plougastel, B., Desmaze, C., Melot, T., Peter, M., Kovar, H., Joubert, I., De Jong, P., Rouleau, G. and Aurias, A., 1992. Gene fusion with an ETS DNA-binding domain caused by chromosome translocation in human tumours. *Nature*, *359*(6391), pp.162-165.

Deng, Z., Fan, T., Xiao, C., Tian, H., Zheng, Y., Li, C., & He, J. (2024). TGF-β signaling in health, disease and therapeutics. *Signal transduction and targeted therapy*, *9*(1), 61.

Dimitrov, D., Schäfer, P. S. L., Farr, E., Rodriguez-Mier, P., Lobentanzer, S., Badia-i-Mompel, P., ... & Saez-Rodriguez, J. (2024). LIANA+ provides an all-in-one framework for cell–cell communication inference. *Nature Cell Biology*, *26*(9), 1613-1622.

Dou, Y., Cha, D. J., Franklin, J. L., Higginbotham, J. N., Jeppesen, D. K., Weaver, A. M., ... & Zhang, B. (2016). Circular RNAs are down-regulated in KRAS mutant colon cancer cells and can be transferred to exosomes. *Scientific reports*, *6*(1), 37982.

Du, T. T., Dewey, J. B., Wagner, E. L., Cui, R., Heo, J., Park, J. J., ... & Shin, J. B. (2019). LMO7 deficiency reveals the significance of the cuticular plate for hearing function. *Nature communications*, *10*(1), 1117.

Dupuy, M., Lamoureux, F., Mullard, M., Postec, A., Regnier, L., Baud'huin, M., ... & Verrecchia, F. (2023). Ewing sarcoma from molecular biology to the clinic. *Frontiers in Cell and Developmental Biology*, *11*, 1248753.

Durer, S., Gasalberti, D. P., & Shaikh, H. (2024). Ewing sarcoma. In *StatPearls [Internet]*. StatPearls Publishing.

Ebegboni, V. J., Jones, T. L., Brownmiller, T., Zhao, P. X., Pehrsson, E. C., Sundara Rajan, S., & Caplen, N. J. (2024). ETS1, a target gene of the EWSR1:: FLI1 fusion oncoprotein, regulates the expression of the focal adhesion protein TENSIN3. *Molecular Cancer Research*, *22*(7), 625-641.

Evdokimova, V., Gassmann, H., Radvanyi, L., & Burdach, S. E. (2022). Current state of immunotherapy and mechanisms of immune evasion in ewing sarcoma and osteosarcoma. *Cancers*, *15*(1), 272.

Ewing, J. (1921). Diffuse endothelioma of bone. *Proc New York Path*, *21*, 17-24.

Fares, J., Fares, M. Y., Khachfe, H. H., Salhab, H. A., & Fares, Y. (2020). Molecular principles of metastasis: a hallmark of cancer revisited. *Signal transduction and targeted therapy*, *5*(1), 28.

Faustino, N. A., & Cooper, T. A. (2003). Pre-mRNA splicing and human disease. *Genes & development*, *17*(4), 419-437.

Flores, G., & Grohar, P. J. (2021). One oncogene, several vulnerabilities: EWS/FLI targeted therapies for Ewing sarcoma. *Journal of bone oncology*, *31*, 100404.

France, K. A., Anderson, J. L., Park, A., & Denny, C. T. (2011). Oncogenic fusion protein EWS/FLI1 down-regulates gene expression by both transcriptional and posttranscriptional mechanisms. *Journal of Biological Chemistry*, *286*(26), 22750-22757.

Franzetti, G. A., Laud-Duval, K., Van Der Ent, W., Brisac, A., Irondelle, M., Aubert, S., ... & Delattre, O. (2017). Cell-to-cell heterogeneity of EWSR1-FLI1 activity determines proliferation/migration choices in Ewing sarcoma cells. *Oncogene*, *36*(25), 3505-3514.

Funk, C. M., & Musa, J. (2020). Proliferation assessment by trypan blue exclusion in ewing sarcoma. In *Ewing Sarcoma: Methods and Protocols* (pp. 151-158). New York, NY: Springer US.

Gajdzis, P., Pierron, G., & Klijanienko, J. (2022). Cytology of undifferentiated round-cell sarcomas of bone and soft tissue: Ewing sarcoma or not Ewing sarcoma, that is the question. *Acta Cytologica*, *66*(4), 295-306.

Galle, E., Thienpont, B., Cappuyns, S., Venken, T., Busschaert, P., Van Haele, M., ... & Lambrechts, D. (2020). DNA methylation-driven EMT is a common mechanism of resistance to various therapeutic agents in cancer. *Clinical epigenetics*, *12*(1), 27.

Gangwal, K., Sankar, S., Hollenhorst, P. C., Kinsey, M., Haroldsen, S. C., Shah, A. A., ... & Lessnick, S. L. (2008). Microsatellites as EWS/FLI response elements in Ewing's sarcoma. *Proceedings of the National Academy of Sciences*, *105*(29), 10149-10154.

Gaspar, N., Hawkins, D. S., Dirksen, U., Lewis, I. J., Ferrari, S., Le Deley, M. C., ... & Oberlin, O. (2015). Ewing sarcoma: current management and future approaches through collaboration. *Journal of Clinical Oncology*, *33*(27), 3036-3046.

Giménez-Llorente, D., Cuadrado, A., Andreu, M. J., Sanclemente-Alamán, I., Solé-Ferran, M., Rodríguez-Corsino, M., & Losada, A. (2024). STAG2 loss in Ewing sarcoma alters enhancer-promoter contacts dependent and independent of EWS:: FLI1. *EMBO reports*, *25*(12), 5537-5560.

Ginsberg, J. P., de Alava, E., Ladanyi, M., Wexler, L. H., Kovar, H., Paulussen, M., ... & Barr, F. G. (1999). EWS-FLI1 and EWS-ERG gene fusions are associated with similar clinical phenotypes in Ewing's sarcoma. *Journal of Clinical Oncology*, *17*(6), 1809-1809.

Girardi, F., Taleb, A., Ebrahimi, M., Datye, A., Gamage, D. G., Peccate, C., ... & Le Grand, F. (2021). TGFβ signaling curbs cell fusion and muscle regeneration. *Nature communications*, *12*(1), 750.

Gomes, G., do Amaral, M. J., Bagri, K. M., Vasconcellos, L. M., Almeida, M. D. S., Alvares, L. E., & Mermelstein, C. (2021). New findings on LMO7 transcripts, proteins and regulatory regions in human and vertebrate model organisms and the intracellular distribution in skeletal muscle cells. *International journal of molecular sciences*, *22*(23), 12885.

Goodspeed, A., Bodlak, A., Duffy, A. B., Nelson-Taylor, S., Oike, N., Porfilio, T., ... & Hayashi, M. (2025). Single-Cell RNA Sequencing of Ewing Sarcoma Tumors Demonstrates Transcriptional Heterogeneity and Clonal Evolution. *Clinical Cancer Research*, *31*(10), 2010-2023.

Grünewald, T. G., Cidre-Aranaz, F., Surdez, D., Tomazou, E. M., de Álava, E., Kovar, H., ... & Dirksen, U. (2018). Ewing sarcoma. *Nature reviews Disease primers, 4*(1), 5.

Guo, L., & Teng, L. (2015). YAP/TAZ for cancer therapy: opportunities and challenges. *International journal of oncology*, *46*(4), 1444-1452.

Hahm, K. B., Cho, K., Lee, C., Im, Y. H., Chang, J., Choi, S. G., ... & Kim, S. J. (1999). Repression of the gene encoding the TGF-β type II receptor is a major target of the EWS-FLI1 oncoprotein. *Nature genetics*, *23*(2), 222-227.

Hanahan, D., & Weinberg, R. A. (2011). Hallmarks of cancer: the next generation. *cell*, *144*(5), 646-674.

Hao, Y., Baker, D., & Ten Dijke, P. (2019). TGF-β-mediated epithelial-mesenchymal transition and cancer metastasis. *International journal of molecular sciences*, *20*(11), 2767.

Hawkins, A. G., Pedersen, E. A., Treichel, S., Temprine, K., Sperring, C., Read, J. A., ... & Lawlor, E. R. (2020). Wnt/β-catenin–activated Ewing sarcoma cells promote the angiogenic switch. *JCI insight*, *5*(13), e135188.

Hay, E. D. (1995). An overview of epithelio-mesenchymal transformation. *Cells Tissues Organs*, *154*(1), 8-20.

Haynes, J., Srivastava, J., Madson, N., Wittmann, T., & Barber, D. L. (2011). Dynamic actin remodeling during epithelial–mesenchymal transition depends on increased moesin expression. *Molecular biology of the cell*, *22*(24), 4750-4764.

He, C. B., Pham, D., Kronenfeld, R. S., Rosenberg, A., Ardente, J., & Dhir, A. (2025). The Importance of Next-Generation Sequencing in Identifying Immunohistochemically Ambiguous Pediatric Sarcomas. *Case reports in oncological medicine*, *2025*(1), 9926653.

He, S., Huang, Q., Hu, J., Li, L., Xiao, Y., Yu, H., ... & Xiao, J. (2019). EWS-FLI1-mediated tenascin-C expression promotes tumour progression by targeting MALAT1 through integrin α5β1-mediated YAP activation in Ewing sarcoma. *British journal of cancer*, *121*(11), 922-933.

Heitzeneder, S., Sotillo, E., Shern, J. F., Sindiri, S., Xu, P., Jones, R., ... & Mackall, C. L. (2019). Pregnancy-associated plasma protein-A (PAPP-A) in Ewing sarcoma: role in tumor growth and immune evasion. *JNCI: Journal of the National Cancer Institute*, *111*(9), 970-982.

Hinton, K., Kirk, A., Paul, P., & Persad, S. (2023). Regulation of the epithelial to mesenchymal transition in osteosarcoma. *Biomolecules*, *13*(2), 398.

Holaska, J. M., Rais-Bahrami, S., & Wilson, K. L. (2006). Lmo7 is an emerin-binding protein that regulates the transcription of emerin and many other muscle-relevant genes. *Human molecular genetics*, *15*(23), 3459-3472.

Hölting, T. L., & Knott, M. M. (2020). Analysis of regulatory DNA sequences by dual-luciferase reporter assays in ewing sarcoma. In *Ewing Sarcoma: Methods and Protocols* (pp. 139-149). New York, NY: Springer US.

Hossain, M. M., & Ray, S. K. (2014). Ews knockdown and taxifolin treatment induced differentiation and removed DNA methylation from p53 promoter to promote expression of puma and noxa for apoptosis in ewing's sarcoma. *Journal of cancer therapy*, *5*(12), 1092.

Inoue, H., Takahashi, H., Hashimura, M., Eshima, K., Akiya, M., Matsumoto, T., & Saegusa, M. (2016). Cooperation of Sox4 with β-catenin/p300 complex in transcriptional regulation of the Slug gene during divergent sarcomatous differentiation in uterine carcinosarcoma. *BMC cancer*, *16*(1), 53.

Jayavelu, A. K., Schnöder, T. M., Perner, F., Herzog, C., Meiler, A., Krishnamoorthy, G., ... & Heidel, F. H. (2020). Splicing factor YBX1 mediates persistence of JAK2-mutated neoplasms. *Nature*, *588*(7836), 157-163.

Jeyaraman, N., Jeyaraman, M., Subramanian, P., Ramasubramanian, S., Balaji, S., Muthu, S., ... & Gangadaran, P. (2025). Advancements in bone malignancy research through next-generation sequencing focussed on osteosarcoma, chondrosarcoma, and Ewing sarcoma. *Pathology-Research and Practice*, 155908.

Jeziorska, D. M., Murray, R. J., De Gobbi, M., Gaentzsch, R., Garrick, D., Ayyub, H., ... & Tufarelli, C. (2017). DNA methylation of intragenic CpG islands depends on their transcriptional activity during differentiation and disease. *Proceedings of the National Academy of Sciences*, *114*(36), E7526-E7535.

Ji, A. L., Rubin, A. J., Thrane, K., Jiang, S., Reynolds, D. L., Meyers, R. M., ... & Khavari, P. A. (2020). Multimodal analysis of composition and spatial architecture in human squamous cell carcinoma. *cell*, *182*(2), 497-514.

Jiang, X., Chen, Z., Zhu, J., Han, J., You, G., Li, Y., ... & Ye, H. (2022). E2F1 promotes Warburg effect and cancer progression via upregulating ENO2 expression in Ewing sarcoma. *Molecular Medicine Reports*, *26*(1), 237.

Jin, Y., Zuo, Y., Li, G., Liu, W., Pan, Y., Fan, T., ... & Peng, Y. (2024). Advances in spatial transcriptomics and its applications in cancer research. *Molecular Cancer*, *23*(1), 129.

Jjingo, D., Conley, A. B., Soojin, V. Y., Lunyak, V. V., & Jordan, I. K. (2012). On the presence and role of human gene-body DNA methylation. *Oncotarget*, *3*(4), 462.

Jo, V. Y. (2020). EWSR1 fusions: Ewing sarcoma and beyond. *Cancer Cytopathology*, *128*(4), 229-231.

Johnson, K. M., Taslim, C., Saund, R. S., & Lessnick, S. L. (2017). Identification of two types of GGAA-microsatellites and their roles in EWS/FLI binding and gene regulation in Ewing sarcoma. *PloS one*, *12*(11), e0186275.

Kadin, M. E., & Bensch, K. G. (1971). On the origin of Ewing's tumor. *Cancer*, *27*(2), 257-273.

Kahlert, U. D., Joseph, J. V., & Kruyt, F. A. (2017). EMT-and MET-related processes in nonepithelial tumors: importance for disease progression, prognosis, and therapeutic opportunities. *Molecular oncology*, *11*(7), 860-877.

Kashima, T. G., Gamage, N. G., Dirksen, U., Gibbons, C. L., Ostlere, S. J., & Athanasou, N. A. (2013). Localized Ewing sarcoma of the tibia. *Clinical sarcoma research*, *3*, 1-6.

Katschnig, A. M., Kauer, M. O., Schwentner, R., Tomazou, E. M., Mutz, C. N., Linder, M., ... & Kovar, H. (2017). EWS-FLI1 perturbs MRTFB/YAP-1/TEAD target gene regulation inhibiting cytoskeletal autoregulatory feedback in Ewing sarcoma. *Oncogene*, *36*(43), 5995-6005.

Katsuno, Y., Lamouille, S., & Derynck, R. (2013). TGF-β signaling and epithelial–mesenchymal transition in cancer progression. *Current opinion in oncology*, *25*(1), 76-84.

Kim, J. A., Crawford, K. A., Spada, P. A., Martin, L. R., Zhang, J., Wong, R., ... & Keller, C. (2023). Non-chemotherapy adjuvant agents in TP53 mutant Ewing sarcoma. *Scientific reports*, *13*(1), 14360.

Kim, M. J., Febbraro, D., Farkona, S., Gillmore, T., Son, J. E., Regeenes, R., ... & Woo, M. (2021). Distinct roles of UVRAG and EGFR signaling in skeletal muscle homeostasis. *Molecular Metabolism*, *47*, 101185.

Kleino, I., Frolovaitė, P., Suomi, T., & Elo, L. L. (2022). Computational solutions for spatial transcriptomics. *Computational and structural biotechnology journal*, *20*, 4870-4884.

Ko, H., So, Y., Jeon, H., Jeong, M. H., Choi, H. K., Ryu, S. H., ... & Choi, K. C. (2013). TGF-β1-induced epithelial–mesenchymal transition and acetylation of Smad2 and Smad3 are negatively regulated by EGCG in human A549 lung cancer cells. *Cancer letters*, *335*(1), 205-213.

Kong, D., Li, Y., Wang, Z., & Sarkar, F. H. (2011). Cancer stem cells and epithelial-to-mesenchymal transition (EMT)-phenotypic cells: are they cousins or twins?. *Cancers*, *3*(1), 716-729.

Krcmery, J., Camarata, T., Kulisz, A., & Simon, H. G. (2010). Nucleocytoplasmic functions of the PDZ-LIM protein family: new insights into organ development. *Bioessays*, *32*(2), 100-108.

Kumar, R. R., Agarwal, N., Shree, A., Gorain, J. K., Rahul, E., Ganguly, S., ... & Sharma, U. (2025). Decoding the immune landscape in Ewing sarcoma pathogenesis: The role of tumor infiltrating immune cells and immune milieu. *Journal of Bone Oncology*, 100678.

Lambert, A. W., Pattabiraman, D. R., & Weinberg, R. A. (2017). Emerging biological principles of metastasis. *Cell*, *168*(4), 670-691.

Lebrun, J. J. (2012). The dual role of TGFβ in human cancer: from tumor suppression to cancer metastasis. *International Scholarly Research Notices*, *2012*(1), 381428.

Lee, A. V., Nestler, K. A., & Chiappinelli, K. B. (2024). Therapeutic targeting of DNA methylation alterations in cancer. *Pharmacology & therapeutics*, *258*, 108640.

Lessnick, S. L., & Ladanyi, M. (2012). Molecular pathogenesis of Ewing sarcoma: new therapeutic and transcriptional targets. *Annual Review of Pathology: Mechanisms of Disease*, *7*(1), 145-159.

Li, F., Song, Q. Z., Zhang, Y. F., Wang, X. R., Cao, L. M., Li, N., ... & Zhuang, X. F. (2022). Identifying the EMT-related signature to stratify prognosis and evaluate the tumor microenvironment in lung adenocarcinoma. *Frontiers in Genetics*, *13*, 1008416.

Liao, Z. W., Zhao, L., Cai, M. Y., Xi, M., He, L. R., Yu, F., ... & Liu, M. Z. (2017). P300 promotes migration, invasion and epithelial-mesenchymal transition in a nasopharyngeal carcinoma cell line. *Oncology letters*, *13*(2), 763-769.

Lim, H. J., Wang, Y., Buzdin, A., & Li, X. (2025). A practical guide for choosing an optimal spatial transcriptomics technology from seven major commercially available options. *BMC genomics*, *26*(1), 47.

Liu, D., Black, B. L., & Derynck, R. (2001). TGF-β inhibits muscle differentiation through functional repression of myogenic transcription factors by Smad3. *Genes & development*, *15*(22), 2950-2966.

Liu, K., Gao, X., Kang, B., Liu, Y., Wang, D., & Wang, Y. (2022). The role of tumor stem cell exosomes in cancer invasion and metastasis. *Frontiers in Oncology*, *12*, 836548.

Liu, X., Yuan, H., Zhou, J., Wang, Q., Qi, X., Bernal, C., ... & Li, G. (2021). LMO7 as an unrecognized factor promoting pancreatic cancer progression and metastasis. *Frontiers in Cell and Developmental Biology*, *9*, 647387.

Lu, J., Tan, M., & Cai, Q. (2015). The Warburg effect in tumor progression: mitochondrial oxidative metabolism as an anti-metastasis mechanism. *Cancer letters*, *356*(2), 156-164.

Luo, A., Liu, H., Huang, C., & Wei, S. (2024). Exosome-transmitted circular RNA circ-LMO7 facilitates the progression of osteosarcoma by regulating miR-21-5p/ARHGAP24 axis. *Cancer Biology & Therapy*, *25*(1), 2343450.

Luo, H. Y., Lu, Y. X., Shitara, K., Lenz, H. J., & Xu, R. H. (2025). Global alliances in translational cancer research. *Cancer Cell*, *43*(4), 581-586.

Luo, W., & Wang, Y. (2018). Epigenetic regulators: multifunctional proteins modulating hypoxia-inducible factor-α protein stability and activity. *Cellular and Molecular Life Sciences*, *75*(6), 1043-1056.

Luo, X., Li, Y., Hua, Z., Xue, X., Wang, X., Pang, M., ... & Liu, Y. (2023). Exosomes-mediated tumor metastasis through reshaping tumor microenvironment and distant niche. *Journal of Controlled Release*, *353*, 327-336.

Machiela, M. J., Grünewald, T. G., Surdez, D., Reynaud, S., Mirabeau, O., Karlins, E., ... & Delattre, O. (2018). Genome-wide association study identifies multiple new loci associated with Ewing sarcoma susceptibility. *Nature communications*, *9*(1), 3184.

Margadant, C., & Sonnenberg, A. (2010). Integrin–TGF-β crosstalk in fibrosis, cancer and wound healing. *EMBO reports*, *11*(2), 97-105.

Matsuda, M., Chu, C. W., & Sokol, S. Y. (2022). Lmo7 recruits myosin II heavy chain to regulate actomyosin contractility and apical domain size in Xenopus ectoderm. *Development*, *149*(10), dev200236.

Matthews, J. M., Lester, K., Joseph, S., & Curtis, D. J. (2013). LIM-domain-only proteins in cancer. *Nature Reviews Cancer*, *13*(2), 111-122.

Maunakea, A. K., Nagarajan, R. P., Bilenky, M., Ballinger, T. J., D'Souza, C., Fouse, S. D., ... & Costello, J. F. (2010). Conserved role of intragenic DNA methylation in regulating alternative promoters. *Nature*, *466*(7303), 253-257.

Miallot, R., Galland, F., Millet, V., Blay, J. Y., & Naquet, P. (2021). Metabolic landscapes in sarcomas. *Journal of hematology & oncology*, *14*(1), 114.

Miller, B. F., Huang, F., Atta, L., Sahoo, A., & Fan, J. (2022). Reference-free cell type deconvolution of multi-cellular pixel-resolution spatially resolved transcriptomics data. *Nature communications*, *13*(1), 2339.

Misra, A., Pandey, C., Sze, S. K., & Thanabalu, T. (2012). Hypoxia activated EGFR signaling induces epithelial to mesenchymal transition (EMT). *PloS one*, *7*(11), e49766.

Mo, C. K., Liu, J., Chen, S., Storrs, E., Targino da Costa, A. L. N., Houston, A., ... & Ding, L. (2024). Tumour evolution and microenvironment interactions in 2D and 3D space. *Nature*, *634*(8036), 1178-1186.

Moriyama, K., Yonezawa, N., Sakai, H., Yahara, I., & Nishida, E. (1992). Mutational analysis of an actin-binding site of cofilin and characterization of chimeric proteins between cofilin and destrin. *Journal of Biological Chemistry*, *267*(11), 7240-7244.

Muthahari, Y. A., Magnus, L., & Laurino, P. (2025). From duplication to fusion: Expanding Dayhoff's model of protein evolution. *Protein Science*, *34*(3), e70054.

Nagano, A., Ohno, T., Shimizu, K., Hara, A., Yamamoto, T., Kawai, G., ... & Takei, Y. (2010). EWS/Fli-1 chimeric fusion gene upregulates vascular endothelial growth factor-A. *International journal of cancer*, *126*(12), 2790-2798.

Nandra, R., Hwang, N., Matharu, G. S., Reddy, K., & Grimer, R. (2015). One-year mortality in patients with bone and soft tissue sarcomas as an indicator of delay in presentation. *The Annals of The Royal College of Surgeons of England*, *97*(6), 425-433.

Neri, F., Rapelli, S., Krepelova, A., Incarnato, D., Parlato, C., Basile, G., ... & Oliviero, S. (2017). Intragenic DNA methylation prevents spurious transcription initiation. *Nature*, *543*(7643), 72-77.

Niedan, S., Kauer, M., Aryee, D. N. T., Kofler, R., Schwentner, R., Meier, A., ... & Kovar, H. (2014). Suppression of FOXO1 is responsible for a growth regulatory repressive transcriptional sub-signature of EWS-FLI1 in Ewing sarcoma. *Oncogene*, *33*(30), 3927-3938.

Nieto, M. A., Huang, R. Y. J., Jackson, R. A., & Thiery, J. P. (2016). EMT: 2016. *cell*, *166*(1), 21-45.

Notaro, A., Messina, A., & La Bella, V. (2021). A deletion of the nuclear localization signal domain in the FUS protein induces stable post-stress cytoplasmic inclusions in SH-SY5Y cells. *Frontiers in neuroscience*, *15*, 759659.

Nurmagambetova, A., Mustyatsa, V., Saidova, A., & Vorobjev, I. *Morphological and cytoskeleton changes in cells after EMT. Sci Rep. 2023; 13: 22164*.

Orth, M. F., Surdez, D., Faehling, T., Ehlers, A. C., Marchetto, A., Grossetête, S., ... & Grünewald, T. G. (2022). Systematic multi-omics cell line profiling uncovers principles of Ewing sarcoma fusion oncogene-mediated gene regulation. *Cell reports*, *41*(10).

Owen, L. A., Kowalewski, A. A., & Lessnick, S. L. (2008). EWS/FLI mediates transcriptional repression via NKX2. 2 during oncogenic transformation in Ewing's sarcoma. *PloS one*, *3*(4), e1965.

Oyinlade, O., Wei, S., Kammers, K., Liu, S., Wang, S., Ma, D., ... & Xia, S. (2018). Analysis of KLF4 regulated genes in cancer cells reveals a role of DNA methylation in promoter-enhancer interactions. *Epigenetics*, *13*(7), 751-768.

Pardali, E., Van Der Schaft, D. W. J., Wiercinska, E., Gorter, A., Hogendoorn, P. C. W., Griffioen, A. W., & Ten Dijke, P. (2011). Critical role of endoglin in tumor cell plasticity of Ewing sarcoma and melanoma. *Oncogene*, *30*(3), 334-345.

Pastushenko, I., & Blanpain, C. (2019). EMT transition states during tumor progression and metastasis. *Trends in cell biology*, *29*(3), 212-226.

Pastushenko, I., Brisebarre, A., Sifrim, A., Fioramonti, M., Revenco, T., Boumahdi, S., ... & Blanpain, C. (2018). Identification of the tumour transition states occurring during EMT. *Nature*, *556*(7702), 463-468.

Patel, A. A., Gupta, D., Seligson, D., Hattab, E. M., Balis, U. J., Ulbright, T. M., ... & Shared Pathology Informatics Network spin@ pop. nci. nih. gov. (2007). Availability and quality of paraffin blocks identified in pathology archives: a multi-institutional study by the Shared Pathology Informatics Network (SPIN). *BMC cancer*, *7*(1), 37.

Patel, M., Simon, J.M., Iglesia, M.D., Wu, S.B., McFadden, A.W., Lieb, J.D. and Davis, I.J., 2012. Tumor-specific retargeting of an oncogenic transcription factor chimera results in dysregulation of chromatin and transcription. *Genome research*, *22*(2), pp.259-270.

Paulussen, M., Fröhlich, B., & Jürgens, H. (2001). Ewing tumour: incidence, prognosis and treatment options. *Paediatric drugs*, *3*, 899-913.

Pedersen, E. A., Menon, R., Bailey, K. M., Thomas, D. G., Van Noord, R. A., Tran, J., ... & Lawlor, E. R. (2016). Activation of Wnt/β-catenin in Ewing sarcoma cells antagonizes EWS/ETS function and promotes phenotypic transition to more metastatic cell states. *Cancer research*, *76*(17), 5040-5053.

Peter, M., Couturier, J., Pacquement, H., Michon, J., Thomas, G., Magdelenat, H., & Delattre, O. (1997). A new member of the ETS family fused to EWS in Ewing tumors. *Oncogene*, *14*(10), 1159-1164.

Peters, H. L., Yan, Y., Nordgren, T. M., Cutucache, C. E., Joshi, S. S., & Solheim, J. C. (2013). Amyloid precursor-like protein 2 suppresses irradiation-induced apoptosis in Ewing sarcoma cells and is elevated in immune-evasive Ewing sarcoma cells. *Cancer biology & therapy*, *14*(8), 752-760.

Picard, C., Macagno, N., Corradini, N., Marec-Bérard, P., Cabet, S., Guibaud, L., ... & Dijoud, F. (2022). Identification of a novel translocation producing an in-frame fusion of TAF15 and ETV4 in a case of extraosseous Ewing sarcoma revealed in the prenatal period. *Virchows Archiv*, *481*(4), 665-669.

Possidonio, A. C., Soares, C. P., Fontenele, M., Morris, E. R., Mouly, V., Costa, M. L., & Mermelstein, C. (2016). Knockdown of Lmo7 inhibits chick myogenesis. *FEBS letters*, *590*(3), 317-329.

Postel-Vinay, S., Véron, A. S., Tirode, F., Pierron, G., Reynaud, S., Kovar, H., ... & Delattre, O. (2012). Common variants near TARDBP and EGR2 are associated with susceptibility to Ewing sarcoma. *Nature genetics*, *44*(3), 323-327.

Puram, S. V., Tirosh, I., Parikh, A. S., Patel, A. P., Yizhak, K., Gillespie, S., ... & Bernstein, B. E. (2017). Single-cell transcriptomic analysis of primary and metastatic tumor ecosystems in head and neck cancer. *Cell*, *171*(7), 1611-1624.

Quail, D. F., & Joyce, J. A. (2013). Microenvironmental regulation of tumor progression and metastasis. *Nature medicine*, *19*(11), 1423-1437.

Rao, S. S., Huntley, M. H., Durand, N. C., Stamenova, E. K., Bochkov, I. D., Robinson, J. T., ... & Aiden, E. L. (2014). A 3D map of the human genome at kilobase resolution reveals principles of chromatin looping. *Cell*, *159*(7), 1665-1680.

Rauch, T. A., Wu, X., Zhong, X., Riggs, A. D., & Pfeifer, G. P. (2009). A human B cell methylome at 100− base pair resolution. *Proceedings of the National Academy of Sciences*, *106*(3), 671-678.

Riggi, N., Knoechel, B., Gillespie, S. M., Rheinbay, E., Boulay, G., Suvà, M. L., ... & Rivera, M. N. (2014). EWS-FLI1 utilizes divergent chromatin remodeling mechanisms to directly activate or repress enhancer elements in Ewing sarcoma. *Cancer cell*, *26*(5), 668-681.

Riggi, N., Suvà, M. L., Suvà, D., Cironi, L., Provero, P., Tercier, S., ... & Stamenkovic, I. (2008). EWS-FLI-1 expression triggers a Ewing's sarcoma initiation program in primary human mesenchymal stem cells. *Cancer research*, *68*(7), 2176-2185.

Ryland, K. E., Hawkins, A. G., Weisenberger, D. J., Punj, V., Borinstein, S. C., Laird, P. W., ... & Lawlor, E. R. (2016). Promoter methylation analysis reveals that KCNA5 ion channel silencing supports Ewing sarcoma cell proliferation. *Molecular Cancer Research*, *14*(1), 26-34.

Saggese, G., Baroncelli, G. I., & Bertelloni, S. (2002). Puberty and bone development. *Best practice & research Clinical endocrinology & metabolism*, *16*(1), 53-64.

Sala, S., & Ampe, C. (2018). An emerging link between LIM domain proteins and nuclear receptors. *Cellular and Molecular Life Sciences*, *75*(11), 1959-1971.

Sala, S., & Oakes, P. W. (2023). LIM domain proteins. *Current Biology*, *33*(9), R339-R341.

Sankar, S., Bell, R., Stephens, B., Zhuo, R., Sharma, S., Bearss, D. J., & Lessnick, S. L. (2013). Mechanism and relevance of EWS/FLI-mediated transcriptional repression in Ewing sarcoma. *Oncogene*, *32*(42), 5089-5100.

Sannino, G., Marchetto, A., Kirchner, T., & Grünewald, T. G. (2017). Epithelial-to-mesenchymal and mesenchymal-to-epithelial transition in mesenchymal tumors: a paradox in sarcomas?. *Cancer research*, *77*(17), 4556-4561.

Sannino, G., Marchetto, A., Ranft, A., Jabar, S., Zacherl, C., Alba-Rubio, R., ... & Grünewald, T. G. (2019). Gene expression and immunohistochemical analyses identify SOX2 as major risk factor for overall survival and relapse in Ewing sarcoma patients. *EBioMedicine*, *47*, 156-162.

Saratov, V., Ngo, Q. A., Pedot, G., Sidorov, S., Wachtel, M., Niggli, F. K., & Schäfer, B. W. (2022). CRISPR activation screen identifies TGFβ-associated PEG10 as a crucial tumor suppressor in Ewing sarcoma. *Scientific Reports*, *12*(1), 10671.

Savola, S., Klami, A., Myllykangas, S., Manara, C., Scotlandi, K., Picci, P., ... & Vakkila, J. (2011). High Expression of Complement Component 5 (C5) at Tumor Site Associates with Superior Survival in Ewing′ s Sarcoma Family of Tumour Patients. *International Scholarly Research Notices*, *2011*(1), 168712.

Schindelin, J., Arganda-Carreras, I., Frise, E., Kaynig, V., Longair, M., Pietzsch, T., ... & Cardona, A. (2012). Fiji: an open-source platform for biological-image analysis. *Nature methods*, *9*(7), 676-682.

Schubert, M., Klinger, B., Klünemann, M., Sieber, A., Uhlitz, F., Sauer, S., ... & Saez-Rodriguez, J. (2018). Perturbation-response genes reveal signaling footprints in cancer gene expression. *Nature communications*, *9*(1), 20.

Scotlandi, K., Remondini, D., Castellani, G., Manara, M. C., Nardi, F., Cantiani, L., ... & Picci, P. (2009). Overcoming resistance to conventional drugs in Ewing sarcoma and identification of molecular predictors of outcome. *Journal of clinical oncology*, *27*(13), 2209-2216.

Selvanathan, S. P., Graham, G. T., Erkizan, H. V., Dirksen, U., Natarajan, T. G., Dakic, A., ... & Toretsky, J. A. (2015). Oncogenic fusion protein EWS-FLI1 is a network hub that regulates alternative splicing. *Proceedings of the National Academy of Sciences*, *112*(11), E1307-E1316.

Serebryannyy, L., & de Lanerolle, P. (2020). Nuclear actin: The new normal. *Mutation Research/Fundamental and Molecular Mechanisms of Mutagenesis*, *821*, 111714.

Shankar, J., & Nabi, I. R. (2015). Actin cytoskeleton regulation of epithelial mesenchymal transition in metastatic cancer cells. *PloS one*, *10*(3), e0119954.

Shao, I. H., Peng, P. H., Wu, H. H., Chen, J. L., Lai, J. C. Y., Chang, J. S., ... & Hsu, K. W. (2023). RP11-367G18. 1 V2 enhances clear cell renal cell carcinoma progression via induction of epithelial–mesenchymal transition. *Cancer Medicine*, *12*(8), 9788-9801.

Sheffield, N. C., Pierron, G., Klughammer, J., Datlinger, P., Schönegger, A., Schuster, M., ... & Tomazou, E. M. (2017). DNA methylation heterogeneity defines a disease spectrum in Ewing sarcoma. *Nature medicine*, *23*(3), 386-395.

Sheikh, K. A., Amjad, M., Irfan, M. T., Anjum, S., Majeed, T., Riaz, M. U., ... & Ibrahim, W. N. (2025). Exploring TGF-β signaling in cancer progression: prospects and therapeutic strategies. *OncoTargets and Therapy*, 233-262.

Shirakawa, T., Rojasawasthien, T., Inoue, A., Matsubara, T., Kawamoto, T., & Kokabu, S. (2021). Tumor necrosis factor alpha regulates myogenesis to inhibit differentiation and promote proliferation in satellite cells. *Biochemical and Biophysical Research Communications*, *580*, 35-40.

Shishido-Hara, Y. (2010). Progressive multifocal leukoencephalopathy and promyelocytic leukemia nuclear bodies: a review of clinical, neuropathological, and virological aspects of JC virus-induced demyelinating disease. *Acta neuropathologica*, *120*(3), 403-417.

Siegel, R. L., Kratzer, T. B., Giaquinto, A. N., Sung, H., & Jemal, A. (2025). Cancer statistics, 2025. *Ca*, *75*(1), 10.

Silveira, D. A., Gupta, S., da Cunha Jaeger, M., Brunetto de Farias, C., Mombach, J. C. M., & Sinigaglia, M. (2023). A logical model of Ewing sarcoma cell epithelial-to-mesenchymal transition supports the existence of hybrid cellular phenotypes. *FEBS letters*, *597*(19), 2446-2460.

Singer, O., & Verma, I. M. (2008). Applications of lentiviral vectors for shRNA delivery and transgenesis. *Current gene therapy*, *8*(6), 483-488.

Sitcheran, R., Cogswell, P. C., & Baldwin, A. S. (2003). NF-κB mediates inhibition of mesenchymal cell differentiation through a posttranscriptional gene silencing mechanism. *Genes & development*, *17*(19), 2368-2373.

Smith, R., Owen, L. A., Trem, D. J., Wong, J. S., Whangbo, J. S., Golub, T. R., & Lessnick, S. L. (2006). Expression profiling of EWS/FLI identifies NKX2. 2 as a critical target gene in Ewing's sarcoma. *Cancer cell*, *9*(5), 405-416.

Sorensen, P. H., Lessnick, S. L., Lopez-Terrada, D., Liu, X. F., Triche, T. J., & Denny, C. T. (1994). A second Ewing's sarcoma translocation, t (21; 22), fuses the EWS gene to another ETS–family transcription factor, ERG. *Nature genetics*, *6*(2), 146-151.

Spector, L. G., Hubbard, A. K., Diessner, B. J., Machiela, M. J., Webber, B. R., & Schiffman, J. D. (2021). Comparative international incidence of Ewing sarcoma 1988 to 2012. *International journal of cancer*, *149*(5), 1054-1066.

Stein, C. K., Qu, P., Epstein, J., Buros, A., Rosenthal, A., Crowley, J., ... & Barlogie, B. (2015). Removing batch effects from purified plasma cell gene expression microarrays with modified ComBat. *BMC bioinformatics*, *16*(1), 63.

Sun, L., Ma, K., Wang, H., Xiao, F., Gao, Y., Zhang, W., ... & Wu, Z. (2007). JAK1–STAT1–STAT3, a key pathway promoting proliferation and preventing premature differentiation of myoblasts. *Journal of cell biology*, *179*(1), 129-138.

Sun, Y., Kolligs, F. T., Hottiger, M. O., Mosavin, R., Fearon, E. R., & Nabel, G. J. (2000). Regulation of β-catenin transformation by the p300 transcriptional coactivator. *Proceedings of the National Academy of Sciences*, *97*(23), 12613-12618.

Surdez, D., Zaidi, S., Grossetête, S., Laud-Duval, K., Ferre, A. S., Mous, L., ... & Delattre, O. (2021). STAG2 mutations alter CTCF-anchored loop extrusion, reduce cis-regulatory interactions and EWSR1-FLI1 activity in Ewing sarcoma. *Cancer cell*, *39*(6), 810-826.

Tak, Y. E., Boulay, G., Lee, L., Iyer, S., Perry, N. T., Schultz, H. T., ... & Rivera, M. N. (2022). Genome-wide functional perturbation of human microsatellite repeats using engineered zinc finger transcription factors. *Cell genomics*, *2*(4).

Tang, H., Peng, Q., Oyang, L., Tan, S., Jiang, X., Ren, Z., ... & Zhou, Y. (2025). Fusion genes in cancers: Biogenesis, functions, and therapeutic implications. *Genes & Diseases*, 101536.

Tirode, F., Laud-Duval, K., Prieur, A., Delorme, B., Charbord, P., & Delattre, O. (2007). Mesenchymal stem cell features of Ewing tumors. *Cancer cell*, *11*(5), 421-429.

Tirode, F., Surdez, D., Ma, X., Parker, M., Le Deley, M. C., Bahrami, A., ... & Delattre, O. (2014). Genomic landscape of Ewing sarcoma defines an aggressive subtype with co-association of STAG2 and TP53 mutations. *Cancer discovery*, *4*(11), 1342-1353.

Tołoczko-Iwaniuk, N., Dziemiańczyk-Pakieła, D., Nowaszewska, B. K., Celińska-Janowicz, K., & Miltyk, W. (2019). Celecoxib in cancer therapy and prevention–review. *Current drug targets*, *20*(3), 302-315.

Tomazou, E. M., Sheffield, N. C., Schmidl, C., Schuster, M., Schönegger, A., Datlinger, P., ... & Kovar, H. (2015). Epigenome mapping reveals distinct modes of gene regulation and widespread enhancer reprogramming by the oncogenic fusion protein EWS-FLI1. *Cell reports*, *10*(7), 1082-1095.

Tseng, P. C., Chen, C. L., Lee, K. Y., Feng, P. H., Wang, Y. C., Satria, R. D., & Lin, C. F. (2022). Epithelial-to-mesenchymal transition hinders interferon-γ-dependent immunosurveillance in lung cancer cells. *Cancer Letters*, *539*, 215712.

Tu, J., Huo, Z., Gingold, J., Zhao, R., Shen, J., & Lee, D. F. (2017). The histogenesis of Ewing sarcoma. *Cancer reports and reviews*, *1*(2), 10-15761.

Tzeng, Y. W., Li, D. Y., Chen, Y., Yang, C. H., Chang, C. Y., & Juang, Y. L. (2018). LMO7 exerts an effect on mitosis progression and the spindle assembly checkpoint. *The International Journal of Biochemistry & Cell Biology*, *94*, 22-30.

Ueno-Yokohata, H., Okita, H., Nakasato, K., Kiyotani, C., Kato, M., Matsumoto, K., ... & Yoshioka, T. (2021). Establishment of multiplex RT-PCR to detect fusion genes for the diagnosis of Ewing sarcoma. *Diagnostic Pathology*, *16*, 1-10.

Urano, F., Umezawa, A., Yabe, H., Hong, W., Yoshida, K., Fujinaga, K., & Hata, J. I. (1998). Molecular analysis of Ewing's sarcoma: another fusion gene, EWS-E1AF, available for diagnosis. *Japanese journal of cancer research*, *89*(7), 703-711.

Van Tilburg, C. M., Pfaff, E., Pajtler, K. W., Langenberg, K. P., Fiesel, P., Jones, B. C., ... & Witt, O. (2021). The pediatric precision oncology INFORM registry: clinical outcome and benefit for patients with very high-evidence targets. *Cancer discovery*, *11*(11), 2764-2779.

Vasileva, E., Arata, C., Luo, Y., Burgos, R., Crump, J. G., & Amatruda, J. F. (2024). Origin of Ewing sarcoma by embryonic reprogramming of neural crest to mesoderm. *bioRxiv*.

Visser, L. L., Bleijs, M., Margaritis, T., van de Wetering, M., Holstege, F. C., & Clevers, H. (2023). Ewing sarcoma single-cell transcriptome analysis reveals functionally impaired antigen-presenting cells. *Cancer research communications*, *3*(10), 2158-2169.

Vojta, A., Dobrinić, P., Tadić, V., Bočkor, L., Korać, P., Julg, B., ... & Zoldoš, V. (2016). Repurposing the CRISPR-Cas9 system for targeted DNA methylation. *Nucleic acids research*, *44*(12), 5615-5628.

Volchenboum, S. L., Andrade, J., Huang, L., Barkauskas, D. A., Krailo, M., Womer, R. B., ... & Lawlor, E. R. (2015). Gene expression profiling of E wing sarcoma tumours reveals the prognostic importance of tumour–stromal interactions: a report from the C hildren's O ncology G roup. *The Journal of Pathology: Clinical Research*, *1*(2), 83-94.

von Levetzow, C., Jiang, X., Gwye, Y., von Levetzow, G., Hung, L., Cooper, A., ... & Lawlor, E. R. (2011). Modeling initiation of Ewing sarcoma in human neural crest cells. *PloS one*, *6*(4), e19305.

Voss, P. G., & Wang, J. L. (2023). Liquid-liquid phase separation: Galectin-3 in nuclear speckles and ribonucleoprotein complexes. *Experimental cell research*, *427*(1), 113571.

Wang, L., Wu, L., Qi, G., Liu, C., Wang, W., Zhang, X. H. F., & Liu, Z. (2025). ReSort enhances reference-based cell type deconvolution for spatial transcriptomics through regional information integration. *Bioinformatics Advances*, *5*(1), vbaf091.

Wang, Q., Xiong, F., Wu, G., Liu, W., Chen, J., Wang, B., & Chen, Y. (2022). Gene body methylation in cancer: molecular mechanisms and clinical applications. *Clinical Epigenetics*, *14*(1), 154.

Wei, E., Mitanoska, A., O'Brien, Q., Porter, K., Molina, M., Ahsan, H., ... & Bosnakovski, D. (2024). Pharmacological targeting of P300/CBP reveals EWS:: FLI1-mediated senescence evasion in Ewing sarcoma. *Molecular Cancer*, *23*(1), 222.

Wei, X., Li, H., Yang, J., Hao, D., Dong, D., Huang, Y., ... & Chen, H. (2017). Circular RNA profiling reveals an abundant circLMO7 that regulates myoblasts differentiation and survival by sponging miR-378a-3p. *Cell death & disease*, *8*(10), e3153-e3153.

Wiles, E. T., Bell, R., Thomas, D., Beckerle, M., & Lessnick, S. L. (2013). ZEB2 represses the epithelial phenotype and facilitates metastasis in Ewing sarcoma. *Genes & cancer*, *4*(11-12), 486-500.

Wolf, F. A., Angerer, P., & Theis, F. J. (2018). SCANPY: large-scale single-cell gene expression data analysis. *Genome biology*, *19*, 1-5.

Wrenn, E. D., Apfelbaum, A. A., Rudzinski, E. R., Deng, X., Jiang, W., Sud, S., ... & Lawlor, E. R. (2023). Cancer-associated fibroblast-like tumor cells remodel the Ewing sarcoma tumor microenvironment. *Clinical Cancer Research*, *29*(24), 5140-5154.

Wu, H. T., & Govender, D. (2012). Ewing sarcoma family of tumours: unusual histological variants and immunophenotypic characteristics. *Diagnostic Histopathology*, *18*(8), 348-355.

Wu, J. S., Jiang, J., Chen, B. J., Wang, K., Tang, Y. L., & Liang, X. H. (2021). Plasticity of cancer cell invasion: Patterns and mechanisms. *Translational oncology*, *14*(1), 100899.

Wu, Y. D., & Zhou, B. P. (2010). TNF-α/NF-κB/Snail pathway in cancer cell migration and invasion. *British journal of cancer*, *102*(4), 639-644.

Xiao, Z., Cai, Z., Deng, D., Tong, S., & Zu, X. (2022). An EMT-based risk score thoroughly predicts the clinical prognosis, tumor immune microenvironment and molecular subtypes of bladder cancer. *Frontiers in Immunology*, *13*, 1000321.

Xie, Y., Ostriker, A. C., Jin, Y., Hu, H., Sizer, A. J., Peng, G., ... & Martin, K. A. (2019). LMO7 is a negative feedback regulator of transforming growth factor β signaling and fibrosis. *Circulation*, *139*(5), 679-693.

Xu, F., Zhang, J., Hu, G., Liu, L., & Liang, W. (2017). Hypoxia and TGF-β1 induced PLOD2 expression improve the migration and invasion of cervical cancer cells by promoting epithelial-to-mesenchymal transition (EMT) and focal adhesion formation. *Cancer cell international*, *17*(1), 54.

Xu, J., Lamouille, S., & Derynck, R. (2009). TGF-β-induced epithelial to mesenchymal transition. *Cell research*, *19*(2), 156-172.

Xu, M., Zhang, T., Xia, R., Wei, Y., & Wei, X. (2022). Targeting the tumor stroma for cancer therapy. *Molecular Cancer*, *21*(1), 208.

Xue, C., Yao, Q., Gu, X., Shi, Q., Yuan, X., Chu, Q., ... & Li, L. (2023). Evolving cognition of the JAK-STAT signaling pathway: autoimmune disorders and cancer. *Signal transduction and targeted therapy*, *8*(1), 204.

Yamashita, N., Tokunaga, E., Iimori, M., Inoue, Y., Tanaka, K., Kitao, H., ... & Maehara, Y. (2018). Epithelial paradox: clinical significance of coexpression of E-cadherin and vimentin with regard to invasion and metastasis of breast cancer. *Clinical breast cancer*, *18*(5), e1003-e1009.

Yan, F., Zhang, X., Tan, R., Li, M., Xiao, Z., Wang, H., ... & Liu, Z. (2021). Autophagic flux in cancer cells at the invasive front in the tumor-stroma border. *Aging (Albany NY)*, *13*(16), 20229.

Yang, X., Han, H., De Carvalho, D. D., Lay, F. D., Jones, P. A., & Liang, G. (2014). Gene body methylation can alter gene expression and is a therapeutic target in cancer. *Cancer cell*, *26*(4), 577-590.

Yasir, M., Park, J., & Chun, W. (2023). EWS/FLI1 characterization, activation, repression, target genes and therapeutic opportunities in Ewing sarcoma. *International Journal of Molecular Sciences*, *24*(20), 15173.

Yates, J., & Van Allen, E. M. (2025). New horizons at the interface of artificial intelligence and translational cancer research. *Cancer Cell*, *43*(4), 708-727.

Yu, L., Davis, I. J., & Liu, P. (2023). Regulation of EWSR1-FLI1 function by post-transcriptional and post-translational modifications. *Cancers*, *15*(2), 382.

Zaidi, S. K., Young, D. W., Choi, J. Y., Pratap, J., Javed, A., Montecino, M., ... & Stein, G. S. (2005). The dynamic organization of gene-regulatory machinery in nuclear microenvironments. *EMBO reports*, *6*(2), 128-133.

Zarghooni, K., Bratke, G., Landgraf, P., Simon, T., Maintz, D., & Eysel, P. (2023). The diagnosis and treatment of osteosarcoma and Ewing's sarcoma in children and adolescents. *Deutsches Ärzteblatt International*, *120*(24), 405.

Zatzman, M., Fuligni, F., Ripsman, R., Suwal, T., Comitani, F., Edward, L. M., ... & Shlien, A. (2022). Widespread hypertranscription in aggressive human cancers. *Science advances*, *8*(47), eabn0238.

Zeng, Q., Jiang, T., & Wang, J. (2024). Role of LMO7 in cancer. *Oncology reports*, *52*(3), 1-12.

Zetouni, N. C., & Sergi, C. M. (2022). Features of metastatic Ewing sarcoma.

Zhan, Q., Liu, B., Situ, X., Luo, Y., Fu, T., Wang, Y., ... & Ke, Z. (2023). New insights into the correlations between circulating tumor cells and target organ metastasis. *Signal transduction and targeted therapy*, *8*(1), 465.

Zhang, H. F., Hughes, C. S., Li, W., He, J. Z., Surdez, D., El-Naggar, A. M., ... & Sorensen, P. H. (2021a). Proteomic screens for suppressors of anoikis identify IL1RAP as a promising surface target in Ewing sarcoma. *Cancer discovery*, *11*(11), 2884-2903.

Zhang, Q., Han, Z., Zhu, Y., Chen, J., & Li, W. (2021b). Role of hypoxia inducible factor-1 in cancer stem cells. *Molecular Medicine Reports*, *23*(1), 17.

Zhang, X., Smits, A. H., Van Tilburg, G. B., Ovaa, H., Huber, W., & Vermeulen, M. (2018). Proteome-wide identification of ubiquitin interactions using UbIA-MS. *Nature protocols*, *13*(3), 530-550.

Zhang, Y., Ma, W., Huang, Z., Liu, K., Feng, Z., Zhang, L., ... & Liu, Q. (2024). Research and application of omics and artificial intelligence in cancer. *Physics in Medicine & Biology*, *69*(21), 21TR01.

Zhao, J., Jin, D., Huang, M., Ji, J., Xu, X., Wang, F., ... & Xiao, M. (2024). Glycolysis in the tumor microenvironment: a driver of cancer progression and a promising therapeutic target. *Frontiers in Cell and Developmental Biology*, *12*, 1416472.

Zhen, Y. Y., Wu, C. H., Chen, H. C., Chang, E. E., Lee, J. J., Chen, W. Y., ... & Hung, C. C. (2022). Coordination of LMO7 with FAK Signaling Sustains Epithelial Integrity in Renal Epithelia Exposed to Osmotic Pressure. *Cells*, *11*(23), 3805.

Zhou, D., Duan, Z., Li, Z., Ge, F., Wei, R., & Kong, L. (2022). The significance of glycolysis in tumor progression and its relationship with the tumor microenvironment. *Frontiers in Pharmacology*, *13*, 1091779.

Zhu, C., Preissl, S., & Ren, B. (2020). Single-cell multimodal omics: the power of many. *Nature methods*, *17*(1), 11-14.

Zhu, S., Kubota, N., Wang, S., Wang, T., Xiao, G., & Hoshida, Y. (2023). Single-cell level deconvolution, convolution, and clustering in spatial transcriptomics by aligning spot level transcriptome to nuclear morphology. *bioRxiv*.

Zöllner, S. K., Amatruda, J. F., Bauer, S., Collaud, S., de Álava, E., DuBois, S. G., ... & Dirksen, U. (2021). Ewing sarcoma—diagnosis, treatment, clinical challenges and future perspectives. *Journal of clinical medicine*, *10*(8), 1685.

9. ACKNOWLEDGEMENTS

I would like to express my great gratitude to my mentors Professor Grünewald and Doctor Cidre-Aranaz for taking me on board as part of their team, for appreciating all my ideas and thoughts and for challenging me in ways that proved to myself how much I am able to achieve. I would like to express immense gratitude to the International DKFZ PhD program that recognized my efforts and granted me a scholarship to be part of this truly inspiring institute. I would like to show gratitude and appreciation to all members, past and present, of the Division of Translational Pediatric Sarcoma Research for their valuable advice and assistance whenever needed. Especially Lovro, Angeline, J-Ann, Angelina, Anna, Nina, Nadine, Mallory, Pablo, Carla, Marleen, Jana, Endrit, Katha, Florian, Steffi, Felina, Sabrina, Zuzanna, Martha, Alina, Malenka, Shunya, and Jing for listening, choosing the right words, empowering and helping me scientifically, emotionally and simply being great friends and colleagues. I am very thankful to Annika for her time and help with German translation of the thesis summary and to Kim for proof-reading my thesis and giving valuable writing advice.

I would like to express my big recognition for the group of Dr. Ashok Kumar Jayavelu and his student Lianghao Mao who generously helped me with proteomic analysis, as well as the lab of Prof. Dr. Moritz Gerstung and his student Heng Luo who were extremely supportive, friendly, and allowed to me learn a lot from them on bioinformatics analysis and spatial transcriptomics. Furthermore, I would like to thank members of Light Microscopy Core Facility, Claudia and Damir, who supported me through various IHC analyses and IF confocal imaging. I would like to express gratitude to my TAC members Prof. Dr. Ursula Klingmüller and Prof. Dr. Didier Surdez for their valuable advice and support through the years. Also, I would like to thank all members from the PhD office, Lindsay, Mariana, and Marion, for their immense support and patience for all of my questions. Furthermore, I would like to express my gratitude for my friendship with Yara, a truly great scientist equally as great a friend, who always whole-heartedly supported me through my journey. Additionally, I would also like to take this opportunity to say how deeply grateful I am to all the patients who generously donated their tumor material for research, as well as to their families and the clinicians involved in their care, whose contributions made this study possible.

Finally, I am very grateful and pleased to have such a beautiful family: Lorena, Neven and Viktoria, who always encouraged, supported and valued me for who I am. I would have never

been able to achieve anything without them trusting so much in me, even when I had doubts myself. I would also like to express my great gratitude to my husband Hrvoje, love of my life, who encouraged me to enroll in this PhD program, was always my pillar, listened and helped me from the beginning of our student days till we are both now finishing our PhDs.